

STUDYING OIL SPILL TRANSPORT BY EXPLORING OIL-MINERAL-
AGGREGATES CHARACTERISTICS AND TIDAL DISPERSION
PROPERTIES

by

Xiaomei Zhong

Submitted in partial fulfilment of the requirements
for the degree of Doctor of Philosophy

at

Dalhousie University
Halifax, Nova Scotia
April 2023

© Copyright by Xiaomei Zhong, 2023

TABLE OF CONTENTS

LIST OF TABLES	v
LIST OF FIGURES	vi
ABSTRACT.....	viii
LIST OF ABBREVIATIONS USED	ix
ACKNOWLEDGEMENTS.....	xv
Chapter 1: Introduction.....	1
1.1 Background.....	1
1.2 Research Objectives.....	8
1.3 Thesis Organization	9
Chapter 2: Literature Review.....	10
2.1 General Information on Oil Spill	10
2.2 Factors Influencing OMA Formation	15
2.3 OMA Settling.....	18
2.4 Modeling OMA Size Distribution	20
2.5 OMA Transport Modelling.....	25
2.6 Finite-Time Lyapunov Exponent (FTLE).....	33
2.7 Machine Learning Algorithms.....	36
2.8 Summary	39
Chapter 3: Materials and Methods.....	41
3.1 OMA Formation Experiments	41
3.2 OMA Settling Velocity Measurement	43
3.3 Traditional Empirical Prediction of OMA Settling Velocity.....	45
3.4 Machine Learning Prediction.....	50

3.5 Particle Tracking Algorithm	52
Chapter 4: OMA Formation.....	54
4.1 Experimental Design and Acquired Data	54
4.2 Statistical Analysis.....	54
4.2.1 Significance of Studied Factors	54
4.2.2 Interaction Effects.....	61
4.3 Machine Learning Prediction.....	64
4.3.1 Algorithm Selection.....	64
4.3.2 Factor Importance Quantification by Machine Learning Algorithm.....	68
4.4 Comparison with Collision-Theory-Based Prediction.....	69
4.5 Machine Learning Based Prediction Tool	72
4.6 Summary	73
4.7 Transition Section	75
Chapter 5: OMA Settling Velocity and Empirical Equations.....	76
5.1 Experimental Design and Data Acquire	76
5.2 Laboratory Tests	76
5.2.1 Data Adequacy and Characteristics	76
5.2.2 Correlation Between Studied Factors and Settling Velocity	77
5.3 Numerical Modelling on OMA Settling Velocity	80
5.3.1 Traditional Empirical Approaches.....	80
5.3.2 Machine Learning Prediction.....	84
5.4 Sensitivity Analysis	87
5.4.1 Hypothetical Case Study in A Square field	87
5.4.2 Hypothetical Case Study in Burrard Inlet.....	92
5.5 Summary.....	95

5.6 Transition Section	97
Chapter 6 Applying Finite-Time Lyapunov Exponent to Study the Tidal Dispersion Properties in Burrard Inlet	98
6.1 Particle Tracking Algorithm	98
6.2 General Descriptions for FTLE	99
6.3 Stochastic Simulation.....	100
6.4 FTLE Analysis Results	103
6.5 Tidal Dispersion Properties.....	112
6.6 The <i>M/V Marathassa</i> Oil Spill.....	117
6.7 Stochastic Oil Spill Modelling.....	120
6.8 Summary	123
Chapter 7: Conclusion.....	125
7.1 Summary and Conclusions	125
7.2 Future Work and Recommendations	130
References.....	132
APPENDIX A.....	157
APPENDIX B.....	161

LIST OF TABLES

Table 2.1 Examples of 3D oil spill models that use a Lagrangian algorithm to simulate oil transport.	13
Table 2.2 Summary of laboratory experiments on the OMA settling velocity.	20
Table 2.3 A summary of equations relevant to the modelling of oil-mineral-aggregates formation.	28
Table 2.4 Equations are used to estimate the settling velocity of oil-mineral-aggregates.	31
Table 3.1 The level of factors of interest for oil-mineral-aggregate formation. ..	43
Table 3.2 Empirical effective density prediction formulas.	47
Table 3.3 Empirical settling velocity prediction equations.	48
Table 4.1 The experiment setting based on Screening Design.	56
Table 4.2 Analysis of variance for oil-mineral aggregate's median diameter (D_{50}).	58
Table 5.1 The coefficient of determination (R^2) from empirical equations for oil-mineral-aggregate's settling velocity prediction.	82
Table 5.2 The root means square error (RMSE) from empirical equations for oil-mineral-aggregate's settling velocity prediction.	83
Table 6.1 The key parameters settings and the release site locations for the stochastic oil spill modelling.	103
Table S6.1 A summary of Figure 6.2 and Figure 6.3.	166

LIST OF FIGURES

Figure 2.1 Formation of OMA in the nearshore environment	15
Figure 2.2 Schematic of OMA formation model	25
Figure 2.3 Flowchart of the model system.....	27
Figure 3.1 The scheme of the settling column experiment system.....	45
Figure 4.1 The influence of significant factors (a) time, (b) temperature, (c) oil/clay ratio and (d) clay type on oil-mineral aggregate’s median diameter.....	61
Figure 4.2 Illustrates how time interacts with (a) the oil/clay ratio and (b) temperature influence on the median diameter of oil-mineral-aggregate.	63
Figure 4.3 The size distribution of the dataset from current and literature data.	66
Figure 4.4 Prediction plots (training and testing) for oil-mineral-aggregate’s median diameter by using machine learning algorithms.....	67
Figure 4.5 The factor importance plot.	69
Figure 4.6 The prediction accuracy of the collision-theory-based numerical model.....	72
Figure 4.7 The screenshot of machine learning based prediction software for oil-mineral-aggregate’s median diameter prediction.	73
Figure 5.1 The characteristics of oil-mineral-aggregate (OMA) based on size bins (a) OMA number distribution, (b) averaged settling velocity.	77
Figure 5.2 The loading plot from principal component analysis of acquired settling velocity data.....	80
Figure 5.3 The plot of oil-mineral-aggregate’s experimental settling velocity vs. theoretically predicted values.	84
Figure 5.4 Prediction plots (training and testing) for oil-mineral-aggregate’s settling velocity by using machine learning algorithms.	86
Figure 5.5 The distribution of oil-mineral-aggregates when it was randomly released in a 2×2 km field by using (a) traditional floc equation and	

(b) machine learning algorithm for settling velocities prediction forcing by a constant current (0.2 m/s) in the northeast direction.....	89
Figure 5.6 The distribution of oil-mineral-aggregates when it was randomly released in a 2×2 km field by using (a) traditional flocculation equation and (b) machine learning algorithm for settling velocities prediction forcing by a constant current (0.2 m/s) that change 30 degrees of direction every 2 hours.	89
Figure 5.7 The trajectories of oil-mineral-aggregates with different sizes	91
Figure 5.8 Burrard Inlet	93
Figure 5.9 The trajectories of oil-mineral-aggregates in a real location.....	95
Figure 6.1 Six oil release sites in Burrard Inlet.....	102
Figure 6.2 The normalized hyperbolic FTLE fields for Burrard inlet during spring tide.	107
Figure 6.3 The normalized hyperbolic FTLE fields for Burrard inlet during neap tide	110
Figure 6.4 Comparison of drifter data with FTLE ridges.	112
Figure 6.5 Residual current vectors for select locations	117
Figure 6.6 Mean tidal excursions.....	117
Figure 6.7 The <i>M/V Marathassa</i> oil spill situation map	118
Figure 6.8 The total probability of oil contamination for an oil spill	122
Figure S3.1 The temperature-controllable shaker.....	163
Figure S3.2 The inverted microscopy.....	163
Figure S3.3 Example image of oil-mineral-aggregates	164
Figure S3.4 The example of OMA settling velocity and size measurements	165
Figure S6.1. Selected locations for comparing the FTLE fields.....	165

ABSTRACT

Oil spill has been widely recognized as a major marine environmental issue, that could cause a profound and long-term impact on the environment, ecology, and socioeconomics. In particular, when the oil spill happens in coastal areas, the spilled oil can interact with the suspended sediments to form oil-mineral-aggregates (OMA), and its settling and trajectory are crucial for oil spill modelling. We started by identifying the most influential variables during OMA formation through a statistical method (Screening Design). Time was the most important factor for OMA median diameter (D_{50}), followed by temperature and oil/clay ratio. The influence of time was highly dependent on the temperature and oil/clay ratio applied. We also assembled a high-speed camera and magnifying lens to measure the settling velocity of OMA precisely and explored how process variables influence the settling velocity. Principal component analysis revealed that increasing clay concentration in the water environment significantly promoted OMA settling velocity. However, the presence of dispersant and water density increment led to settling velocity reduction. The traditional empirical numerical modelling for OMA D_{50} and settling velocity prediction was based on collision-theory and Stokes' law, respectively. The empirical predictions were conducted in this study, and the R^2 of 0.62 and 0.39 were achieved. Machine learning algorithms were, for the first time, employed to predict OMA D_{50} and settling velocity. Adaboost algorithm and Gradient Boost Regression algorithm was identified to be the most satisfying one for predicting D_{50} (R^2 of 0.74) and settling velocity (R^2 of 0.61) respectively, which had correspondingly higher R^2 than traditional empirical numerical modellings. As for the OMA transport, the particle tracking model was applied for simulation. The sensitivity of OMA transport to prediction accuracy was evaluated, and a high sensitivity was observed. In addition to oil spill modelling, the feasibility of using the Finite-Time Lyapunov Exponent (FTLE) to analyze the tidal dispersion properties and oil spill trajectory was assessed. The FTLE results were compared with a real oil spill in Burrard Inlet in 2015. The results indicated that FTLE could reasonably explain the spilled oil's trajectories, suggesting FTLE could be a valuable addition to practical oil spill transport.

LIST OF ABBREVIATIONS USED

2D	Two dimensional
3D	Three dimensional
AdaBoost	Adaptive Boosting
ADIOS	Automated Data Inquiry for Oil Spills
ANOVA	Analysis of Variance
ARCOPOL	The Atlantic Regions' Coastal Pollution Response
ASA	Applied Science Associate
ASCE	American Society of Civil Engineers
COAWST	Coupled Ocean-Atmosphere-Wave-and-Sediment Transport
COSMoS	Coastal Storm Modeling System
COZOIL	coastal zone oil spill
DBWM	Diluted Bitumen Weathering Model
DFO	Fisheries and Oceans Canada
DHI	Danish Hydraulic Institute
ECCC	Environment and Climate Change Canada
ELMs	Eulerian-Lagrangian methods
FTLE	Finite-Time Lyapunov Exponent
FVCOM	Finite-Volume Community Ocean Model
GBR	Gradient Boost Regression
GNOME	General NOAA Operational Modeling Environment
GOMRI	Gulf of Mexico Research Initiative

HCMR	Hellenic Centre for Marine Research
IТОPF	International Tanker Owners Pollution Federation
KFUPM/RI	King Fahd University of Petroleum & Minerals/ Research & Innovation
LCS	Lagrangian Coherent Systems
LP	Lagrangian Parcel
MARETEC	Marine and Environmental Technology Research Center
MOHID	Modelo Hidrodinâmico
MOTHY	Modèle Océanique de Transport d'Hydrocarbures
NASP	National Aerial Surveillance Program
NOAA	National Oceanic and Atmospheric Administration
NRDA	Natural Resource Damage Assessment
OC-UCY	Oceanography Centre of the University of Cyprus
OMA	oil-mineral-aggregation
OSCAR	Oil Spill Response and Contingency Model
OWM	Oil weathering models
PMV	Port of Metro Vancouver
RF	Random Forest
RHSVTTMS-	Revealer High-speed Video Target Tracking Measurement
VL	Software VL
RMSE	Root-Mean-Square-Error
SCAT	Shoreline Cleanup Assessment Technique
SCT	Surface Current Tracker drifters

SINTEF Stiftelsen for Industriell Og Teknisk Forskning

UTC Coordinated Universal Time

SYMBOL	DESCRIPTION	UNIT
A_o	surface area of an oil droplet	μm^2
A_{p-proj}	projection area of particles on the droplet surface when an OMA is formed	μm^2
β	collision frequency	-
β_{Br}	collision efficiency due to Brownian motion	-
β_{sh}	collision efficiency due to fluid shear	-
β_{ds}	collision efficiency due to differential sedimentation	-
C_D	drag coefficient	-
D	Diameter	μm
D_{50}	Median diameter	μm
Δ	the Cauchy-Green deformation tensor	-
D_z	vertical dispersion coefficient	-
E	diffusion coefficient	-
E_{max}	maximum possible trapping efficiency	-
ε	dissipation rate	W/kg

F_{SP}	a factor to account for particle shape and packing effects on the coagulation process	-
g	gravity	m^2/s
k	Boltzman's constant	J/K
K_d	distribution coefficient	-
$\lambda_{max}(\Delta)$	the maximum eigenvalue of the symmetric matrix Δ	-
n_i, n_j	the particle concentrations for the particle of size i and j respectively	number/L
ρ	Density	kg/m^3
r	radii of the oil droplets	m
R^2	coefficient of determination	-
Re	Reynold number	-
sf	surface fractions	-
SR	oil sinking ratio	-
T	absolute temperature	K
$\theta_{k,q}$	the interaction term due to coagulation	-

$\phi_i^T(x)$	FTLE value	-
y_n	Actual value	m/s
\bar{y}	average of actual value	m/s
\hat{y}_n	Predicted value	m/s
(x_i, y_i)	the position of the particle	-
α	collision efficiency	-
α_{HOMO}	homogeneous collision efficiency	-
α_{HET}	probabilities of successful aggregation	-
α_{sta}	stability ratio	-
μ	dynamic viscosity of the media	mPa·s
u	u-velocity at the location of the particle (x_i, y_i)	m/s
v	v-velocity at the location of the particle (x_i, y_i)	m/s
V	Volume	m ³
ν	kinematic viscosity of water	m ² /s
w	settling velocity	m/s
z	vertical distance	m

ACKNOWLEDGEMENTS

I would like to thank and express my greatest appreciation to my supervisor, Dr. Haibo Niu, for his professional, scientific and continuous guidance and support throughout my PhD study. I really appreciate his encouragement, trust and inspiration that greatly motivated me to work hard, act efficiently and accomplish more. I believe I would embed those nice personality and positive attitude to my life and make further progress in the future.

I also appreciate the comments and suggestions from my committee members Dr. Yongsheng Wu and Dr. Lei Liu. Their expertise and patience helped so much. I am very grateful to Dr. Pu Li, Shihan Li, and other faculty members and staff as well, for their help and contributions to this research.

At last but not least, I would like to show my appreciation to my families for their continuous encouragements and support that allowed me to pursue my goals at scientific research area.

Chapter 1: Introduction

1.1 Background

Despite the critical need to decrease petroleum hydrocarbon consumption, oil products remain vital to our society in the near future due to time required to transition to alternative energy sources in different sectors, especially the marine transportation industry. The production and transportation of oil products carry the inherent risk of oil spills resulting from accidents or operational errors [1]. Marine oil spills, involving crude oils and other petroleum products, pose a significant environmental challenge. According to the International Tanker Owners Pollution Federation (ITOPF), approximately 15,000 tons of oil were spilled from tankers and oil carriers in 2020 [2]. While the frequency of large spills has progressively declined over the past five decades [2], the number of small spills (e.g., the *M/V Marathassa* oil spill in English Bay, BC, in 2015) remains high [3]. Small oil spills typically occur due to improper ship operations and received less public attention than large oil spill events [4]. Nonetheless, both large and small oil spills are considered major forms of marine pollution, often resulting in significant, long-term impacts on the environment, ecology, and socio-economic in the affected areas. Consequently, local authorities and oil companies strive to develop comprehensive contingency plans to mitigate the adverse effects of oil spills. Precise monitoring of the fate and trajectory of spilled oil is crucial for rapid and effective spill response.

Oil spill models are computational tools designed to predict the trajectories and fate of spilled oil. Despite significant advancements in oil spill model development, recent state-of-the-art reviews have identified limitations in existing models [5,6]. For instance, processes such as dissolution, vertical mixing, oil sedimentation, photo-oxidation, and biodegradation are often neglected in current oil spill models [5]. Additionally, the transport algorithms in these models are incapable of predicting the fine-scale structure of spills, which could significantly affect the spill distribution and subsequent transport [6]. Among these limitations in oil spill modelling, this study focuses on addressing the shortcomings related to oil sedimentation and oil transport prediction.

Upon discharge into the water, the majority of oil mass exists as droplets [7,8]. Parts of the volatile components evaporate in the initial hours of the spill. Volatile components partially evaporate during the initial hours of the spill, leaving behind heavier components that can interact with sediments in the water column. These interactions form oil-mineral aggregates (OMA) through adsorption or incorporation into the sediment phase due to capillarity and surfactant ions [9–12], or through direct aggregation resulting from collisions [13–15], ultimately leading to oil sedimentation [16]. Poirier and Thiel (1941) first proposed the potential interactions between oil and mineral particles in an aqueous medium, suggesting that kaolinite should be the most efficient mineral for oil-mineral interactions. However, oil-mineral interactions in natural environments were first observed during cleanup operations following the Exxon Valdez spills in 1989, when they were postulated as “clay-oil flocculation” [18,19]. Researchers hypothesized that

spilled oil could be removed from the water column through the natural cleaning and removal process of "clay-oil flocculation" even in low-energy environments [18–21]. This hypothesis was confirmed after the Tampa Bay spill in Florida in 1993 and the Sea Empress Spill in Wales in 1996. Subsequently, the interaction between oil and mineral particles was redefined as "oil-mineral aggregation (OMA)" because clay-sized minerals ($<2 \mu\text{m}$) were not considered responsible for OMA formation [22,23].

OMA formation has been documented in various environments and numerous oil spills. For example, in 1989, approximately 41 million liters of Alaska North Slope crude oil spilled into Prince William Sound, with a portion of the spilled oil naturally removed through OMA formation [18–21]. In 2010, over 3.2 million liters of diluted bitumen transported by the Enbridge Line 6B pipeline were released into Michigan's Kalamazoo River, where a large amount of the spilled oil (heavy component) interacted with sediments to form OMA along channel margins, backwaters, and oxbows [24]. The extensive cleanup and environmental remediation efforts cost around 1.2 billion dollars in 2014 [24]. Although majority of the spilled oil being collected, the spill continues to have long-term environmental impacts. Consequently, understanding the formation, settling, and transport of OMA is critical for effective cleanup and long-term assessment of oil spills.

OMA formation is an important process that naturally transports oil from one environmental compartment to another, enhancing oil dispersion [20–22]. The formation process is affected by many factors, including the oil properties (type,

droplet size, and oil concentration), particle properties (size and shape, its organic matter content, density, and concentration), and ambient condition (i.e. mixing energy, salinity, and temperature) [25]. While considerable efforts have been made to study OMA formation under various conditions, many results are conflicting [26]. For example, regarding the effect of salinity on OMA formation, several studies have demonstrated a strong impact at low salinity levels (0 - 5 ppt) with no significant effect observed with further salinity increases [27–30]. Conversely, Guyomarch et al. (1999) found that increasing salinity from 10 to 50 ppt significantly affected OMA formation. It is important to note that different OMA formation studies employed distinct laboratory procedures, introducing considerable variance and uncertainty. Replication of experimental runs has rarely been conducted to present experimental error, making the reported data less reliable [26]. More importantly, despite the complexity of the OMA formation system, no attempt has been made to find out the most influential factors by utilizing statistical design & analysis methods. Additionally, the interaction effects between factors (e.g., the temperature influence might be dependent on the time used) are highly possible to play essential roles during OMA formation [25, 29, 32–34]. Unfortunately, these interactions have not been systematically explored [26]. On the other hand, The rapid development of machine learning algorithms, extensive data mining, and powerful computing resources have advanced scientific research and industrial practices in numerous aspects [35–39], which inspired us to evaluate the feasibility of applying machine learning algorithms for OMA formation prediction.

It is also worth mentioning that OMA settling velocity is significant for modelling the fate and transport of OMA/spilled oil. However, the literature on studying OMA settling velocity remains scarce. The empirical equation for OMA settling velocity estimation relies on the traditional Stokes' Law formula, which assumes OMA particles to be spherical under certain assumptions [40, 41]. Therefore, using Stokes' Law to estimate OMA settling velocity is less reliable, hindering the accuracy of OMA transport modelling. Thus, exploring an alternative method for OMA settling velocity prediction is necessary. Machine learning approaches have recently attracted interest in various research fields, including oil spill related studies. For instance, Cao et al. (2022) aimed to investigate the effects of chemical dispersant and salinity on the biodegradation of spilled oil, and employed machine learning method to quantitative predict the strength of causal links between dispersant addition, salinity, cell abundance etc., in which the positive effect of dispersant addition was suggested, and it was due to the enrichment of cell abundance [39]. The ability to handle large datasets and provide adequate estimation inspired us to explore the feasibility of using machine learning algorithms for OMA settling velocity prediction.

In addition to the oil sedimentation process resulting from OMA formation, improving oil spill trajectory prediction using new techniques is also one of the future directions for oil spill modelling, as mentioned in the recent state-of-the-art review [5,6]. Oil spill trajectory tracking can be done with various existing models, however, following the trajectory of an oil spill or predicting the trajectory with a numerical model in coastal areas is not easy. The trajectory is related to the

pollutant's physicochemical properties and depends on tidal currents and dispersion, and transporting the pollutants through estuaries and coastal environments is also associated with tidal dispersion [42]. Tidal dispersion occurs when the periodic tidal oscillations spread a patch of particles due to the spatial variability of the tidal currents or the background mean flow. This tidal process scatters or dilutes water parcels [43]. Therefore, to accurately predict the trajectory of an oil spill, it's necessary to understand the complex relationship between tidal dispersion and an oil spill's trajectory.

Tidal dispersion is commonly studied using Lagrangian techniques, drifters, and virtual trajectories in a numerical model of ocean flow fields. Over the last two decades, researchers have studied tidal dispersion and its impact on particle transport in estuaries [44–48]. For instance, researchers tracked surface drifters to estimate residence times, dispersion, and trapping in the Salish Sea, and they concluded that dispersion was crucial to particle transport and is often far more important than mean advection [47]. Furthermore, with computer modelling, it has become possible to simulate flow fields with high spatial and temporal resolutions, and, as technology improves and computing power increases, modelling has become a viable, convenient, and economical option for studying dispersion. Several numerical modelling studies on tidal dispersion have been conducted [42, 49, 50], with one study noting that the scale of a tidal excursion length relative to the spacing between major bathymetric and shoreline features was the most important effect of the tidal current on tidal dispersion [42].

The tidal excursion length is the net horizontal distance a water particle travels from slack low water to slack high water, or vice versa [51]. Tidal excursion length is a valuable indicator of hydraulic and mixing characteristics of estuaries [52], and is usually used to study the movement of pollutants in estuaries over a tidal cycle [51, 53–59]. If the tidal excursion were larger than the typical spacing of the topographic features, tidal dispersion could significantly contribute to the flushing of an estuary. Otherwise, the dispersion might only be local without any influence on the overall flushing of the estuary [42].

In addition to the length of the tidal excursion, the residual current of the tide is important to tidal dispersion in an estuary. For instance, Xu and Xue (2011) investigated the tidal circulation in Cobscook Bay at different tidal phases and found that the magnitude of the residual currents and the tidal excursion could estimate the effective dispersion coefficient (the degree of separation of particles within the cluster). Xu and Xue found that small residual currents and short tidal excursion limited the tidal dispersion and produced small effective dispersion coefficients, and large residual currents and long tidal excursion enhanced tidal dispersion and produced large effective dispersion coefficients [50].

Although several advanced methods have been proposed for understanding particle transport using Lagrangian particle trajectories in ocean modelling [60–63], obtaining the Finite-Time Lyapunov Exponent (FTLE) fields and visualizing the FTLE ridges is arguably one of the most powerful tools for investigating spilled oil movement in complex flows [6]. Compared to traditional modelling approaches, calculating FTLE values does not require having high data accuracy or interpolating

the velocity field. Furthermore, FTLE analysis results are not sensitive to data errors. The FTLE method was successfully applied to understand the distribution of pollutants, including spilled oil. For instance, Mezic et al. (2010) employed FTLE to simulate the trajectories of oil spilled in the Gulf of Mexico, and the simulation results were consistent with the observations reported by NOAA (National Oceanic and Atmospheric Administration) [64]. Unfortunately, there are no comprehensive studies using the FTLE method, residual currents, and tidal excursion length to track spill trajectories.

1.2 Research Objectives

This research aims to study oil spill transport by examining OMA characteristics and tidal dispersion properties. The OMA formation, settling, and transport characteristics are investigated through laboratory experiments and numerical simulations, while the tidal dispersion properties are analyzed using the Finite-Time Lyapunov Exponent (FTLE) method. The specific objectives are as follows:

- 1) Systematically investigate OMA formation under various conditions to identify significant factors and interaction effects;
- 2) Precisely measure OMA settling velocity and explore the influence of external environmental factors;
- 3) Compare the prediction accuracy of traditional numerical modelling and machine learning algorithms for determining OMA median diameter and settling velocity;

- 4) Evaluate the feasibility of using FTLE analysis as a tool to aid in oil spill transport modelling.

1.3 Thesis Organization

Chapter 2 presents a literature review on the oil-mineral-aggregates' formation, settling and modelling, as well as the FTLE related studies. **Chapter 3** provides the details of the materials and methodologies employed. **Chapter 4** identifies the most influential factors for the OMA formation and compares the collision theory and machine learning prediction for OMA median diameter. In **Chapter 5**, the settling velocity of OMA is comprehensively quantified, correlated with environmental conditions, and estimated using both traditional empirical equations and machine learning algorithms. Furthermore, the sensitivity of OMA deposition to settling velocity prediction is investigated by conducting particle tracking modeling. **Chapter 6** presents the details of FTLE analysis in Burrard Inlet, Vancouver, which is thoroughly compared with a real oil spill (*M/V Marathassa* oil spill) that occurred in Burrard Inlet. Finally, **Chapter 7** provides the overall conclusions of this research and the recommendations for future work.

Chapter 2: Literature Review

Copyright permission:

A version of this chapter has been published in J. Mar. Sci. Eng., 10(5), 610. The copyright has been obtained from the Journal of Marine Science and Engineering and co-authors.

Contribution statement:

I was responsible for literature searching, data summarization and analysis, table and figure preparation, and manuscript drafting.

2.1 General Information on Oil Spill

Once oil is discharged into the water environment, two common transformation processes can occur as follows. One is the oil weathering process that can significantly change the physicochemical properties of the spilled oil. Another one is the oil movement in the water environment that can increase the contamination area.

Oil weathering refers to oil spreading, evaporation, emulsification, and natural dispersion, followed by dissolution, photooxidation, biodegradation, and sedimentation [65]. Each process happens at different times and varying rates. For example, oil evaporation begins immediately when the oil slick first presents on the water surface. Oil evaporation is a relatively short process. In contrast, oil emulsification is a long process that begins relatively slowly [66]. Furthermore, different weathering processes have different impacts on the physicochemical properties of the spilled oil. Among these processes, photooxidation and

biodegradation are the most critical for modifying the chemical compositions of spilled oil [65,67]. Moreover, as evaporation decreases the volume of the spilled oil, it also increases the oil's density [68]. After evaporation, the remaining heavy components of a lighter oil can combine with sediments in the water column and subsequently sink to the bottom. The oil remaining at the surface naturally disperses into the water column [16]. Lastly, oil emulsification depends on the types of oil and conditions in the surrounding environment. Emulsification changes the oil's physical properties, such as water content and viscosity [69].

Knowing how spilled oil moves on the water surface is important to oil spill modelling. Spreading is one of the most critical movement processes because spreading oil can increase the size of the contaminated area [66]. Furthermore, gravity and oil-water interfacial tension can help the spilled oil spread into a slick over the water surface [65]. The effects of gravity could gradually diminish over time, but the oil would continue to spread under the effects of interfacial tension [70]. The spreading rate of spilled oil is closely related to environmental conditions, such as tidal streams, water currents, coastlines, and wind speeds, as well as being related to oil properties [66,71–73]. For instance, in a confined waterway, it is difficult for spilled oil to spread quickly to reach the shoreline [74], but, in the open ocean, spilled oil can spread rapidly and widely to cover a large area in a short period [66]. Moreover, spilled oil that has lower molecular weight components presumably spreads more quickly [66]. Additionally, spreading depends on oil weathering. For example, evaporation and dissolution can reduce the area covered by the spreading oil [73].

Oil advection at the sea surface and into the water column is another crucial movement process and mainly depends on ocean currents, wind, and waves. The effects of the wind and currents on spilled oil depend on the spill location and hydrographic conditions.

Various oil spill models have been developed to track the fate and behavior of spilled oil. These oil spill models are classified as oil weathering models or trajectory/deterministic models. Oil weathering models (OWM) do not consider oil transport and only simulate oil weathering processes. For instance, The ADIOS2 (Automated Data Inquiry for Oil Spills, Silver Spring, MD 20910, USA) oil weathering model, which was developed by NOAA, mainly includes the weathering processes of evaporation, dispersion, emulsification, spreading, and sedimentation. ADIOS can also assess how effective clean-up techniques would be [75,76]. The IKU Oil Weathering Model, which was developed by SINTEF, is also commonly used. The IKU OWM is also known as SINTEF OWM. SINTEF OWM is developed based on small and mesoscale laboratory tests and full-scale field experiments [77,78]. SINTEF OWM considers emulsification, natural dispersion, and evaporation as its main weathering processes. The model applies a pseudo-component method to calculate how much oil is lost to evaporation, and Mackay's equation evaluates the viscosity of the emulsified oil [79,80]. It is also worth mentioning that nearly 200 different types of oil have been characterized by the SINTEF laboratory in Norway, all of which are included in SINTEF OWM [81]. More specialized weathering models, such as the Diluted Bitumen Weathering Model (DBWM), have been developed and recently validated against meso-scale

experimental data to simulate the weathering of unconventional crude products such as diluted bitumen [82].

Trajectory/deterministic models are grouped as two-dimensional (2D) and three-dimensional (3D) models [83]. A 2D model only simulates the trajectory of spilled oil at the water’s surface, whereas a 3D model tracks the spilled oil at the surface and in the water column. Various algorithms have been developed for trajectory/deterministic models, including Eulerian methods, Lagrangian methods, and Eulerian–Lagrangian methods (ELMs). According to state-to-the-art reviews [6,83,84], Lagrangian methods are the most popular algorithms for 3D oil spill models. For instance, the COSMoS model developed by Environment and Climate Change Canada [85] and SPILLCALC developed by Tetra Tech EBA [86] use Lagrangian algorithms. Table 2.1 lists examples of 3D models that use Lagrangian algorithms.

Table 2.1 Examples of 3D oil spill models that use a Lagrangian algorithm to simulate oil transport.

Model	Developer	Reference
COSMoS	Environment and Climate Change Canada (ECCC)	[85]
COZOIL	Department of the Interior Minerals Management Service	[87]
GNOME Suite	National Academies of Sciences, Engineering, and Medicine (NOAA)	[88]
GULFSPILL	KFUPM/RI	[89]
MEDSLIK / MEDSLIK-II	Oceanography Centre of the University of Cyprus (OC-UCY)	[90–92]
MIKE 21/3	Danish Hydraulic Institute (DHI)	[93]
MOHID	MARETEC (Marine and Environmental Technology Research Center)	[94]
MOTHY	Météo-France	[95]
OILMAP/SIMAP	ASA	[96, 97]

Model	Developer	Reference
OILTRANS	The Atlantic Regions' Coastal Pollution Response (ARCOPOL)	[98]
OpenDrift / OpenOil	Norwegian Meteorological Institute	[99, 100]
OSCAR	SINTEF	[101]
POSEIDON-OSM	Hellenic Centre for Marine Research (HCMR)	[102, 103]
SPILLCALC	Tetra Tech EBA	[86]

Oil spill models can also be classified based on their purpose. After the Deepwater Horizon oil spill, Ainsworth et al. (2021) categorized and summarized 330 published modelling applications (between 2010 to 2020) developed by the Gulf of Mexico Research Initiative (GOMRI), the Natural Resource Damage Assessment (NRDA), and other researchers. Ainsworth et al. (2021) classified the models by (1) circulation/mixing, (2) abiotic transport (far field), (3) oil fate, (4) biotic transport, (5) biological impacts, (6) other plume dynamics, (7) turbulence/local mixing, (8) water chemistry, (9) atmosphere, (10) oil spill response support, and (11) other [63]. Furthermore, Keramea et al. (2021) summarized commonly used models based on model capabilities and purpose. Keramea et al. (2021) classified the oil spill models into: (1) surface oil spill models and blowout/buoyant plume models, (2) operational response models, (3) deep sea blowout/buoyant plume models, and (4) models with spill response and environmental impact assessment support. Zhao et al. (2021) evaluated algorithms for oil spreading, evaporation, emulsification, dispersion, dissolution, biodegradation, and photooxidation. We note that sedimentation (OMA formation and transport) is absent in all the 2D and most 3D oil spill models. The 3D models

that include sedimentation usually describe it with simple coefficients and do not have detailed sedimentation algorithms.

2.2 Factors Influencing OMA Formation

When oils were spilled into a marine environment, a significant portion of the oil could be dispersed as oil droplets [7, 8]. These oil droplets can interact with the suspended sediments in the water column to form oil-mineral-aggregates (OMA) as shown in Figure 2.1.

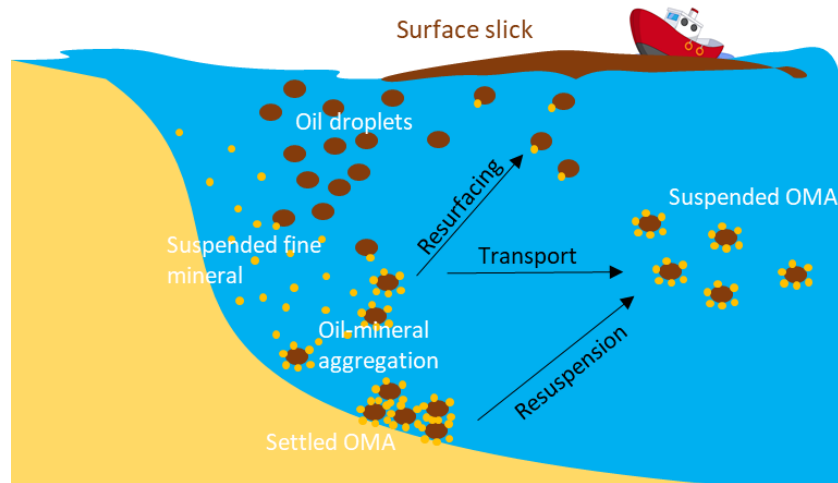


Figure 2.1 Formation of OMA in the nearshore environment adapted from [106].

OMA formation is affected by many factors, including oil properties (type, droplet size, and concentration), particle properties (size and shape, organic matter content, density, and concentration), and ambient conditions such as mixing energy, salinity, and temperature [25]. It has been reported that the average aggregate size is positively correlated to the oil-particle ratio (g oil/g sediment) [33]. However, when only considering sediment concentration, the relationship between particle concentration and the average aggregate size fits a Gaussian distribution with the

highest average aggregate size of $\sim 1400 \mu\text{m}$ at a particle concentration of 0.8 g/l [33]. Kehlifa et al. (2015) showed that normalized cumulative size distributions of OMA are like the size distributions of mineral-free oil droplets formed in seawater.

In terms of the oil viscosity's influence on how OMA form, Wood et al. (1998) observed that the aggregation rate of OMA is greater as the oil viscosity and density decrease. However, Khelifa et al. (2002) indicated that oil viscosity has a negligible effect on OMA's maximum and mean sizes.

The types of clay in the suspended sediment impacts how OMA form. Zhang et al. (2010) and Wang et al. (2011) found that the size of an OMA increases as the minerals change from hydrophilic to hydrophobic. The OMA's size increases from a few micrometers for a natural kaolin (hydrophilic) to tens of micrometers for a modified kaolin (hydrophobic). The change in size occurs because the hydrophobicity of minerals promotes the affinity of minerals to oil, which enhances the formation of OMA. Khelifa et al. (2005) also stated that the clay type was crucial for the OMA's size, which was even more influential compared to the effect of oil type.

The effect of salinity on how OMA form is controversial. Several studies illustrate that low salinity ($0\text{--}5 \text{ ppt}$) strongly influences OMA formation, and no significant effect exists for greater salinity increases [27–30]. For instance, Le-Floch et al. (2002) reported that the proportion of oil in an OMA increases as the salinity increases, but the oil content stabilizes when salinity is greater than $\sim 2 \text{ ppt}$. Khelifa et al. (2005) illustrated that the median and maximum size of OMA increases significantly as the salinity increases from 0 ppt to 1.2 ppt , but a further

increase in salinity to 3.5 ppt decreases the OMA's size. However, Payne (1989) found the opposite result: an OMA forms more quickly with salinities of 15 and 30 ppt than in freshwater. Furthermore, Guyomarch et al. (1999) reported that the OMA formation rate slows as salinity increases from 10 to 50 ppt. Theoretically, the effects of salinity on OMA formation occur because of the change in the electrical double-layer thickness of the oil and mineral particles. As salinity increases, the layer thickness compresses, which reduces surface repulsion and increases the inter-particle attraction between the oil and mineral. However, the influence of salinity on OMA formation is minimal once the layer thickness is below a threshold as the level of salinity in the water rises. Therefore, OMA formation eventually peaks and stabilizes as the salinity increases [28].

Mixing energy is an important environmental factor that influences the size of OMA [32, 108, 111–113]. An adequate mixing energy promotes the interaction between dispersed oil droplets and suspended particles so that OMA can form [113]. On the other hand, an OMA could break apart if the mixing energy is too aggressive [108]. Ji et al. (2021) conducted a series of laboratory experiments to investigate the impact of mixing energy on the time it takes for OMA to form. They suggested that the collision efficiency between oil and sediments under a higher mixing energy rate (200 rpm) is three times higher than under a lower mixing energy rate (150 rpm). High mixing energy results in rapidly forming OMA during the first 3 h, followed by the OMA breaking apart. Ji et al. (2021) found that, after 24 h of mixing, only in low energy mixing cases would the dispersed OMA reform because there would be more oil droplets on the water's surface.

As a human initiated influence, chemical dispersants are key to OMA formation. Page et al. (2000) carried out a series of wave tank experiments to study the effectiveness of using dispersants as an oil spill chemical countermeasure in the surf zone. Their experiment results indicated that chemically dispersed oil associates less intensively with mineral matter than physically dispersed oil [7]. Zhang et al. (2010) found that applying chemical dispersants is a dominant factor in how OMA form and behave. Several wave tank experiments conducted by Lee et al. (2008) indicated that chemical dispersants reduce surface tension between the oil and water and stimulate interaction between oil and fine mineral, eventually increasing the concentration of OMA. Lee et al. (2008) also indicated that the chemical dispersants reduce the size of OMA to a mean diameter of 15–25 μm . However, Khelifa et al. (2008) observed that chemical dispersants enhance the stickiness of oil to lead to larger OMA, probably due to the surfactant coating the oil droplets. Fu et al. (2014) carried out roller table experiments to explore how marine oil snow forms when a stereotype oil dispersant (Corexit EC9500A) is present. Fu et al. (2014) found that adding the chemical dispersant enhances particle aggregation and formation of marine snow. O’Laughlin et al. (2017) claimed that dispersants delay flocculation of natural sediments and create a surplus of available sediment to interact with oil droplets and potentially form OMA.

2.3 OMA Settling

The settling velocity of OMA mainly depends on their composition densities. The buoyancy of OMA should cause OMA to rise to the surface if the composition is mainly oil; otherwise, the OMA composed primarily of sediment

should sink to the benthic layer [14]. A better understanding of OMA settling is critical to predicting the fate and transport of OMA.

Despite its importance, the literature on studying OMA settling and trajectory is still rare. There are only a few attempts to study OMA settling and transport as shown in Table 2.2. Muschenheim and Lee (2002) investigated the amount and rates of OMA formation and settling velocities by using a focused flow reactor. They reported that large (100 to 200 μm) OMA have settling velocities ranging from 2.2 to 10.4 mm/s. Waterman and Garcia (2015) tested settling velocities by using a 1.6 m height Plexiglass settling column and observed that the OMA had settling velocities between 1.0 and 11.2 mm/s, with the majority being between 1.0 and 3.0 mm/s. O’Laughlin et al. (2017) conducted experiments to measure the variability in particle size and settling velocity of OMA in response to sediment concentrations and presence/absence of chemical dispersants. O’Laughlin et al. (2017) found that OMA size, settling velocity, and effective particle density increase under a higher concentration of suspended sediment (comparing 10 mg/L with 50 mg/L), which indicates that high concentration suspension produces large, inorganic-derived flocs that settle rapidly. Their results also suggested that dispersants inhibit natural sediment flocculation. Ye et al. (2020) conducted laboratory experiments to investigate the influence of clay types on OMA structures and settling velocities by using the LabSFLOC-2 system and digital microscopy. Ye et al. (2020) found that for low stickiness Kaolinite clay, droplet OMA form with much smaller settling velocities than the settling velocities of pure Kaolinite flocs. Furthermore, Ye et al. (2020) found that high stickiness Bentonite clay,

generates flack/solid OMA with settling velocities greater (by 25%) than settling velocities of pure Bentonite flocs.

Table 2.2 Summary of laboratory experiments on the OMA settling velocity.

References	Main objectives/methods	Results
[117]	To measure OMA settling velocities by using a focused flow reactor	Settling velocities ranging from 2.2 to 10.4 mm/s for 100-200 um OMA
[118]	Settling velocity tests were conducted in a 1.6 m height Plexiglass settling column.	Settling velocities between 1.0-11.2mm/s, with the majority being in the range between 1.0-3.0mm/s.
[41]	Sediment concentration influences settling velocity	The higher concentration of suspended sediment (10 vs. 50 mg/L), the greater settling velocity and effective particle density
[40]	To explore the effect of clay type on OMA structure and settling velocity by using the LabSFLOC-2 system and digital microscopy	For low stickiness Kaolinite clay, the OMA settling velocity was about a factor of two smaller than the pure Kaolinite flocs; For high stickiness Bentonite clay, the OMA settling velocity was greater than the pure Bentonite flocs

2.4 Modeling OMA Size Distribution

The size of OMA can vary from a few micrometres to hundreds, even thousands of micrometres [33, 108, 112, 113]. The range of sizes of OMA illustrates the complexity of OMA formation. This complexity encouraged scientists to develop sophisticated numerical models to predict how OMA form and

subsequently transported. However, modelling OMA formation and transport is still at an early stage and the ability of the models to accurately predict either process is limited. In most oil spill models, only the ratio of mineral-stabilized oil is computed from standard equilibrium partitioning theory (by using a dimensionless coefficient), and the concentration of suspended particle matter in the water column is just estimated [6]. Therefore, there is still a need to develop even more advanced OMA models that can be incorporated into existing oil spill models.

With regards to modelling OMA formation, the population balance equation, based on collision theory between oil droplets and suspended sediment materials, is currently widely used [15, 29, 119–122]. The population balance equation for particle collision due to Brownian motion was first proposed by Smoluchowski (1918) and is listed as Equation (1) in Table 2.3. After Smoluchowski developed their equation, other physical mechanisms, such as shear turbulence and differential settling, were included in the modelling (Equation (2) in Table 2.3) [124]. Sterling et al. (2004) extended the population balance equation to simulate the changes in particle size distribution and density due to aggregation (Equations (3) and (4) in Table 2.3). Sterling et al. (2004) conducted batch flocculation experiments and introduced an algorithm to estimate homogeneous collision efficiency values (α_{HOMO}) to account for the effects of particle types on OMA formation. Furthermore, Sterling et al. (2004) found that α_{HOMO} is greater for clay (0.7) and crude oil (0.3) compared to silica (0.01); thus, they classified clay and crude oil as cohesive particles and classified silica as a non-cohesive particle. In addition, they

found that heterogeneous collision efficiency values (α_{HEMO}) is similar for oil-clay (0.4) and oil-silica (0.3), suggesting that crude oil increases the aggregation of non-cohesive silica particles [15]. However, the Sterling et al.'s model utilized a looped term to represent oil–oil, oil–particle, and particle–particle interactions, mainly because the laboratory operations probably could not distinguish between the interactions. Moreover, Sterling et al. (2004) did not include an OMA breakup process in their model.

Same as Sterling et al.'s model, breakup is also neglected in several other OMA formation models [119, 122, 125, 126]. For instance, Bandara et al. (2011) developed a numerical model by using a three-dimensional (3D) advection-diffusion equation to simulate oil-sediment interaction (Equation (5) in Table 2.3). They used the Lagrangian Parcel (LP) method to reduce their program size and to operate more efficiently. Bandara et al.'s simulations showed that up to 65% of released oil can be removed from the water column as OMA. When oil droplets and sediment particles are smaller than 0.1 mm, more OMA form. Bandara et al. (2021) also stated that their lacking knowledge of oil sediment aggregation collision efficiencies, sediment aggregation efficiencies, and oil partitioning led to some uncertainty in their results, and more laboratory and field experimental work/data would further test and improve their model's adequacy [119]. Zhao et al. (2016) developed the A-DROP model, based on the population balance equation, by introducing a new formulation of oil-mineral coagulation efficiency (Equation (6) in Table 2.3) to account for the coated areas on the surface of oil droplets, the effects of hydrophobicity, and the ratio of particle to droplet size. The Zhao et al.

(2016) formulation satisfactorily estimates oil trapping efficiency by incorporating the effects of shape and packing on OMA coagulation. They suggested that increasing particle concentration in the swash zone quickens oil–particle interaction, but the amount of oil trapped in the OMA does not correspond to the increasing particle concentration [122]. Recently, Cui et al. (2021) developed an OMA formation model, OPAMOD, within the Coupled Ocean-Atmosphere-Wave-and-Sediment Transport (COAWST) modelling system, by modifying the existing population balance equation (Figure 2.2). The authors performed sensitivity tests on fractal dimension and collision efficiency by using the OPAMOD model. They stated that fractal dimension is important to OMA size distribution because fractal dimension influences the effective particle density; however, collision efficiency has less impact on the size distribution [125].

Although the size distribution of OMA is successfully simulated by the models that do not include disaggregation, the OMA breakup process is still valuable when modelling OMA formation. Khelifa’s group developed a Monte Carlo simulation model (involving disaggregation) to predict OMA size distribution based on a population balance equation [120, 121, 127]. The Monte Carlo method (Equation (7) in Table 2.3) is applied as a probabilistic tool to solve the model. The specific event, aggregation or disaggregation, is selected randomly at each step during the simulation. The simulation stops once equilibrium is reached. Khelifa et al. (2005) suggested that it is appropriate to integrate their new breakage model to describe oil droplet formation. The maximum permissible size of the oil droplets in their simulation is the key physical input of the model and can be

upgraded by integrating an empirical-theoretical model [127]. We note that this model predicts the particle size distribution well, but information about oil (mass) in OMA, needed for further risk assessment, is unavailable. In addition, the conceptual time to run the Khelifa et al. model using the Monte Carlo method is unknown.

In addition to the size distribution of the OMA, other parameters important to OMA formation, such as the time scale of formation [128,129], oil trapping efficiency [28, 130, 131], and oil sinking rate [132], have been studied and predicted. Hill et al. (2002) presented Equation (8) (Table 2.3) to define the time required to form stable OMA. They stated that OMA formation can occur over a short time scale. Among all their simulations, about 7% of the required times were shorter than 30 s, and 10% were longer than a day. In their modelling, when sediment concentration was high and droplets were large, the OMA formation time was the shortest. Hill et al. (2002) also suggested that their equation is suitable for the coastal zone. Ajijolaiya et al. (2006) developed Equation (9) (Table 2.3) to describe oil trapping efficiency. They found that trapping efficiency increases with improving sediment concentration and decreasing sediment size. Ajijolaiya et al. (2006) also stated that maximum trapping efficiency occurs when the range of sediment concentrations is near unity. Wang et al. (2019) conducted several experiments and developed an empirical equation to calculate oil trapping efficiency as a function of sediment concentrations (Equation (10) in Table 2.3). Their simulation results indicated that the formation rate of OMA depends on sediment concentration, mixing time, salinity, and the use of a chemical dispersant

in the water column. Wu et al. (2016) developed a simple approach to estimate the sinking rate of spilled diluted bitumen (Equation (11) in Table 2.3). They suggested that the sinking rate is impacted by the density of oil, sediment, water, and oil size distribution.

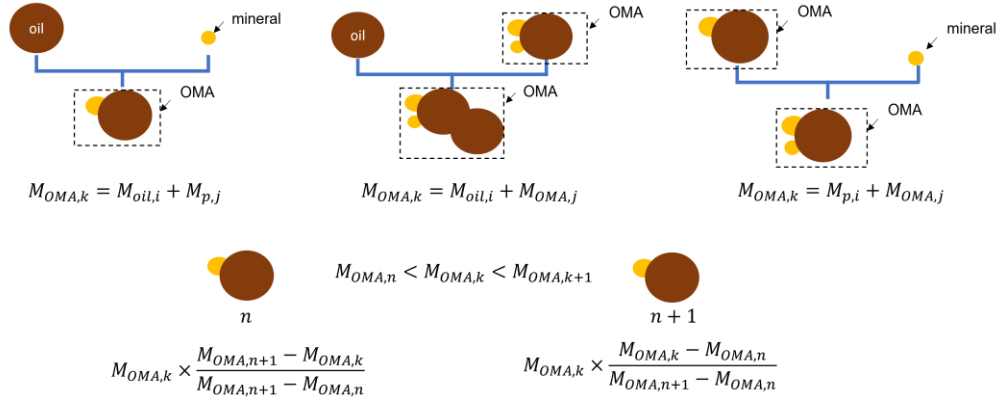


Figure 2.2 Schematic of OMA formation model adapted from Cui et al. (2021).

2.5 OMA Transport Modelling

The transport of OMA is critically important to oil spill modelling. Some models have already been developed to simulate OMA transport [14,15,119,126,133–137]. The fate and transport of OMA have been typically modeled by implementing the advection-diffusion equation and a random walk model. For example, as we noted before, Bandara et al. (2011) used the Lagrangian Parcel (LP) method to develop a model based on the 3D advection-diffusion equation to predict the fate and transport of OMA. The model simulates six processes: advection and diffusion of oil and sediments, dissolution of oil, aggregation of sediments, aggregation of oil-sediment particles, oil partitioning, and deposition of sediment and OMA. Unfortunately, Bandara et al. (2011) made

some assumptions due to their lacking knowledge of oil sediment aggregation efficiencies, sediment aggregation efficiencies, and oil partitioning [119].

Niu and Lee (2013) used a 3D random walk model to simulate the transport of OMA under hydrodynamic conditions involving wave-induced velocities, random velocities due to turbulence, and a settling velocity due to gravity (Figure 2.3). In their model, they use a fixed number of particles to represent the OMA at the spill site at the beginning of a simulation. Then, the particles move on each subsequent time-step, according to Lagrangian motion, while the OMA size distribution is artificially defined. [135]. Jones and Garcia (2018) avoided having to artificially define the size distribution by combining the random walk model with the A-DROP model to simulate the fate and transport of OMA. The Jones and Garcia's model simulates the interactions between oil droplets and sediments during their residence time in a river, which informs the user under what conditions the oil is more likely to coagulate with suspended sediment. However, Jones and Garcia neglected the re-entrainment of settled OMA [126].

The settling velocity of OMA is one of the most important parameters when modelling OMA transport. There are equations that calculate settling velocity [119, 122, 133, 135, 138]. Winterwerp (1998) developed the most widely used settling velocity equation basing it on Stokes' formula (Eq. (12) in Table 2.4). Winterwerp's equation is suitable for spherical, massive particles in Stokes's regime ($Re \leq 1$). This settling velocity equation integrates a particle tracking model or an advection-diffusion equation. Integrated model's simulation results compare favorably with laboratory observations [119, 139]. Later, Zhao et al. (2015) improved the

Winterwerp's equation by expanding the applicable flows ($1 \leq Re \leq 10^4$ and $Re > 10^4$) as shown in Equation (13) (Table 2.4). Zhao et al.'s predicted settling velocity is also consistent with experimental data [122, 140]. Niu et al. (2011) developed a simple regression equation (Equation (14) in Table 2.4) to simulate the settling velocity relative to OMA diameter. Niu et al. (2011) also provide equations to estimate the concentration of the settled OMA and the oil content in each particle as shown in Equation (15) in Table 2.4 [135, 141]. However, the Niu et al.'s equations are only suitable for specific conditions.

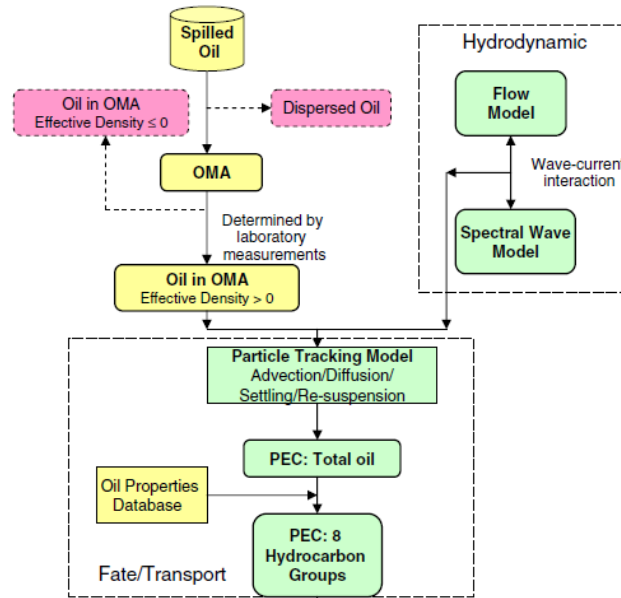


Figure 2.3 Flowchart of the model system adapted from Niu et al. (2011) with permission.

Table 2.3 A summary of equations relevant to the modelling of oil-mineral-aggregates formation.

Eq. #	Equations	Denote	References
1	$\theta = \frac{dn_k}{dt} = \frac{1}{2} \sum_{i+j=k} \alpha\beta(i,j)n_in_j - n_k \sum_{i=1}^{\infty} \alpha\beta(i,k)n_i$	<p>α is the collision efficiency, β is the collision frequency, and n_i, n_j are the particle concentrations for the particle of size i and j respectively.</p>	[123]
2	$\beta = \beta_{Br} + \beta_{sh} + \beta_{ds}$ $\beta_{Br} = \frac{2kT}{3\mu} \left(\frac{1}{d_i} + \frac{1}{d_j} \right) (d_i + d_j)$ $\beta_{sh} = \frac{G}{6} (d_i + d_j)^3$ $G = \left(\frac{\varepsilon}{\mu} \right)^{0.5}$ $\beta_{ds} = \frac{\pi}{4} (d_i + d_j)^2 U_i - U_j $	<p>β_{Br}, β_{sh}, and β_{ds} are the collision efficiency due to Brownian motion, fluid shear, differential sedimentation respectively. k is the Boltzman's constant; T is the absolute temperature, and μ is the dynamic viscosity of the media, d_i and d_j are the effective particle diameters. G is the root mean square of the velocity gradient. ε is the dissipation rate. U_i and U_j are the settling velocity of the two collided entities of size d_i and d_j.</p>	[15, 122, 133]
3	$\frac{dn_{k,q}}{dt} = D_z \frac{\partial^2 n_{k,q}}{\partial Z^2} - w_{k,q} \frac{\partial n_{k,q}}{\partial Z} + \theta_{k,q}$	<p>$n_{k,q}$ is the particle size distribution, k is particle volume, q is effective density; z is the vertical distance; D_z is the vertical dispersion coefficient; $w_{k,q}$ is the settling velocity; $\theta_{k,q}$ is the interaction term due to coagulation.</p>	[133]

Eq. #	Equations	Denote	References
4	$\alpha_{obs}(o,p) = \alpha_{HOMO,1}(sf_{1,o})(sf_{1,p}) - \alpha_{HOMO,2}(sf_{2,o})(sf_{2,p}) - \alpha_{HET,1-2}(sf_{1,o}sf_{2,p} - sf_{1,p}sf_{2,o})$	<p>$sf_{1,o}$, $sf_{2,o}$, $sf_{1,p}$, and $sf_{2,p}$ are surface fractions of constituent particles 1 and 2 in aggregate with density o and constituent particles 1 and 2 in aggregate with density p; $\alpha_{HOMO,1}$, $\alpha_{HOMO,2}$, and α_{HET} are probabilities of successful aggregation through contacts of floc constituent types 1-1, 2-2, and 1-2.</p> <p>For $i=1-5$; correspond to 5 species mentioned in assumptions; $k = 1, 2, 3$; correspond to directions of x, y, z; C_i = volumetric concentration of the ith species; u_k = component of current velocity in x, y, and z directions; w_{si} is the buoyant/settling velocity of the ith species; E_k is the diffusion coefficient of kth direction;</p>	[15]
5	$\frac{\partial C_i}{\partial t} + \frac{\partial(u_k C_i)}{\partial x_k} = \frac{\partial(E_k \frac{\partial C_i}{\partial x_k})}{\partial x_k} + w_{si} \frac{\partial C_i}{\partial x_3} + S_{i,Agg} + S_{i,De} + S_{i,Abs}$	<p>$S_{i,Agg} = \frac{\partial C_i}{\partial t _{Agg}}$ = source/sink terms of the ith species due to aggregation; $S_{i,De} = \frac{\partial C_i}{\partial t _{De}}$ = sink term due to deposition of the ith species; and $S_{i,Abs}$ = source/sink term for the ith species due to partitioning.</p>	[119]

Eq. #	Equations	Denote	References
6	$\alpha(t) = \alpha_{sta} \left(1 - \frac{\sum A_{p-proj} \text{ in OMAs}}{F_{SP} \sum A_o} \right)$	α_{sta} is the stability ratio, A_o is the surface area of an oil droplet; A_{p-proj} is the projection area of particles on the droplet surface when an OMA is formed; and F_{SP} is a factor to account for particle shape and packing effects on the coagulation process.	[122]
7	$P_{brk} = \begin{cases} 0, & n_b = 0 \\ 0.5, & n_b = 1 \\ 1, & n_b > 1 \end{cases}$	n_b is the number of droplets larger than the maximum allowed D_{max} . A breakage process is chosen when two or more droplets larger than D_{max} . $P_{agg} = 1 - P_{brk}$. A random number r_l is selected from a uniform distribution between 1 and 0. A breakage event is selected if $P_{brk} \geq r_l$, otherwise an aggregation event is selected.	[120, 121, 127]
8	$\frac{dN_s}{dt} = -0.16\alpha_{os}(D_s + D_o)^3(\varepsilon/\nu)^{\frac{1}{2}}N_sN_o$	D_s is sediment diameter; D_o is oil droplet diameter; N_s is OMA number concentration. α_{os} is the collision efficiency; ε is the dissipation rate; ν is the kinematic viscosity of water.	[128]
9	$E = \frac{E_{max}(\frac{C_s}{C_{s50}})^n}{1 + (\frac{C_s}{C_{s50}})^n}$	E_{max} is the maximum possible trapping efficiency, C_s is the mass concentration of sediment, C_{s50} is the sediment concentration at 50% trapping efficiency, n is the shape of the trapping efficiency versus	[130]

Eq. #	Equations	Denote	References
10	$E = \frac{(K_d/10^3) \times SPM}{1 + (K_d/10^3) \times SPM}$	sediment concentration curve. Least-squares fitting of the equation to the experiment data yield $n = 3$, and $E_{max} = 85\%$. E is the oil trapping efficiency; K_d is a distribution coefficient; SPM is the sediment concentration	[131]
11	$SR = \frac{V_s}{V} = \frac{r_c^{4-s} - r_{min}^{4-s}}{r_{max}^{4-s} - r_{min}^{4-s}} \times 100\%$	SR is the oil sinking ratio, r_c is $1/2$ of the critical oil droplets size, r_{max} and r_{min} are the maximum and minimum radii of the oil droplets, $s = 2.3$ based on laboratory data.	[132]

Table 2.4 Equations are used to estimate the settling velocity of oil-mineral-aggregates.

Eq. #	Equations	Denote	References
12	$w_s = \frac{(\rho_s - \rho_w)gD^2}{18\mu}$	w_s is the settling velocity of OMA, D is the diameter of OMA, ρ_w and μ is the density and viscosity of the liquid respectively, ρ_s is the OMA density, and g is the gravity.	[138]
13	$w_s = eD^f$	e and f are regression coefficients.	[141]

Eq. #	Equations	Denote	References
14	$C_{settled} = \sum_{i=1}^k \frac{N_i \times PM_i}{A_{cell}}$ $PM_i = \frac{M_{spilled} \times P_{settled} \times p_i}{n_i}$ $V_{oil} = \frac{\rho_{sediment} - \rho_{OMA}}{\rho_{sediment} - \rho_{oil}} V_{OMA}$	<p>k is the number of particle size classes, N_i is the number of the i_{th}-size class particles in the user specified cell, A_{cell} is the area of the cell, and PM_i is the amount of oil per particle for the i_{th}-class particles. $M_{spilled}$ is the total mass of spilled oil, $P_{settled}$ is the percentage of spilled oil that may be transferred to sediment, n_i is the number of particles used in the simulation for class i, and p_i is the fraction of settled oil (in percentage) carried by the particle class. V_{oil} is the volume of oil in an OMA of class i, V_{OMA} is the volume of OMA, ρ_{oil}, $\rho_{sediment}$, and ρ_{OMA} are the density of oil, sediment, and OMA respectively.</p>	[134]
15	$w_s = \sqrt{\frac{4g \rho_s - \rho_w D}{3C_D\rho_w}}$ <p>If $R_e < 1$, $C_D = \frac{24}{R_e}$ If $R_e > 10^4$, $C_D = 0.34$ to 0.4</p>	<p>C_D is the drag coefficient, R_e is the Reynold number.</p>	[140]

2.6 Finite-Time Lyapunov Exponent (FTLE)

Several advanced methods have been proposed to understand particle transport from Lagrangian particle trajectories in realistic ocean model solutions [60–63]. However, obtaining Finite-Time Lyapunov Exponent (FTLE) fields and visualizing FTLE ridges remains a powerful tool for investigating particle movement in complex flows. FTLE was first proposed by Lorenz (1963) based on the Lyapunov Exponent. Later, Haller (2001, 2002) used the ridges of the FTLE field to derive the Lagrangian Coherent Systems (LCS), representing the boundaries between attracting or repelling particles in flows. The scalar FTLE values indicate the convergence and divergence rate between neighboring particles after a given interval of time at a given location in a time-varying flow field [143]. High FTLE values are shown as ridges in the map of the FTLE field and act as the mathematical definition of LCS, representing the most kinematically active material lines of the flow fields [145, 146], so no flux can cross them. In other words, LCS lines represent transport boundaries in the flow field. Therefore, such methods not only forecast the trajectory of particles but also predict the structures that organize the entire flow, and are important in determining transport mechanisms in unsteady flows [147, 148].

FTLE and LCS have been widely used to understand the unsteady flow transport behavior [143,144,149–155]. For instance, Huhn et al. (2012) compared the trajectories of surface drifters with LCS lines, aiming to study the horizontal Lagrangian surface transport in the Ria de Vigo, an estuary in NW Spain with tidal and wind-driven dynamic. They reported that the drifters' trajectories were in well

agreement with the predicted results in two out of four cases [153]. Moreover, FTLE ridges computed from the model velocity fields were used to mark transport barriers for the drifters, indicating that the FTLE ridges can adequately represent the general circulation in the estuary [153].

FTLE and LCS were also successfully applied to understand the distribution and fate of nutrients, pollution, suspended sediments, and other waterborne planktonic biotas in coastal oceans [156–158]. For example, Fiorentino et al. (2012) used FTLE to understand the influence of tidal mixing on coastal water quality in Hobie Beach. The LCS was extracted from the velocity field produced by a coastal ocean circulation model and compared with the satellite-tracked drifter [155]. They found that the drifter trajectories were in well agreement with the LCSs results [155]. They also provided a likely explanation for the high microbial level in Hobie Beach based on the LCS analysis [155]. Wu et al. (2017) used the nonlinear dynamical system theory to compute the FTLE field, which was then adapted to discuss the spatial features of the dispersion rate due to kelp beds in the Hecate Strait [157]. The results suggested that the presence of kelp beds significantly influenced the spatial structures and FTLE values [157]. The location of FTLE ridges was mainly associated with the sizes of kelp beds rather than the surrounding islands [157]. Moreover, the magnitude of FTLE in the case of kelp effects was lower than that without kelp drag. They concluded that the dispersion rate (high FTLE values) was in a reverse relationship to the interiors' kelp density, but in a positive relationship to the edges' kelp density [157]. Ku and Hwang (2018) studied the influence of vertical mixing and stratification on the transport of suspended

sediment and aquatic micro-organisms. They compared the FTLE results with the conventional Lagrangian particle trajectories and observed that small particles' transport and dispersion patterns were strongly related to the FTLE analysis [156]. Particles were almost trapped and thus transported slowly in the region of the low FELE field [156].

Furthermore, FTLE was used to identify the atmospheric transport pathways to understand the effects of pollutants on weather, climate, and human health by Nolan et al. (2020). Six chemical species, water vapor (H_2O), sulfur dioxide (SO_2), ozone (O_3), sulfate (SO_4^{2-}), nitrogen dioxide (NO_2), and sodium (Na^+), were studied [159]. FTLE analysis revealed that the transport pathway of water vapor, sulfur dioxide, Ozone, and sulfate was strongly correlated in the troposphere. In contrast, the near surface winds mainly influenced the transport pathway of nitrogen dioxide [159]. Suara et al. (2020) used FTLE to describe the fate of floating material in a coastal tidal embayment, Moreton Bay. The results indicated that FTLE was able to unveil the likely pathways for floating transport [160]. The flow structure and the location of saddle points varied in different tidal phases [160]. The authors also studied the effects of wind on the LCS and suggested that wind increased the contraction and expansion rate in the vicinity of the barrier, decreased the mixing strength, and changed the particle transport directions [160]. Ghosh et al. (2021) utilized FTLT to predict areas of spontaneous material accumulation in Moreton Bay. They identified 11 potential areas of spontaneous and persistent accumulation of material in Moreton Bay based on the frequency of FTLE. The authors compared the FTLE results with the debris collected data and

found that the identified areas were consistent with the recorded debris accumulation regions [161].

2.7 Machine Learning Algorithms

Machine learning, a subset of artificial intelligence, can construct predictive and empirical classification models without making assumptions about the data distribution [162]. This method is particularly useful for addressing specific issues when the theoretical understanding of a problem is limited, even if a large number of observations are available [162]. Machine learning tasks usually be categorized as supervised, unsupervised, reinforcement learning, and deep learning [163]. Supervised learning is a type of machine learning algorithm that uses labeled data to learn the relationship between input-output pairs. These algorithms can handle many input variables and a single output variable [164]. Supervised learning is performed for two main tasks: classification, which predicts categorical values, and regression, which predicts continuous values [163]. Conversely, unsupervised learning is a type of machine learning that trains algorithms using unclassified and unlabeled data [163]. Without any guidance, it aims to identify patterns, similarities, and differences in the data [165]. Unsupervised learning is mainly used for clustering, dimensionality reduction, and anomaly detection [163]. Reinforcement learning is a slightly differs from supervised and unsupervised learning. This method focuses on how software agents can optimize their decision-making in an environment by taking actions that maximize cumulative rewards over time. In this learning paradigm, an agent learns by performing actions, observing the consequences, and drawing inferences from the results to maximize a specific

notion of cumulative reward [163,165]. Deep learning models have multiple layers that enable progressive learning, and they include both supervised and unsupervised algorithms [166]. Deep learning utilizes artificial neural networks, inspired by the human brain's structure and function. These networks come in various forms, such as recurrent, convolutional, and feedforward neural networks [163].

Machine learning algorithms enable data-driven decision-making that can be integrated into modeling systems to address gaps and reduce demands on human experts in various research, such as oceanography [167–170], environmental monitoring [171–173], and oil spill research [39,162,166,174–182]. One of the commonly used types of machine learning in oil spill research is supervised learning [180,183–187]. For instance, Liu et al. (2019) employed support vector machine incorporated with texture analysis and adaptive thresholding on X-band marine radar images to bring about semi-automatic oil spill detection method. They indicated that this method enables accurate, consistent, and semi-automatic extraction of oil spills without manual threshold setting by testing on radar images from a 2010 oil spill accident in Dalian, China [183]. Conceição et al. (2021) developed open-source procedures using two random forest classifiers to effectively deal with oil spills. The first classifier uses an ocean synthetic aperture radar image to categorize biofilm and multi-containing oil, while the second, Radar Image Oil Spill Seeker (RIOSS), targets oil spills on maritime surfaces using Sentinel-1 SAR images. The algorithms were highly accurate and improved by 90% with the use of RIOSS [180].

Another commonly used machine learning type is deep learning [174, 181, 182, 188–191]. For example, De Kerf et al. (2020) employed seven convolutional neural network segmentation architectures combined with eight different feature extractors to find the best combination to detect the oil spill in port environment. They indicated that the combination of Mobilenet Feature extractor and fully convolutional network architecture achieve the best performance with the mean Intersection over Union of 89% [174]. Seydi et al. (2021) a new oil spill detection framework based on a multiscale multidimensional residual kernel convolution neural network was developed for optical remote sensing imagery. They indicated this method has high potential for oil spill detection as more than 95% accuracy rate and less than 5% of false alarm rate were achieved when compared with the imagery acquired over the Gulf of Mexico [191].

Researchers also compare the efficiency of using these two types of machine learning algorithms [166,176,192]. For instance, Li et al. (2021) investigated the identification of oil spill types using high-resolution hyperspectral sensors and four machine learning algorithms, including supervised learning of random forest and support vector machine, and deep learning of deep neural network and differential pooling deep neural network. These four models were compared in terms of prediction accuracy and computational complexity. Results suggest that the two deep learning models achieve the most accurate prediction at the cost of more computation, while the support vector machine or proposed differential pooling deep neural network may be more favorable when training time is limited [176]. Mohammadiun et al. (2022) compares various regression-based

machine learning techniques, including artificial neural networks, gaussian process regression, and support vector regression, to develop decision-support models for oil spill response methods selection. Using a small dataset, optimized fuzzy decision trees models and gaussian process regression showed the best prediction power, and the Bayesian regularization algorithm improved artificial neural network performance. These findings can aid in timely and effective oil spill response methods selection in challenging Arctic/subarctic conditions [192].

Machine learning algorithms such as decision trees, artificial neural networks, and support vector machines have shown to be effective in analyzing oil spill trajectory on water surface and classifying spilled oil type with high accuracy and efficiency. This provides valuable insights and predictions to inform response strategies and mitigate environmental impacts. However, the use of machine learning algorithms for predicting oil spill weathering processes and oil transport in water column is still limited and requires further exploration and investigation.

2.8 Summary

Although several efforts have been made to OMA-related research, there still some research gaps to be addressed. First, different studies have employed various laboratory methods and many studies lack replication, introducing considerable uncertainty in the results. Additionally, there is an absence of systematic analysis regarding the important factors and interaction effects using statistical methods. Furthermore, most empirical equations for estimating OMA size distribution and settling velocity rely heavily on collision-theory and Stokes'

Law, which may not fully capture the complexity of the aggregation and settling process. Moreover, the use of machine learning algorithms for predicting oil spill weathering processes, such as OMA formation, and oil spill transport in water column is still limited and requires further exploration and investigation. As for the prediction of oil spill trajectory on water surface, the alternative approaches, such as the FTLE method, are required to predict the oil spill trajectory more accurately and efficiently.

Chapter 3: Materials and Methods

3.1 OMA Formation Experiments

Crude oil from Iran with a density of 799.2 kg/m^3 and viscosity of 61.1 cSt was used. For the mineral component, kaolinite and montmorillonite are widespread in nature and can be found in various environments, such as soils and sediments. Their abundance makes them readily available and cost-effective options for forming OMA [193]. Either kaolinite with a density of 2788.9 kg/m^3 or montmorillonite with a density of 2172.5 kg/m^3 was used, depending on the experimental conditions. Additionally, a chemical dispersant (namely, JAFIRSTTM001) was utilized, maintaining a dispersant-to-oil ratio (DOR) of 1:10, in compliance with the established experimental parameters. Prior research has demonstrated that this specific DOR is conducive to the effective formation of OMA [33].

According to the literature, the formation of OMA could be influenced by the following seven factors: salinity, temperature, time, mixing energy, mixing ratio, clay type, and the presence/absence of dispersant. The experiments were designed using Screening Design in Minitab 19 software, and their levels are provided in Table 3.1. The 0°C was used to simulate the winter water temperatures in most coastal area. The water temperatures of 15°C and 30°C were used to simulate the summer water temperatures in various coastal environments around the world. The 15°C temperature is more representative of temperate coastal regions, such as the coastal areas of Northern Europe, the northeastern coast of the United States, and

the southern coast of Australia [194]. The 30°C temperature is more indicative of tropical and subtropical coastal regions, such as the Caribbean, the Gulf of Mexico, Southeast Asia, and the northern coast of Australia [194]. Furthermore, concerning salinity, 0 ppt was utilized to represent river water, while 17 ppt simulated coastal regions near river mouths, estuaries, or areas with substantial freshwater input. A salinity of 34 ppt was employed to emulate subtropical and tropical coastal regions. The mixing duration of 4 h and 6 h were demonstrated to successfully form OMAs in previous studies [32, 34, 195]. As time is a continuous factor, equal spacing between levels was implemented when designing the experiment using Screening Design; 8 h was selected to investigate the influence of extended time on OMA formation. Agitation speeds of 100, 130, and 160 rpm, which were shown to successfully form OMAs in prior literature [27, 32, 113] were also employed in this study. Oil/clay ratios of 1:2, 1:1, and 2:1 were examined by Sun et al. (2014) and Zhang et al. (2019), indicating that varying oil/clay ratios influenced oil trapping efficiency. Consequently, this study utilized these three distinct oil/clay ratios to determine their impact on OMA formation.

Each experiment was conducted twice to reduce experimental errors, and the detailed experiment runs (18×2 runs) were provided in APPENDIX B Table S3.1. According to the experiment design, the aqueous solution (100 mL) was prepared by adding a certain amount of sea salt, depending on the salinity. 40 mg oil and 20 – 80 mg clay (depending on oil/clay ratio) were then loaded into a 250 mL baffled flask containing the prepared aqueous solution. A temperature-controllable shaker (Figure S3.1) was utilized to agitate the sample-containing flask

and form OMA. The shaking frequency of 100, 130, and 160 rpm (revolutions per minute), which can be approximately transferred to 15, 18, and 20 s⁻¹ of share rate [197], were selected to form OMA. The frequency of sampling was every 60 min. Inverted microscopy (Figure S3.2) was employed to acquire the images to observe OMA structures, and the image processing software (ImageJ.exe) was then used to obtain the OMA size (area and perimeter). All the OMA samples were directly collected from the running experiment in real-time using wide-mouth (> 2mm) plastic pipettes to minimize the microscope slides without using a coverslip to prevent the samples from being squeezed. OMA samples were observed with a 20 – 40 times zoom-in screen, and six images for each sample were captured for further analysis. An example of the acquired image is shown in Figure S3.3.

Table 3.1 The level of factors of interest for oil-mineral-aggregate formation.

Factors	Level		
Temperature (°C)	0	15	30
Salinity (ppt)	0	17	34
Time (h)	4	6	8
Agitation (rpm)	100	130	160
Mixing ratio (oil/sand, w/w)	1:2	1:1	2:1
Clay type	Kaolinite	Montmorillonite	
Presence of dispersant	Yes	No	

3.2 OMA Settling Velocity Measurement

The pre-formed OMA was subjected to an overnight settling period, approximately 16 hours in duration, prior to collection for subsequent settling

experiments. This approach was necessitated by the challenges associated with collecting and identifying floating and neutrally buoyant OMA under magnified observation. The system of settling experiment is illustrated in Figure 3.1. The dimension of the settling column is 10×10×50 cm. The high-speed camera with a magnifying lens (18 times zoom-in), which can track the steady state particles, was positioned at 65 mm above the column base. The hemocytometer was used as the reference scale. About 5 L of the prepared aqueous solution was gently added into the settling column to prevent excessive bubbles on the inner column surface. Then, the settled OMA was collected by a wide mouth (> 2mm) plastic pipette from the baffled flask and transferred to the settling column smoothly. The high-speed camera acquired 40 pictures per second, and each stream lasted for 8 seconds, giving 240 continuous pictures within each stream. 100 – 150 streams were taken for each experiment. The acquired streams were then analyzed using the Revealer High-speed Video Target Tracking Measurement Software VL (RHSVTTMS-VL) to obtain the OMA settling velocity. The diameter of target OMA in streams was correspondingly quantified by using ImageJ.exe. The example of OMA settling velocity and size measurements are shown in Figure S3.4.

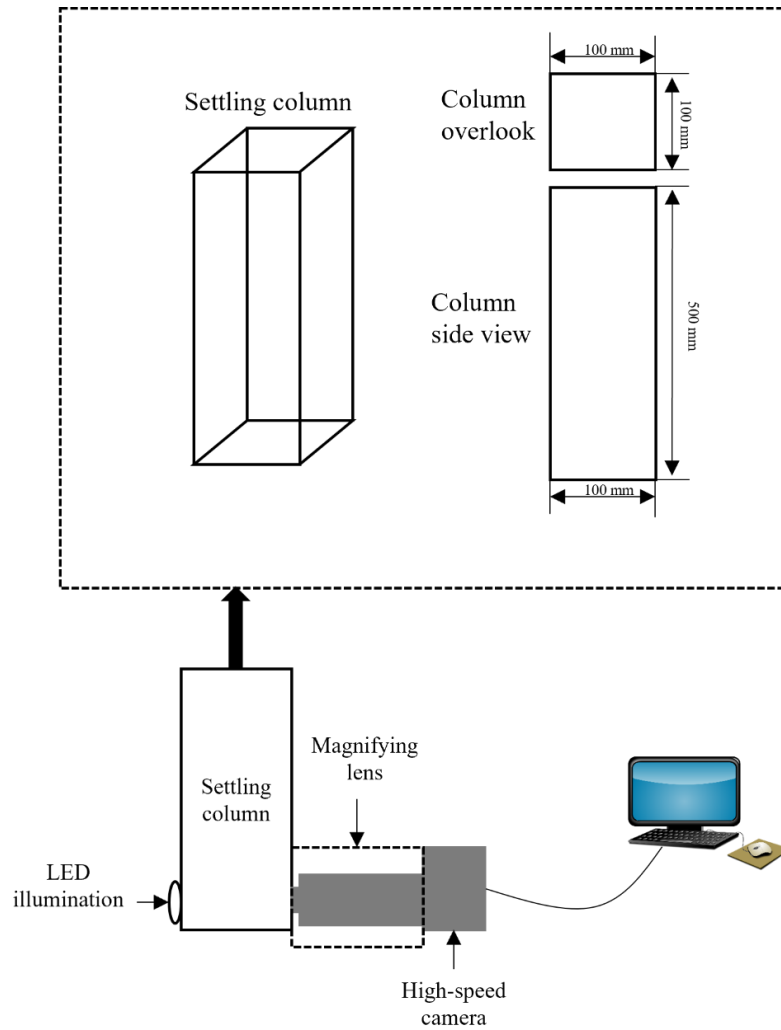


Figure 3.1 The scheme of the settling column experiment system.

3.3 Traditional Empirical Prediction of OMA Settling Velocity

The studies on the traditional empirical prediction of OMA's settling velocity were minimal in the literature. Thus, the prediction on the similar and more thoroughly studied process, settling of fine-grained suspended flocs, can serve as a valuable reference for OMA's settling velocity prediction. For most floc settling velocity formulas, the effective density of particles (OMA in this study) is one of the necessary input parameters. Therefore, seven equations were selected to

calculate the OMA effective density, as shown in Table 3.2. The calculated density then served as an input parameter when employing the flocs settling velocity prediction equations (nine equations), as shown in Table 3.3, to estimate the OMA settling velocity. Therefore, there are 7×9 groups of equations to calculate the OMA settling velocity by incorporating the effective density estimation equation.

Table 3.2 Empirical effective density prediction formulas.

#	Equations	Comments	References
1	$\rho_a - \rho_w = 0.0013D_a^{-0.9}$	D_a is in cm and the densities in g cm^{-3}	[198]
2	$\rho_a - \rho_w = (\rho_s - \rho_w)\left(\frac{D_a}{d}\right)^{-0.9}$		[199]
3	$\rho_a - \rho_w = \begin{cases} 1 & \text{for } D_a \leq 1 \text{ } \mu\text{m} \\ \propto D_a^{-0.42} & \text{for } 1 \leq D_a \leq 50 \text{ } \mu\text{m} \\ \propto D_a^{-1.3} & \text{for } 50 \leq D_a \leq 1200 \text{ } \mu\text{m} \\ 0.003 & \text{for } D_a \geq 1200 \text{ } \mu\text{m} \end{cases}$	D_a is in μm and the densities in g cm^{-3}	[200]
4	$\rho_a - \rho_w = (\rho_s - \rho_w)\left(\frac{D_a}{d}\right)^{F-3}$	$F=1.6, 2, 2.4$	[201]
5	$\rho_a - \rho_w = 7971D_a^{-1.19}$	D_a is in μm	[202]
6	$\rho_a - \rho_w = (\rho_s - \rho_w)\left(\frac{D_a}{d}\right)^{3-D_f}$ $D_f = \begin{cases} -0.0047d + 3.0183 & d \leq 50\mu\text{m} \\ -0.0007d + 2.7529 & d > 50\mu\text{m} \end{cases}$		[203]
7	$\rho_a - \rho_w = b d_f^{D_f-3} d_p^{3-D_f} (\rho_s - \rho_w)$	$b=0.78; d_p=7.5 \text{ } \mu\text{m}; D_f=2.33, 2.61, 2.83$	[204]

Table 3.3 Empirical settling velocity prediction equations.

#	Equations	Comments	References
	w_s		
1	$= \begin{cases} \frac{vD_*^3}{18D} & \text{for } D_* \leq 16.187 \\ \frac{10v}{D} [\sqrt{1 + 0.01D_*} - 1] & \text{for } 16.187 < D_* \leq 16187 \\ \frac{1.1vD_*^{1.5}}{D} & \text{for } D_* > 16187 \end{cases}$		[205]
2	$w_s = \frac{v}{D} (\sqrt{10.36^2 + 1.049D_*^3} - 10.36)$	$D_* = D \left[\frac{\Delta g}{v^2} \right]^{\frac{1}{3}}$	[206]
3	$w_s = \frac{v}{D} (\sqrt{25 + 1.2D_*^2} - 5)^{1.5}$	$\Delta = \frac{\rho_s}{\rho_w} - 1$	[207]
4	$w_s = 0.004d^{0.77}$		[202]
5	$w_s = \frac{v}{d} \left[\sqrt{\frac{1}{4} \left(\frac{A}{B} \right)^{\frac{2}{m}} + \left(\frac{4d_*^3}{3B} \right)^{\frac{1}{m}} - \frac{1}{2} \left(\frac{A}{B} \right)^{\frac{1}{m}}} \right]^m$	a,b,m=24, 0.4, 2; 24, 1.5, 1; 26.4,1.27,1; 32,1,1.5	[208]
6	$w_s = \begin{cases} \frac{0.033v}{D} \left(\frac{\Delta g D^3}{v^2} \right)^{0.963} & \text{for } D_* \leq 10 \\ \frac{0.51v}{D} \left(\frac{\Delta g D^3}{v^2} \right)^{0.535} & \text{for } D_* > 10 \end{cases}$		[209]
7	$w_s = \frac{37.8\Delta D_n + 3780\Delta D_n^2}{0.383 + 10000\Delta v + 100\Delta^2 D_n}$		[210]
8	$w_s = \frac{(\rho_a - \rho_w) * g * D^2}{18 * \rho_w * v * f(Re)}$	$f(Re) = \frac{1}{(1 + 0.1875 * Re)}$	[40]

$$Re = \frac{(\rho_a - \rho_w) * w_s * D^2}{\rho_w * \nu}$$

$$9 \quad w_s = \frac{10\nu}{D} \left[\left(1 + \frac{0.01\Delta g D^3}{\nu^2} \right)^{0.5} - 1 \right] \quad [22]$$

3.4 Machine Learning Prediction

Tree-based machine learning algorithms, Random Forest (RF), Gradient Boost Regression (GBR), and Adaptive Boosting (AdaBoost), were employed to estimate OMA median diameter and OMA settling velocity in the present work. The selection of these algorithms was based on their ability to model non-linear relationships between input features and response variables, as well as their robustness in handling noise and outliers. Comprehensive explanations of these algorithms are provided in Chapter 2, Section 2.7.

Single task models were developed in the Anaconda3 environment based on Python 3.9 using Scikit-learn libraries [211]. The input dataset was randomly partitioned into two subsets, with 80% designated for training and 20% for testing, using the `train_test_split` package from Scikit-learn. A grid-search method, accompanied by 5-fold cross-validation, was employed to optimize two critical hyperparameters: maximal tree depth (`max_depth`) and tree number (`n_estimators`). The `n_estimators` parameter was adjusted in increments of 5, ranging from 5 to 200, while `max_depth` was examined in increments of 1, spanning the range of 5 to 50. Upon determining the optimal hyperparameters, they were integrated into the models, and the dataset was randomly shuffled and divided into five equally sized folds. For each fold, the current fold (representing 20% of the original dataset) was assigned as the testing set, while the remaining four folds (constituting 80% of the original dataset) were designated as the training set. Subsequently, the model was trained using the training set, evaluated with the validation set, and the performance metric was documented. The final model performance was determined by

calculating the average performance metric across all five folds. For a more comprehensive explanation of the optimal hyperparameter search process, refer to Yu et al. (2023).

The coefficient of determination (R^2) and root means square error (RMSE) were employed to assess the models' prediction accuracy. A higher R^2 and lower RMSE indicate higher prediction accuracy. The equations for R^2 and RMSE calculation are provided as follows:

$$R^2 = 1 - \frac{\sum_{n=1}^N (y_n - \widehat{y}_n)^2}{\sum_{n=1}^N (y_n - \bar{y})^2} \quad (3.1)$$

$$\text{RMSE} = \sqrt{\frac{1}{N} \left(\sum_{n=1}^N (y_n - \widehat{y}_n)^2 \right)} \quad (3.2)$$

where N denotes the number of test samples; \widehat{y}_n and y_n is the predicted value and corresponding actual value of the n^{th} sample, respectively; \bar{y} denotes the average of actual values.

The importance of each factor can be quantified by using machine learning algorithms (tree-based algorithm in this study). Specifically, the Gini index was utilized to represent the purity of tree nodes, in which the larger the Gini index, the lower the purity. The variance between the sum of the Gini indexes of split nodes and the Gini index of each tree node was denoted as Gini decrease. The Gini decrease weighted by sum of the same node in all trees was termed Gini importance, ranging from 0 to 1. A larger value indicates the greater importance of the factor.

This method was implemented using the `feature_importance_` package in the Scikit-learn section.

3.5 Particle Tracking Algorithm

The particle trajectories were numerically determined by integrating the following equation [50]:

$$\begin{cases} \frac{dx_i}{dt} = u(x_i, y_i, t) \\ \frac{dy_i}{dt} = v(x_i, y_i, t) \end{cases} \quad (3.3)$$

where the i subscript indicates the i th particle and denotes the position of the particle. (u, v) represents the instantaneous velocity at the location of the particle (x_i, y_i) , and is interpolated from the FVCOM current data. Particles that adhered to the shore/bottom were permanently removed, but their last active positions in the water were recorded. Overall, the results of particle trajectories and instantaneous velocities were recorded every hour.

To identify the influence of OMA settling velocity on the deposition of OMA in the marine environment, the empirical prediction equation with the highest R^2 and machine learning algorithm was incorporated into the particle tracking model in parallel. Furthermore, the velocities due to turbulence were included in this study to consider the effects of the environment. Equation 3.3 can be therefore converted to follows:

$$\begin{cases} \frac{d_{x_i}}{d_t} = u(x_i, y_i, z_i, t) + u_t \\ \frac{d_{y_i}}{d_t} = v(x_i, y_i, z_i, t) + v_t \\ \frac{d_{z_i}}{d_t} = w(x_i, y_i, z_i, t) + w_t \end{cases} \quad (3.4)$$

where w denotes the vertical velocity obtained from the empirical prediction equation or machine learning prediction results. The terms u_t , v_t , and w_t represent the velocities resulting from turbulence and can be described as follows:

$$\begin{aligned} u_t &= R \frac{\sqrt{2K_H \Delta t}}{\Delta t} \\ v_t &= R \frac{\sqrt{2K_H \Delta t}}{\Delta t} \\ w_t &= R \frac{\sqrt{2K_v \Delta t}}{\Delta t} \end{aligned} \quad (3.5)$$

where R is a normal random number with zero mean and a variance of 1, K_H and K_v are the horizontal and vertical mixing coefficients in the unit of $\text{m}^2 \text{s}^{-1}$ [213].

Chapter 4: OMA Formation

4.1 Experimental Design and Acquired Data

The OMA formation experimental design and data acquisition was described in Chapter 3, Section 3.1. The raw data for each experiment were presented in Table 4.1. The raw data of OMA median diameter in the two replicated experiments appears to differ. This discrepancy could potentially stem from the relatively small sample size (one sample at each time step) and the acquisition of a limited number of images (six images) per sample, leading to a decreased number of detected OMAs. Nonetheless, a paired t-test conducted in Minitab yielded a p-value of 0.329, which is greater than the 0.05 significance level. This result suggests that there is no statistically significant difference between the means of OMA median diameter of the two experiments. Consequently, measurement inaccuracies and human errors were not identified as contributing factors in this study.

4.2 Statistical Analysis

4.2.1 Significance of Studied Factors

Many factors have been reported to affect the median diameter (D_{50}) during the OMA formation process. However, the level/significance of their influences has not been systematically investigated and compared. We, therefore, covered a wide range of factors (temperature, time, salinity, clay type, agitation speed, oil/clay weight ratio, and the absence/presence of dispersant) and employed a statistical method (Screening Design and Analysis of Variance (ANOVA)) to find out the

most influential factors for OMA median diameter (D_{50}). The ANOVA results, including significant model terms, were provided in Table 4.2 and Equation 4.1. It can be clearly observed that time exhibited the most significant impact on D_{50} , as evidenced by its highest F-value (22.48) and lowest p-value ($0.000 < 0.05$), followed by temperature (p-value of 0.014) and oil/clay ratio (p-value of 0.023). Clay type was only a marginally significant factor for D_{50} ($0.05 < \text{p-value} = 0.069 < 0.1$).

Table 4.1 The experiment setting based on Screening Design.

Standard order	Temperature (°C)	Salinity (ppt)	Agitation time (h)	Clay type	Agitation speed (rpm)	Oil/clay ratio	Dispersant	Median diameter (µm)
1	15	34	8	Montmorillonite	160	2: 1	Yes	14.59
2	15	0	4	Kaolinite	100	1: 2	No	21.15
3	30	17	8	Kaolinite	160	1: 2	No	29.19
4	0	17	4	Montmorillonite	100	2: 1	Yes	33.13
5	30	0	6	Kaolinite	160	2: 1	Yes	16.89
6	0	34	6	Montmorillonite	100	1: 2	No	42.65
7	30	34	8	Kaolinite	100	2: 1	No	15.52
8	0	0	4	Montmorillonite	160	1: 2	Yes	25.19
9	30	0	4	Montmorillonite	130	2: 1	No	28.13
10	0	34	8	Kaolinite	130	1: 2	Yes	72.03
11	30	34	4	Kaolinite	100	1: 1	Yes	13.58
12	0	0	8	Montmorillonite	160	1: 1	No	72.82
13	30	34	4	Montmorillonite	160	1: 2	No	18.77
14	0	0	8	Kaolinite	100	2: 1	Yes	19.13
15	30	0	8	Montmorillonite	100	1: 2	Yes	31.44
16	0	34	4	Kaolinite	160	2: 1	No	11.40
17	15	17	6	Kaolinite	130	1: 1	No	15.20
18	15	17	6	Montmorillonite	130	1: 1	Yes	86.27
1	15	34	8	Montmorillonite	160	2: 1	Yes	37.16
2	15	0	4	Kaolinite	100	1: 2	No	13.24
3	30	17	8	Kaolinite	160	1: 2	No	33.02
4	0	17	4	Montmorillonite	100	2: 1	Yes	18.58

Standard order	Temperature (°C)	Salinity (ppt)	Agitation time (h)	Clay type	Agitation speed (rpm)	Oil/clay ratio	Dispersant	Median diameter (µm)
5	30	0	6	Kaolinite	160	2: 1	Yes	24.40
6	0	34	6	Montmorillonite	100	1: 2	No	28.30
7	30	34	8	Kaolinite	100	2: 1	No	36.59
8	0	0	4	Montmorillonite	160	1: 2	Yes	17.65
9	30	0	4	Montmorillonite	130	2: 1	No	18.93
10	0	34	8	Kaolinite	130	1: 2	Yes	65.93
11	30	34	4	Kaolinite	100	1: 1	Yes	9.99
12	0	0	8	Montmorillonite	160	1: 1	No	53.62
13	30	34	4	Montmorillonite	160	1: 2	No	28.78
14	0	0	8	Kaolinite	100	2: 1	Yes	16.67
15	30	0	8	Montmorillonite	100	1: 2	Yes	28.07
16	0	34	4	Kaolinite	160	2: 1	No	16.82
17	15	17	6	Kaolinite	130	1: 1	No	12.93
18	15	17	6	Montmorillonite	130	1: 1	Yes	39.94

Table 4.2 Analysis of variance for oil-mineral aggregate's median diameter (D_{50}).

	F-value	p-value
Time	22.48	0.000
Temperature	6.96	0.014
Oil/clay ratio	5.77	0.023
Clay type	3.58	0.069
Time*Oil/clay ratio	9.64	0.004
Time*Temperature	6.17	0.020
Temperature*Oil/clay ratio	4.62	0.041

In addition to the p-values of these factors, a linear regression model that capture the relationship between significant factors, including interaction effects, and response variable (OMA D_{50}) was presented in Equation 4.1. The coefficients of the model were estimated using the least squares method. Equation 4.1 is shown as following:

$$D_{50} = -32.9 + 0.109x_1 + 14.21x_2 + 3.42x_3 + 0.435x_4 - 0.1807x_1x_2 + 0.01251x_1x_4 - 0.1356x_2x_4 \quad (4.1)$$

where x_1 , x_2 , x_3 , and x_4 represent temperature ($^{\circ}\text{C}$), time (h), clay type (kaolinite denotes -1 and montmorillonite denotes +1), and oil/clay ratio (1:2 denotes 25, 1:1 denotes 50, 2:1 denotes 75), respectively.

The impact of the identified factors (herein, time, temperature, oil/clay ratio, and clay type) on D_{50} was quantified using Equation 4.1. For each combination of factor levels, the response value (D_{50}) was computed, and the mean value was employed. The resulting plot is illustrated in Figure 4.1. As shown in Figure 4.1a, increasing time from 4 h to 8 h gradually promoted D_{50} from 19 μm to 38 μm ,

suggesting prolonged time enhanced the formation of relatively large OMA. This was in well agreement with the previously reported results [113,214]. Sun et al. (2014) conducted a series of experiments to investigate the effects of time on OMA formation and found that the size of OMA increased with prolonged time, and they stated that the small oil droplets could incorporate into OMA or coalesce on the OMA surface with the increasing time [113]. However, an opposite result was observed by Ji et al. (2021) in that the OMA D_{50} decreased from $\sim 45 \mu\text{m}$ to $\sim 20 \mu\text{m}$ when the mixing duration increased from 30 min to 24 h. They claimed that the decline of OMA D_{50} with increasing time was likely because the particles continuously fragmented the OMA into smaller ones [111]. More efforts are therefore highly recommended to further investigate the influence of mixing time on OMA formation.

Regarding the temperature effect (Figure 4.1b), raising the temperature from $0 \text{ }^\circ\text{C}$ to $30 \text{ }^\circ\text{C}$ steadily decreased the OMA D_{50} , implying that the formation of larger OMA was favored under a low temperature environment. In addition, oil viscosity was reduced with the higher temperature, resulting in more dispersed oil droplet in the water column to interaction with minerals. The OMA D_{50} was therefore decreased when the temperature was raised.

Increasing the oil/clay ratio from 1:2 to 2:1 also reduced OMA D_{50} , as demonstrated in Figure 4.1c. When the oil/clay ratio increased, OMA size dropped because fewer minerals were available to coalesce on the oil droplet surface. However, the present result differed from the observation of previously studies [33,215,216]. They found that OMA size was positively related to the oil/clay ratio.

They stated that the mineral could provide sufficient penetration to fragment the OMA into smaller droplets at the high mineral concentration (low oil/clay ratio).

In Figure 4.1d, it is observed that when montmorillonite participates in OMA formation, the resulting OMA D_{50} (32 μm) is larger compared to that of kaolinite (26 μm). This suggests that montmorillonite possesses a higher hydrophobicity, enabling better interaction with oil, and consequently, resulting in a larger OMA D_{50} . Previous studies have reported similar findings, where the OMA size increased from a few micrometers to tens of micrometers as mineral hydrophobicity increased [108, 109, 215]. Considering mineral surface properties and cation exchange capacity (CEC), montmorillonite exhibits a higher surface charge compared to kaolinite, which facilitates the adsorption of oil droplets and OMA formation [217]. Moreover, montmorillonite has a high CEC, which enables it to adsorb a large amount of organic compounds, including petroleum hydrocarbons. This property contributes to the effectiveness of montmorillonite in OMA formation [217]. Furthermore, montmorillonite exhibits a greater propensity for swelling in aqueous environments compared to kaolinite, which can further promote the penetration of non-polar hydrocarbon molecules into the interlayer spaces of the clay mineral. This swelling property enhances the clay's capacity to adsorb oil and form larger OMA [217].

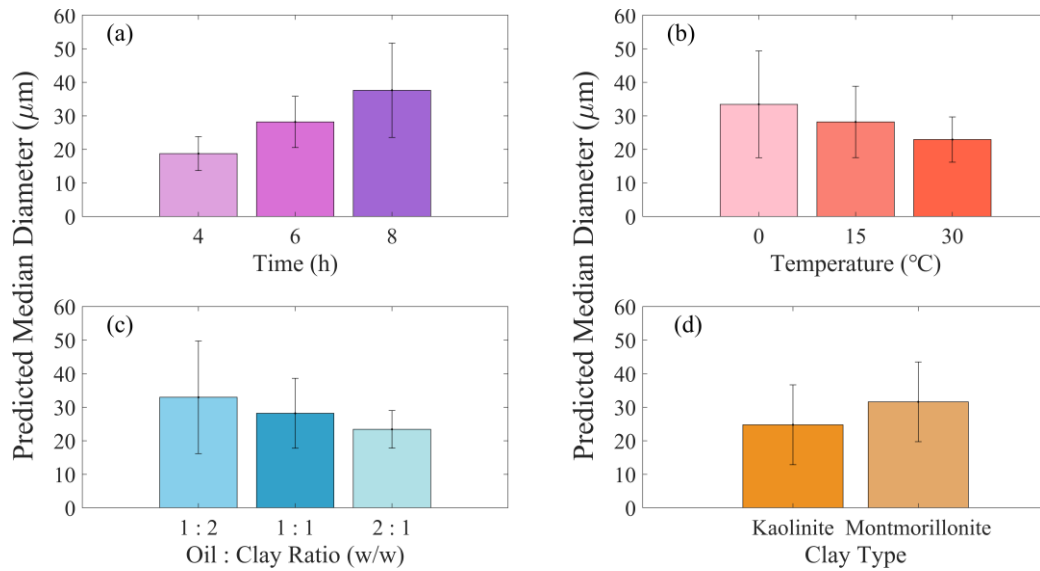


Figure 4.1 The influence of significant factors (a) time, (b) temperature, (c) oil/clay ratio and (d) clay type on oil-mineral aggregate’s median diameter.

4.2.2 Interaction Effects

In addition to the individual influence, the two-factor interaction effects were evaluated, and the significant interaction effects were presented in Table 4.2. The influence of significant interaction effects on D_{50} was calculated/quantified by the linear regression model in Equation 4.1. For each combination of factor levels, the response value (D_{50}) was computed, and the mean value was employed. The resulting plot is illustrated in Figure 4.2. Although the relationship between factors is non-linear, straight lines were obtained as shown in Figure 4.2. The reason is probably that the non-linear component (e.g., interaction term) in the regression model is not significant or exerts minimal influence on the response variable. In such cases, the relationship between the factor and the response can be adequately approximated by a linear model within the investigated range. It is crucial to note, however, that this observation does not necessarily imply a strictly linear relationship between the factor and the response in all scenarios. It merely suggests

that, based on the data and the levels selected for the factor in the experimental design, the relationship appears linear. The true nature of the relationship may yet be non-linear beyond the investigated range or with additional data points.

Notably, the time impact on D_{50} was highly dependent on the oil/clay ratio employed, as evidenced by the low p-value of 0.004 for time*oil/clay ratio interaction in Table 4.2, detail illustrated in Figure 4.2a. When an oil/clay ratio of 2:1 was employed, increasing formation time from 4 h to 8 h did not largely improve D_{50} ($\sim 24 \mu\text{m}$). However, when the oil/clay ratio was switched to 1:1 or 1:2, much greater increments were observed (from $\sim 20 \mu\text{m}$ to as high as $48 \mu\text{m}$). These demonstrated that the effect of time on D_{50} was highly dependent on the oil/clay ratio employed. More specifically, when more clay was presented in OMA formation environments, prolonging time can result in a larger OMA D_{50} .

The influence of time was also highly dependent on the temperature, as illustrated in Figure 4.2b and supported by the p-value (0.02) in Table 4.2. When the temperature was $0 \text{ }^\circ\text{C}$, increasing time from 4 h to 8 h remarkably raised D_{50} from $20 \mu\text{m}$ to $47 \mu\text{m}$, but a less profound increment in D_{50} was observed at $15 \text{ }^\circ\text{C}$ and $30 \text{ }^\circ\text{C}$. These results indicated that a longer time at low temperatures favored the formation of OMA with larger D_{50} , and the formation time became less influential if the temperature was increased.

Referring to Figure 4.2a and Figure 4.2b, it can be observed that at a relatively short mixing time (4 h), variations in the oil/clay ratio or temperature appear to have negligible influence on the median size of OMA. This phenomenon may be attributed to the insufficient time for OMA to fully develop during the initial

mixing period. As a result, the effects of temperature and oil/clay ratio on OMA formation are not yet discernible at this stage. With an increase in mixing time, the gradual growth in OMA median size can be primarily ascribed to the continuous adhesion of free particles onto oil droplets or formed OMA.

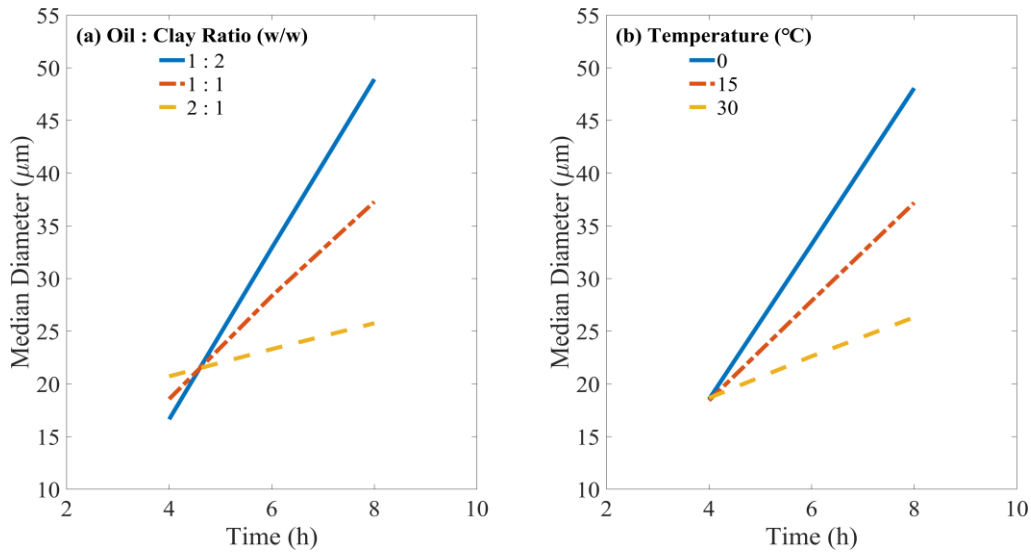


Figure 4.2 Illustrates how time interacts with (a) the oil/clay ratio and (b) temperature influence on the median diameter of oil-mineral-aggregate.

In addition to the mentioned significant factors and interaction effects above, various other factors, including salinity, mixing energy, and dispersant addition, have been shown to influence the formation of OMA in the OMA-related research works [7, 28, 29, 31, 32, 41, 108, 110, 113–116, 215]. For example, Khelifa et al. (2005) examined the impact of salinity, clay type, and oil type on OMA formation, demonstrating that salinity affects the median size of OMA at low concentrations, with a more pronounced influence than either clay type or oil type. Furthermore, their study revealed interaction effects between salinity and clay type on OMA median size. Contrarily, Payne (1989) and Guyomarch et al. (1999) reported that

high salinity values also affect OMA formation. Sun et al. (2010, 2014) posited that mixing energy influences OMA formation by parameterizing oil trapping efficiency. Additionally, Ji et al. (2021) proposed that interaction effects exist between mixing energy and mixing time, impacting the median diameter and oil trapping efficiency of OMA. Several researchers have also discovered that chemical dispersants either reduced [114] or increase [115] the size of OMA. However, these previous findings were not supported by statistical analysis. The disparity in the importance of factors between the current study and the existing literature could likely be attributed to two primary reasons. Firstly, although the impacts of salinity, mixing energy, and dispersant addition on OMA formation have been acknowledged in previous studies, these effects appear to be less significant in comparison to other factors, such as mixing time, temperature, oil/clay ratio, and clay type, given that the present study encompasses a broader type of factors. Secondly, the variation in the importance of these factors might also be attributed to differences in response variables and the distinct ranges or levels of each factor investigated across various studies.

4.3 Machine Learning Prediction

4.3.1 Algorithm Selection

Whether it is feasible to use machine learning algorithms to predict OMA D_{50} has not been explored yet. We herein, for the first time, attempted to estimate OMA D_{50} through machine learning approaches. Three machine learning algorithms were evaluated, including RF, GBR and Adaboost, as mentioned in Chapter 3 Section 3.4. The dataset containing both current work data and literature data [27, 29, 34,

113, 218, 219] and the D_{50} size distribution was illustrated in Figure 4.3. It can be seen that most of the OMA D_{50} were between 3 – 35 μm , and the OMA D_{50} in the range of 35 – 40 μm and 55 – 80 μm was limited. The dataset was used to train the machine learning algorithms by feeding randomly selected 80% of the dataset. The trained algorithms were then tested by assessing their performances in estimating the rest 20% of the dataset.

The training and testing performances of the studied algorithms are presented in Figure 4.4. High training R^2 values (>0.9) and testing R^2 values (>0.7) were obtained from machine learning predictions, with minor differences in R^2 and RMSE among the three tested algorithms. One potential reason for this minor difference is their shared ensemble learning approach. All three algorithms employ ensemble methods, combining the predictions of multiple base models, usually decision trees, to improve overall model performance. Since they share a common foundation, their performance might be similar in certain situations. Another reason for the minor differences in performance could be the relatively small dataset size used in this study, which comprises only 197 samples. Consequently, it is recommended that further research and data collection efforts be undertaken to expand the dataset, which may help in identifying the most suitable algorithms for OMA median diameter prediction.

Despite the minor differences in R^2 and RMSE among the three tested algorithms, AdaBoost (Figure 4.4c) exhibited the best performance in predicting D_{50} , with the highest R^2 value (0.97) and a lowest RMSE value (3.48) compared to those of RF (Figure 4.4a) and GBR (Figure 4.4b). A similar trend can be observed

for testing R^2 and RMSE values, suggesting that the AdaBoost algorithm (testing R^2 of 0.74 and RMSE of 10.02) also outperforms RF and GBR during the testing process. These results indicate that: (1) machine learning algorithms can be feasibly applied for OMA D_{50} prediction, and (2) the predictive performance of AdaBoost is better than that of RF and GBR in this study. It is also important to note that acquiring more data, particularly for OMA D_{50} values in the ranges of 35-40 μm and 55-80 μm , is necessary to expand the dataset and better train the model for more accurate predictions.

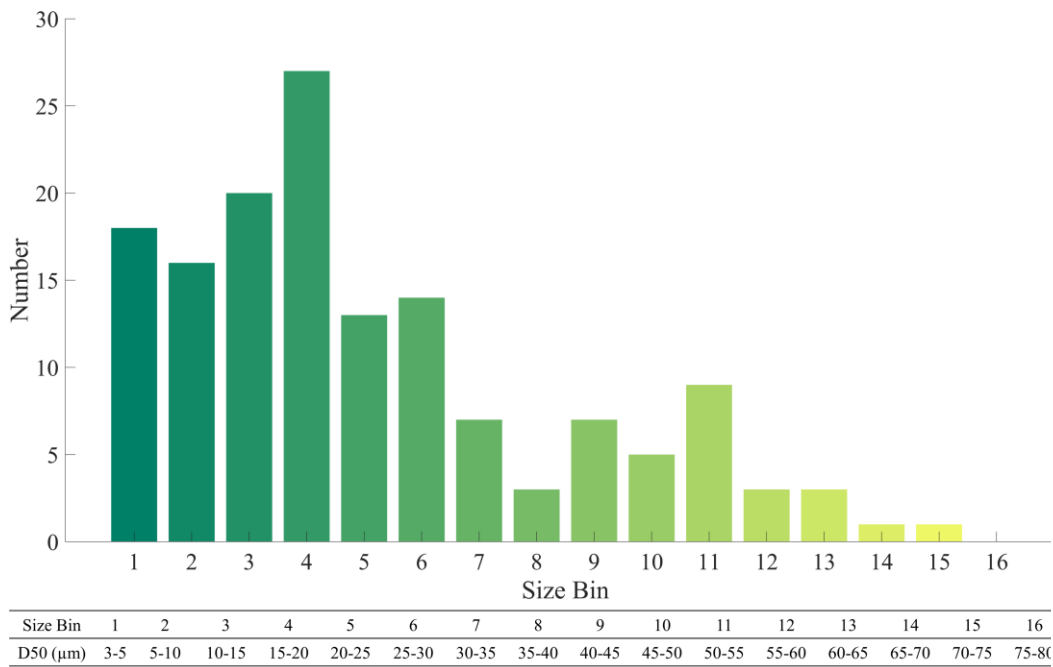


Figure 4.3 The size distribution of the dataset from current and literature data [27, 29, 34, 113, 218, 219].

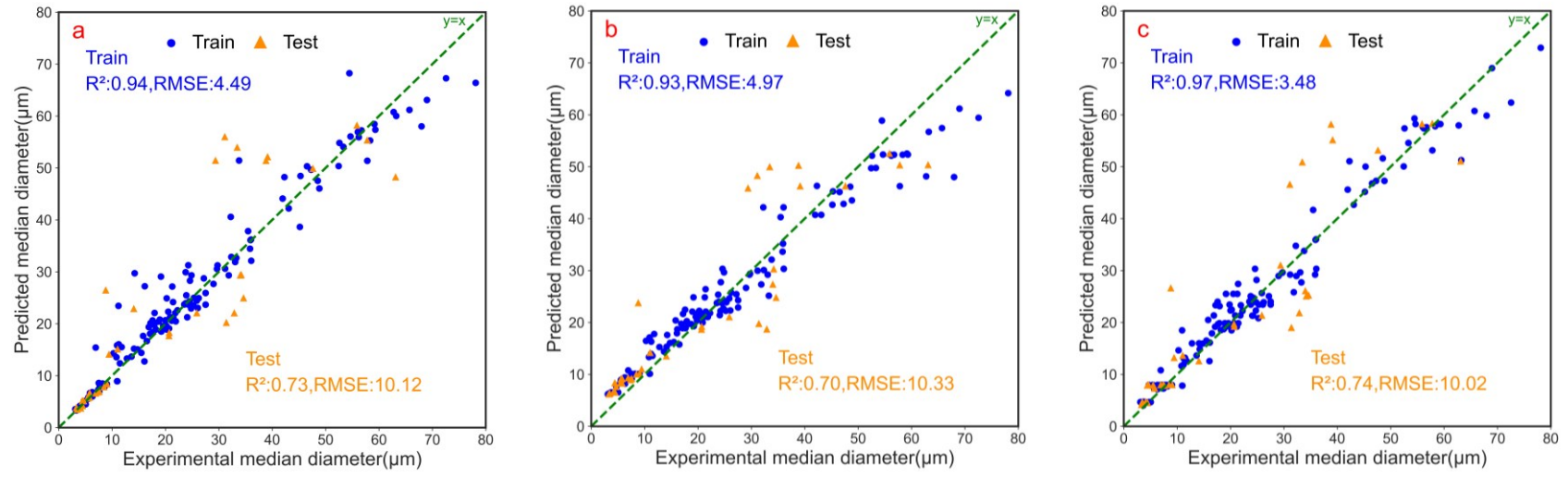


Figure 4.4 Prediction plots (training and testing) for oil-mineral-aggregate's median diameter by using machine learning algorithms (a) Random Forest, (b) Gradient Boosting Regression, (c) Ababoost. RMSE denotes root mean square error.

4.3.2 Factor Importance Quantification by Machine Learning Algorithm

Based upon current work and literature, a variety of OMA formation factors were used to estimate OMA D_{50} , including temperature, time, salinity, shaking rate, clay concentration, oil concentration, clay type (density), oil type (density), and the absence/presence of dispersant. Since Adaboost was recognized as the adequate machine learning algorithm for OMA D_{50} prediction in this study, it was utilized to quantify the importance of each factor, as illustrated in Figure 4.5. Clay concentration, time, clay type (density) and temperature were suggested as the four most important factors for D_{50} , which took greater than 85% of accountability. This was actually in well agreement with the results observed in Section 4.2.1, that time, temperature, oil/clay ratio (closely related to clay concentration), and clay type were all significantly important for D_{50} . Thus, future research on OMA formation could emphasize these four factors.

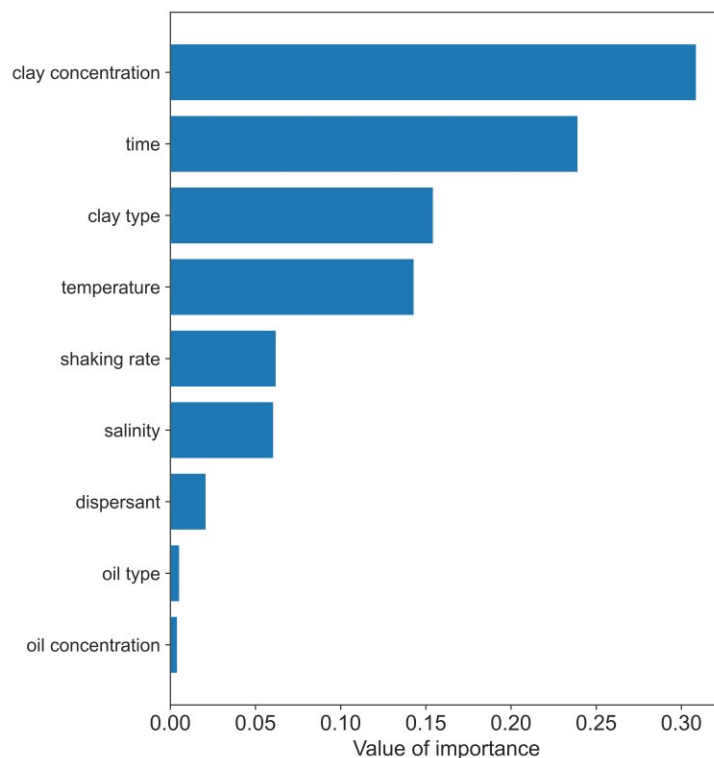


Figure 4.5 The factor importance plot derived from the Adaboost algorithm for oil-mineral-aggregate's median diameter.

4.4 Comparison with Collision-Theory-Based Prediction

Many efforts have been devoted to investigating how the external environment influenced the OMA formation, as discussed in Section 4.2. Also, some attempts have been made to predict OMA formation using collision-theory-based numerical models. Zhao et al. (2016) advanced the coagulation numerical model by developing the A-DROP model. With the aim to generally compare the prediction accuracy between the machine learning algorithm (herein Adaboost) and collision-theory-based numerical model, the A-DROP model was adapted to predict the OMA D_{50} with the input data that has been used to train/test the Adaboost algorithm. Several assumptions were made to run the coagulation model based on the OMA

formation theory as described by Zhao et al. (2016). First, only the interaction between oil-clay and OMA-clay was considered; second, the droplet break-up process was neglected; third, the clay diameter of 5 μm was used, and the oil droplet diameter was much larger than the clay diameter [122].

The prediction accuracy of the A-DROP model was illustrated in Figure 4.6. An R^2 of 0.62 and RMSE of 12.12 were obtained from A-DROP model prediction, which was less satisfactory than that of the Adaboost algorithm (testing R^2 of 0.74 and RMSE of 10.02). These comparative results further highlight the promising potential of employing machine learning algorithms to predict OMA formation.

Furthermore, in comparison to machine learning algorithms, traditional numerical modeling necessitates the modification of input parameters and setup when the oil, mineral, or ambient environment changes for OMA formation. Additionally, the setup of mineral or oil size bins heavily relies on the user's experience. Traditional empirical prediction also demands an understanding of the relationship between physical factors and input parameters. For instance, if salinity or temperature changes, the water viscosity value in the A-DROP model should be adjusted accordingly. Moreover, not all experiments identify the required parameters for traditional OMA size prediction models, occasionally resorting to estimated values, which contributes to the low prediction accuracy of traditional methods. However, one of the limitations of using machine learning algorithms for making predictions is that they can often overlook the underlying theory or relationships between features and predictions. This can result in models that are highly accurate but may lack interpretability and transparency in their decision-

making process. Additionally, machine learning predictions typically require a larger dataset for model training and increased computational resources, and users should carefully and appropriately regularize machine learning algorithms to mitigate the risk of overfitting. In summary, although machine learning algorithms exhibit certain limitations, they are more effective and efficient for predicting OMA formation when contrasted with traditional collision-theory-based predictions.

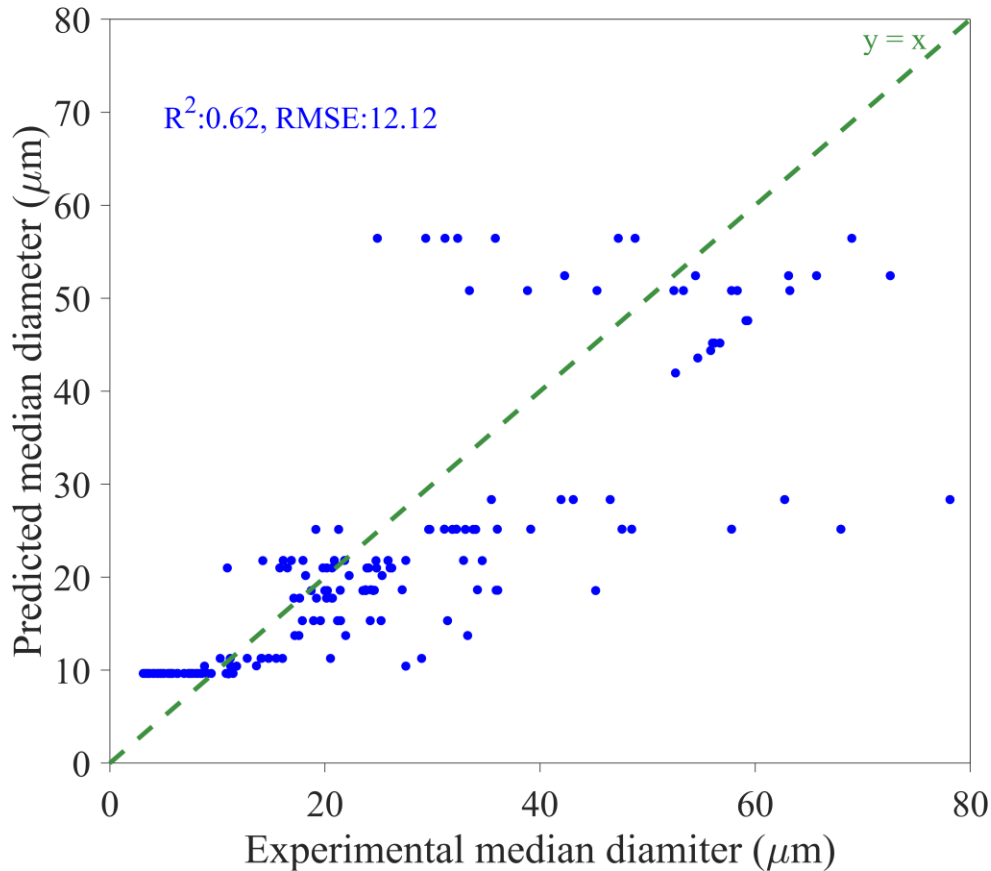


Figure 4.6 The prediction accuracy of the collision-theory-based numerical model developed by Zhao et al. (2016).

4.5 Machine Learning Based Prediction Tool

OMA D_{50} was proved to be adequately predicted by the Adaboost algorithm in Section 4.3.1, which also exhibited better prediction performance than the collision-theory-based numerical model as presented in Section 4.4.1. We, therefore, attempted to develop a machine learning based prediction software that incorporated the Adaboost algorithm. The software screenshot was presented in Figure 4.7, and OMA D_{50} can be quickly estimated by inputting the formation process variables. Notably, more research efforts are required to expand the dataset of OMA D_{50} and even size distributions, which will train the Adaboost algorithm

to become better and thus further improve the prediction accuracy. This open-sourced prediction software can be easily installed on the user's computer by following instructions.

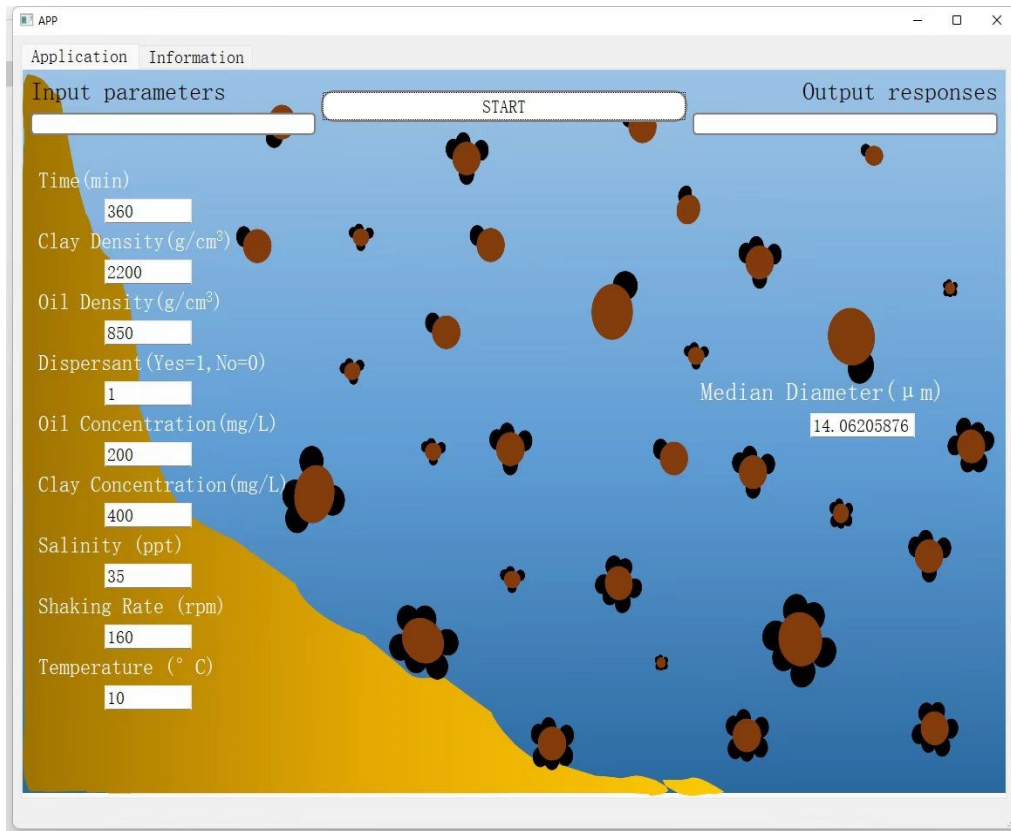


Figure 4.7 The screenshot of machine learning based prediction software for oil-mineral-aggregate's median diameter prediction.

4.6 Summary

With the aim to systematically explore OMA formation and find out the most influential factors, Screening Design was employed to investigate seven process variables' impact, including temperature, time, salinity, clay type, agitation speed, oil/clay weight ratio, and the absence/presence of dispersant. It was found that time exhibited the most profound influence on OMA D_{50} , followed by temperature and

oil/clay ratio. Also, the influence of time heavily depended on the temperature and oil/clay ratio employed. Prolonging formation time to 8 h at a low temperature of 0 °C and 1:2 oil/clay ratio led to a greater OMA D₅₀ (~50 μm).

This study, for the first time, evaluated the feasibility of using machine learning algorithms for OMA D₅₀ prediction. Three tree-based machine learning algorithms (RF, GBR and Adaboost) were assessed. Adaboost had the most satisfactory performance on predicting D₅₀, as evidenced by the high R² (0.97 for training and 0.74 for testing) and low RMSE values. In addition to D₅₀ prediction, Adaboost was implemented to quantify the importance of each process variable, and the obtained results were in well agreement with that of statistical analysis from Screening Design. The machine learning based prediction was then compared with the traditional collision-theory-based prediction by using the same dataset, which the former was favourable in terms of the prediction accuracy (R² of 0.74 vs. 0.62).

Last but not least, an open-sourced machine learning based prediction software that incorporated with Adaboost algorithm and can be easily installed in the user's computer was assembled to quickly predict the OMA D₅₀ by simply keying the formation process variables, even though more research efforts are still required to expand the dataset to train the model better for more accurate prediction. Overall, this multi-disciplinary study not only identified the most influential factors and their interactions during OMA formation, but also innovatively employed machine learning algorithms to predict OMA D₅₀. The results obtained and practical tools developed showed promising potential for future more detailed

OMA studies (e.g., size distribution) and, ultimately, achieve more accurate and smarter tracking of the fate and trajectory of spilled oil.

4.7 Transition Section

The influential factors for OMA formation and their interaction effects were statistically identified in Chapter 4. D_{50} of OMA was adequately predicted by using machine learning algorithms for the first time, proving to be superior to traditional collision-theory-based estimations. However, minimal efforts have been contributed to studying OMA's settling. Chapter 5 thus aims to track the settling of OMA and precisely measure their velocities, then explore environmental variables' influence on OMA settling velocity. Inspired by the excellent performance of machine learning algorithms on D_{50} prediction, the feasibility of using machine learning algorithms for OMA settling velocity estimation was evaluated in Chapter 5 as well.

Chapter 5: OMA Settling Velocity and Empirical Equations

5.1 Experimental Design and Data Acquire

The details of the OMA settling velocity experimental setting and data acquisition were illustrated in Chapter 3, Section 3.2.

5.2 Laboratory Tests

5.2.1 Data Adequacy and Characteristics

The OMA number distribution and averaged settling velocities were provided in Figure 5.1. It can be seen from Figure 5.1a that most OMA (with a number of ~2000) had a diameter ranging from 30 – 60 μm , followed by the diameter of 60 – 90 μm (~600). This was consistent with the results from [40] that most OMA had a diameter between 40 μm and 80 μm when kaolinite was used for OMA formation. As for the averaged settling velocity of each size bin, they varied from 0.2 mm/s to 3 mm/s, with the majority being between 0.2 to 1 mm/s. It is notable that along with the increment of OMA diameter, the averaged settling velocity gradually increased as well (Figure 5.1b), indicating the significant formation of flake/solid-like OMA that contained high percent of minerals instead of oil in the large OMA.

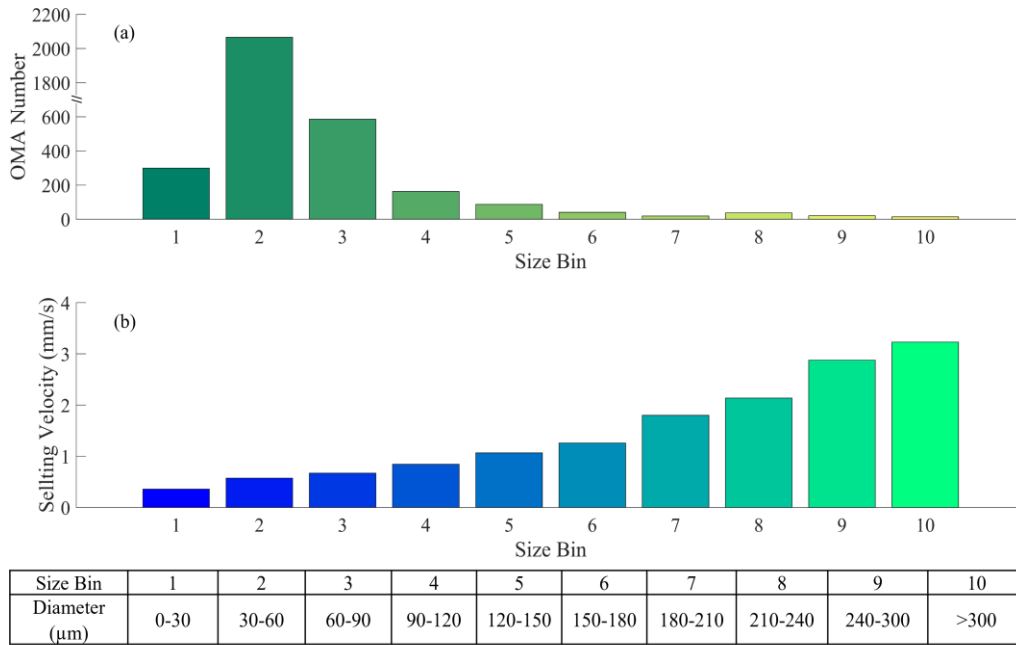


Figure 5.1 The characteristics of oil-mineral-aggregate (OMA) based on size bins (a) OMA number distribution, (b) averaged settling velocity.

5.2.2 Correlation Between Studied Factors and Settling Velocity

Besides understanding the general characteristics of OMA settling velocity data, how the process variables affect the settling velocity was also investigated. The variables studied were water density (kg/m^3), clay density (kg/m^3), clay concentration (mg/L) and dispersant addition. Principle Component Analysis (PCA) is known to have the capability of handling a large dataset to explore the correlation between studied factors and response. Thus, PCA was adapted to correlate process variables of interest with OMA settling velocity, as shown in Figure 5.2.

It can be clearly observed that settling velocity was in close relation and the same direction with clay concentration (both at the right-low corner), suggesting that a higher clay concentration could lead to faster settling velocity, presumably because the formation of mineral-rich OMA was favored at a high clay

concentration. This was in well agreement with the results from O'Laughlin et al. (2017) that OMA settling velocity increases under a relatively high concentration of clay (comparing 10 mg/L with 50 mg/L). However, the water density (proportional to salinity) was separated from settling velocity by both the first and second component, locating at the left-high corner and was thus opposed to settling velocity (Figure 5.2), indicating the rising water density (high salinity water environment) reduced the OMA settling velocity. Although the exploration of the salinity effect on OMA settling velocity is limited, several previous works reported that salinity was an essential factor that impacts the floc settling velocity. Some researchers stated that the floc settling velocity increased with the rising floc concentration and salinity [220, 221]. By comparison, other studies illustrated that the floc settling velocity could reach its maximum values at a specific concentration and salinity. The further increased concentration and salinity would decrease the floc settling velocity [222–225]. However, the specific value of concentration and salinity is still unknown.

Clay density stayed with settling velocity on the right side, even though it was separated from settling velocity by the second component, implying its positive but mild correlation with settling velocity. The settling of OMA is closely related to gravity. The higher density of OMA, therefore, led to a greater settling velocity. However, the density of OMA not only depends on the clay density, but also relates to oil density and the amount of trapping oil. Clay density was, therefore, mildly correlated with OMA settling velocity.

Regarding the addition of dispersants, it has been observed that although both dispersant addition and settling velocity were present in the bottom layer (Figure 5.2), they were separated by the first component, indicating a mildly negative correlation. This phenomenon could be attributed to the dispersant's ability to produce smaller oil droplets, which subsequently mix more readily with water and sediment in the water column, thereby increasing the formation of smaller OMA and resulting in a relatively lower settling velocity. This hypothesis aligns with the findings of Lee et al. (2008) who reported that chemical dispersants could reduce OMA size, ultimately decreasing their settling velocity. Contrastingly, some researchers have posited that the addition of chemical dispersants could lead to larger OMAs due to an enhancement in oil's adhesive properties [115] or a delay in the flocculation of natural sediments, thereby increasing the availability of sediment to interact with oil droplets [41]. Under these circumstances, larger OMAs with a higher mineral composition would form, consequently increasing the settling velocity. Nonetheless, as depicted in Figure 5.1, the present study primarily observed smaller OMA. Hence, based on the experimental conditions established in this investigation, it can be inferred that the introduction of chemical dispersants is likely to yield smaller OMA, subsequently leading to reduced settling velocities.

Overall, we generally concluded that settling velocity was positively correlated with clay concentration, followed by clay density. Conversely, it was negatively correlated with water density and dispersant addition in this study.

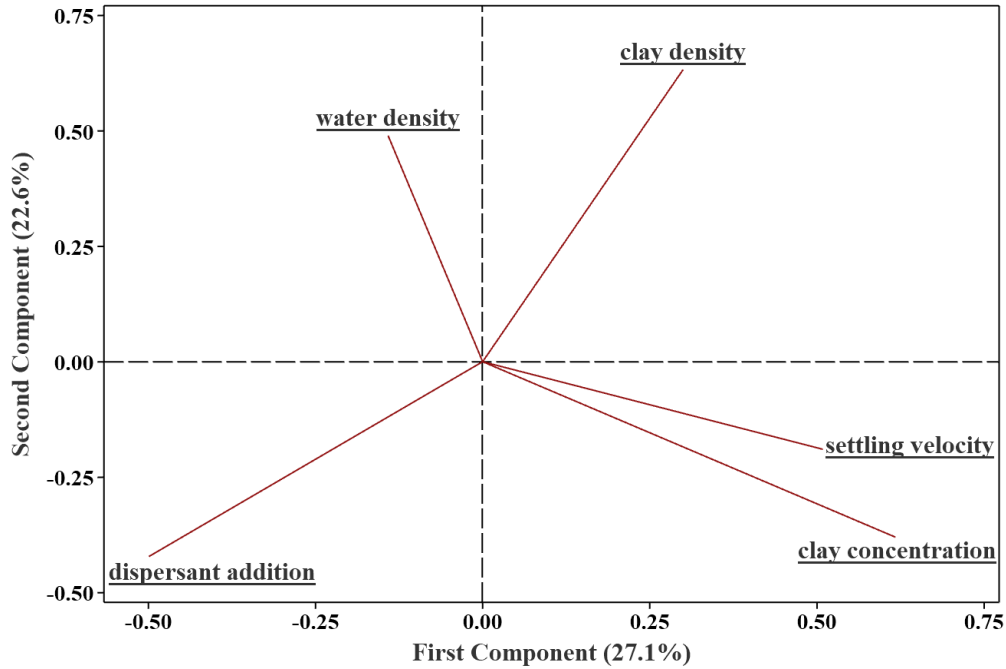


Figure 5.2 The loading plot from principal component analysis of acquired settling velocity data.

5.3 Numerical Modelling on OMA Settling Velocity

5.3.1 Traditional Empirical Approaches

The OMA settling velocity data from the current work were combined with that from Ye et al. (2022) to assemble a more informative and comprehensive dataset, 10637 samples, for prediction. Due to the lack of estimation equations for OMA effective density and settling velocity, the traditional empirical equations of floc effective density and settling velocity estimation were adapted in this study. Seven floc effective density equations and nine floc settling velocity equations were employed, resulting in 63 combinations in total. The details of adapted equations were provided in Table 3.2 and Table 3.3 in Chapter 3 Section 3.3. They were then used to predict the assembled OMA settling velocity data, and the obtained R^2 was presented in Table 5.1. It can be seen from Table 5.1 that the combined equations

from Kranenburg (1994) and Lee et al. (2020) exhibited the best prediction performance with an R^2 of 0.387, which was illustrated in Figure 5.3 as well. Furthermore, the corresponding RMSE results were presented in Table 5.2. The lowest RMSE (1.933) was observed for Kranenburg (1994) and Lee et al. (2020) combination, again, demonstrating the favourability of using the equation from Kranenburg (1994) to calculate OMA density and the equation from Lee et al. (2020) for OMA settling velocity estimation based upon the assembled data. Moreover, the majority of the remaining combinations produced an R^2 value close to zero, which can be attributed to the fact that empirical equations are generally developed and tailored for specific situations. Consequently, the equations from Kranenburg (1994) and Lee et al. (2020) outperformed other combinations when applied to the dataset utilized in this study.

Table 5.1 The coefficient of determination (R^2) from empirical equations for oil-mineral-aggregate's settling velocity prediction.

Settling velocity Density	Van Rijn, 1989 [205]	Soulsby, 1997 [206]	Cheng, 1997 [207]	Curran et al., 2007 [202]	Camenen, 2007 [208]	Sadat-Helbar et al., 2009 [209]	Goldstein & Coco, 2014 [210]	Lee et al., 2020 [226]	Ye et al., 2020 [40]
Tambo & Watanabe, 1979 [198]	0.000	0.000	0.000	0.000	0.000	0.000	0.000	0.000	0.000
Hawley, 1982 [199]	0.138	0.088	0.000	0.000	0.000	0.000	0.040	0.082	0.140
McCave, 1984 [200]	0.000	0.000	0.000	0.000	0.000	0.000	0.000	0.000	0.000
Kranenburg, 1994 [201]	0.306	0.385	0.369	0.000	0.000	0.298	0.000	0.387	0.230
Curran et al., 2007 [202]	0.000	0.000	0.000	0.000	0.000	0.000	0.000	0.000	0.000
Vahedi & Gorczyca, 2017 [203]	0.000	0.000	0.000	0.000	0.054	0.000	0.000	0.000	0.000
Moruzzi et al., 2020 [204]	0.348	0.306	0.198	0.000	0.000	0.098	0.177	0.300	0.351

Table 5.2 The root means square error (RMSE) from empirical equations for oil-mineral-aggregate’s settling velocity prediction.

Settling velocity Density	Van Rijin, 1989 [205]	Soulsby, 1997 [206]	Cheng, 1997 [207]	Curran et al., 2007 [202]	Camenen, 2007 [208]	Sadat-Helbar et al., 2009 [209]	Goldstein & Coco, 2014 [210]	Lee et al., 2020 [226]	Ye et al., 2020 [40]
Tambo & Watanabe, 1979 [198]	2.605	2.645	2.719	3.024	2.850	2.780	2.618	2.649	2.605
Hawley, 1982 [199]	2.292	2.358	2.485	3.024	2.816	2.587	2.419	2.365	2.289
McCave, 1984 [200]	3.011	3.012	3.015	3.024	2.965	3.016	3.009	3.013	3.011
Kranenburg, 1994 [201]	2.056	1.937	1.961	3.024	2.754	2.068	2.514	1.933	2.166
Curran et al., 2007 [202]	2.881	2.894	2.919	3.024	2.896	2.939	2.866	2.896	2.881
Vahedi & Gorczyca, 2017 [203]	55.751	26.522	20.030	3.024	2.485	21.454	23.608	25.990	1042.525
Moruzzi et al., 2020 [204]	1.994	2.057	2.211	3.024	2.786	2.345	2.240	2.065	1.989

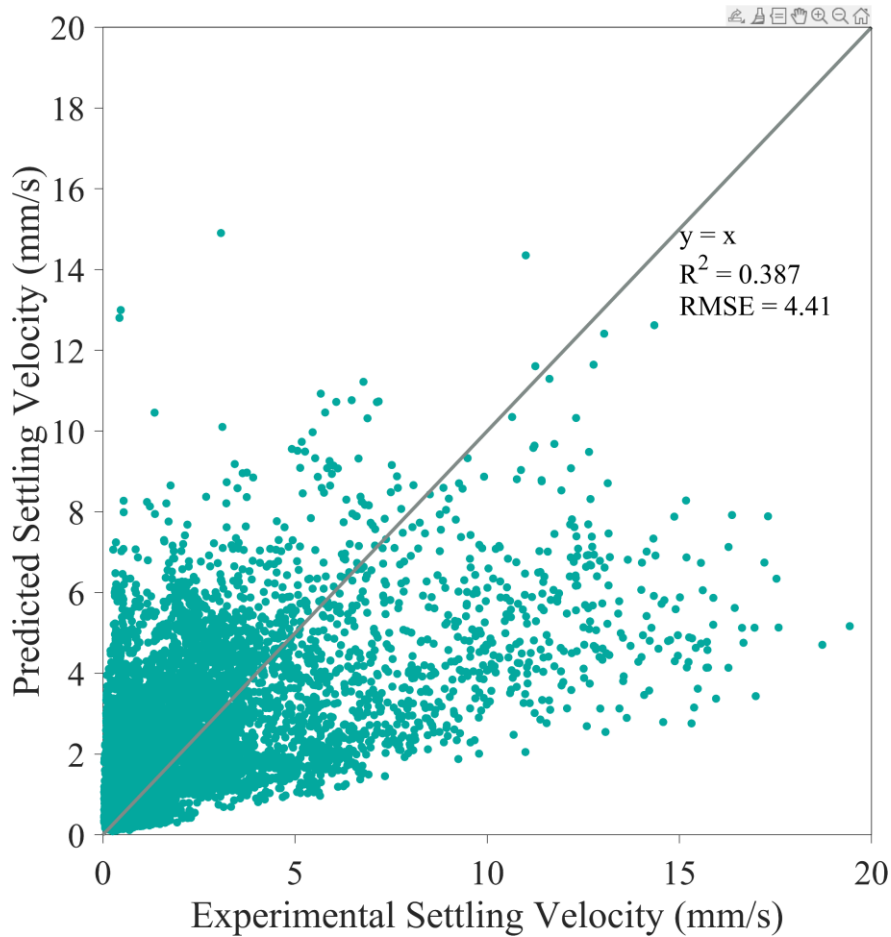


Figure 5.3 The plot of oil-mineral-aggregate’s experimental settling velocity vs. theoretically predicted values. R^2 denotes the coefficient of determination and RMSE denotes the root means square error.

5.3.2 Machine Learning Prediction

Three machine learning algorithms, RF, GBR and Adaboost, as mentioned in Chapter 3 Section 3.4, were implemented to predict OMA settling velocity. The input variables were consistent with that used for empirical prediction, including diameter, water density and clay density. The prediction accuracies of machine learning algorithms are illustrated in Figure 5.4. In general, machine learning prediction exhibited better performances compared to the empirical prediction, as evidenced by their higher R^2 (> 0.6) and lower RMSE (< 1.6). Among them, GBR’s

prediction accuracy (Figure 5.4b) was most satisfying, along with the highest training R^2 (0.645) and testing R^2 (0.614) and the lowest training RMSE (1.469) and testing RMSE (1.535). Therefore, GBR was selected as the most satisfactory machine learning algorithm for OMA settling velocity prediction in this study, which was subsequently employed for OMA trajectory sensitivity analysis in the next Chapter.

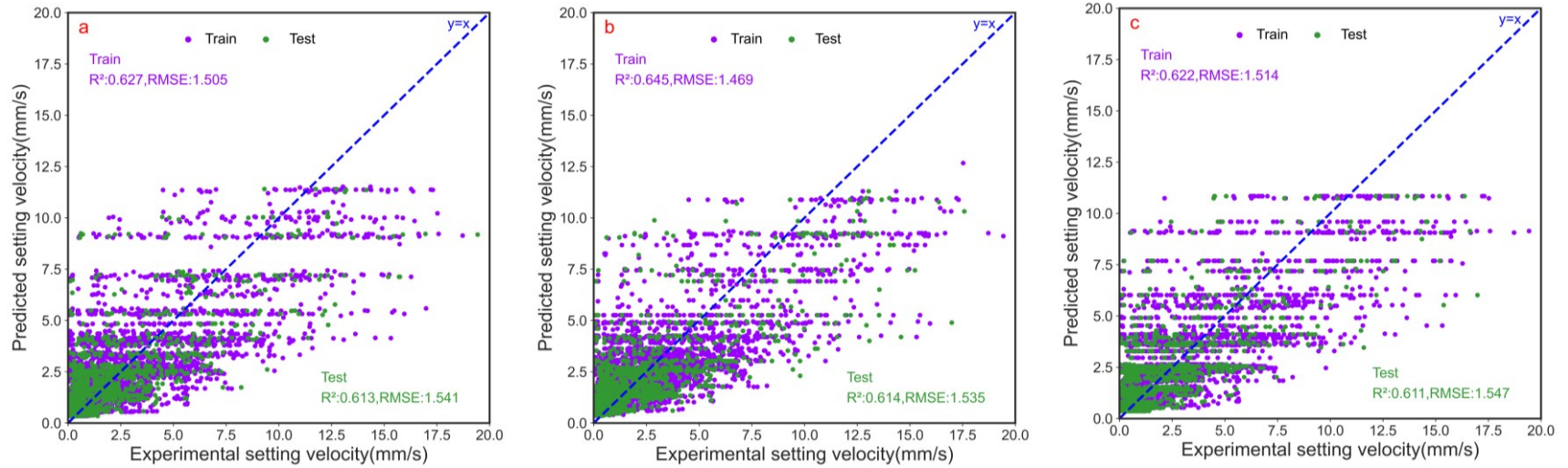


Figure 5.4 Prediction plots (training and testing) for oil-mineral-aggregate's settling velocity by using machine learning algorithms (a) Random Forest, (b) Gradient Boosting Regression, and (c) Ababoost. RMSE denotes root mean square error.

During the OMA settling velocity prediction, the GBR exhibited the highest R^2 value; however, the differences in R^2 values among the algorithms were relatively small and insignificant. Similarly, during the OMA formation prediction, the Adaboost algorithm demonstrated the highest R^2 but only marginally outperformed the other two algorithms. Consequently, when users aim to employ a single method for predicting both OMA median diameter and settling velocity, the selection of an algorithm should be based on the specific purpose, dataset quality, and available computational resources. The three algorithms offer distinct advantages: the RF algorithm is best suited for handling missing and noisy data, while the Adaboost algorithm requires the least amount of time for model training. The GBR algorithm typically delivers the highest prediction accuracy in most situations due to its ability to learn from errors. In summary, the choice of algorithm should be tailored to the user's objectives, dataset characteristics, and computational capabilities to optimize prediction outcomes for OMA median diameter and settling velocity.

5.4 Sensitivity Analysis

5.4.1 Hypothetical Case Study in A Square field

The influence of OMA settling velocity on the deposition of OMA in the marine environment was investigated. The empirical prediction equation and machine learning algorithm with the highest R^2 (a combination of Kranenburg (1994) and Lee et al. (2020) and GBR algorithm in this study) was incorporated into the particle tracking model (Equation 3.4) in parallel. Since the settling velocity in the literature equations (Table 3.2 and Table 3.3) were diameter dependent, OMA

was grouped by diameter with the interval of 6 μm , and the resultant mean velocity was used. 102 classes with size ranging from 14 μm to 626 μm were employed in particle tracking based on the experiment and literature data [40]. Particles were randomly released in a 2×2 km field, then tracked for 48 h driven by a constant current of 0.2 m/s. Moreover, two simulations were set up that differ by the current direction. The current direction was in the northeast in the first case and changed 30 degrees every 2 hours in the second case. The water depth was assumed to be 20 m to simulate the nearshore environment.

The resulting deposition of OMA is depicted in Figure 5.5 and Figure 5.6. It is evident that the OMA distribution is highly sensitive to the prediction accuracy of settling velocity, which in turn affects the settling velocity magnitude of OMA. Figure 5.5a and Figure 5.6a display the OMA distribution derived from empirical equations (R^2 of 0.387), while Figure 5.5b and Figure 5.6b illustrate the distribution obtained using a machine learning algorithm (R^2 of 0.614) for settling velocity estimation. Under the specific conditions implemented in this study, reduced prediction accuracy resulted in a more dispersed (less concentrated) OMA distribution.

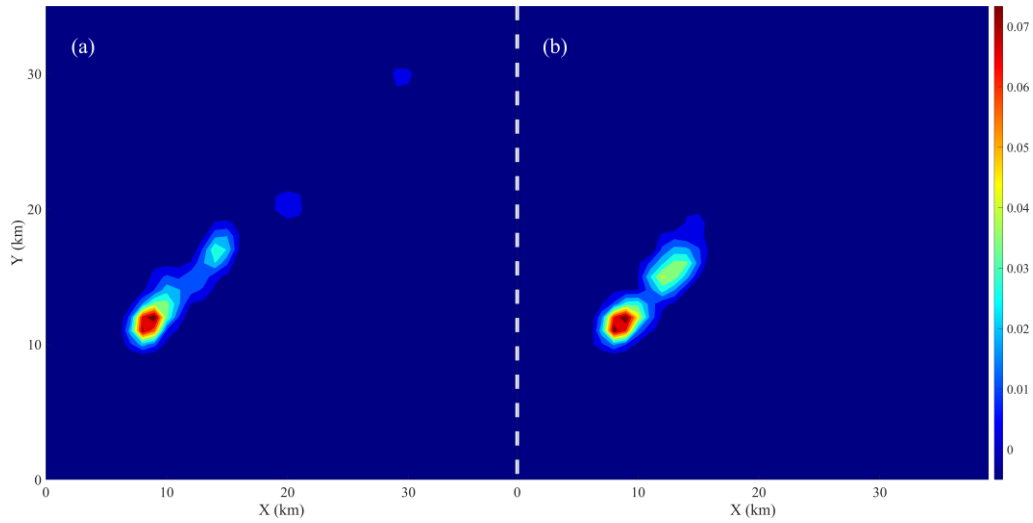


Figure 5.5 The distribution of oil-mineral-aggregates when it was randomly released in a 2×2 km field by using (a) traditional floc equation and (b) machine learning algorithm for settling velocities prediction forcing by a constant current (0.2 m/s) in the northeast direction.

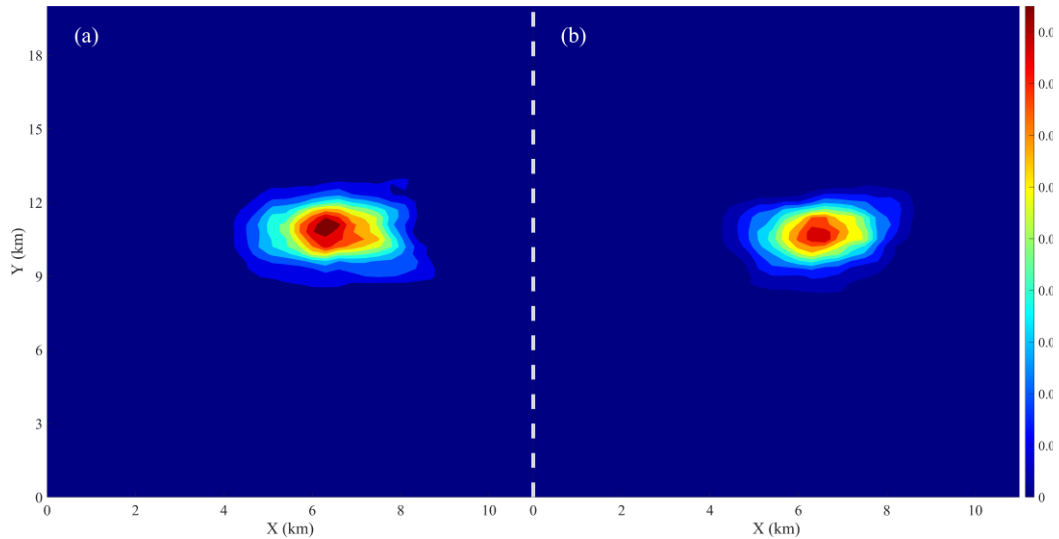


Figure 5.6 The distribution of oil-mineral-aggregates when it was randomly released in a 2×2 km field by using (a) traditional floc equation and (b) machine learning algorithm for settling velocities prediction forcing by a constant current (0.2 m/s) that change 30 degrees of direction every 2 hours.

In order to gain more insights, the sensitivity of different sizes of OMA deposition to settling velocity prediction accuracy was explored, as shown in Figure 5.7. The settling velocity prediction accuracy was influential for the small size OMA as illustrated in Figure 5.7a. A lower prediction accuracy resulted in the maximal travel distance of ~25 km, which was much longer than ~10 km for the counterpart. However, for the medium size OMA (Figure 5.7b) and large size OMA (Figure 5.7c), using different prediction methods (varying prediction accuracies) did not exhibit a profound impact on the OMA distribution. This result revealed that the long OMA travel distance in Figure 5.5a was mainly due to the small size of OMA. Overall, from this sensitivity analysis, we found that the extent of OMA deposition was sensitive to the prediction accuracy of settling velocity, especially for the small size OMA.

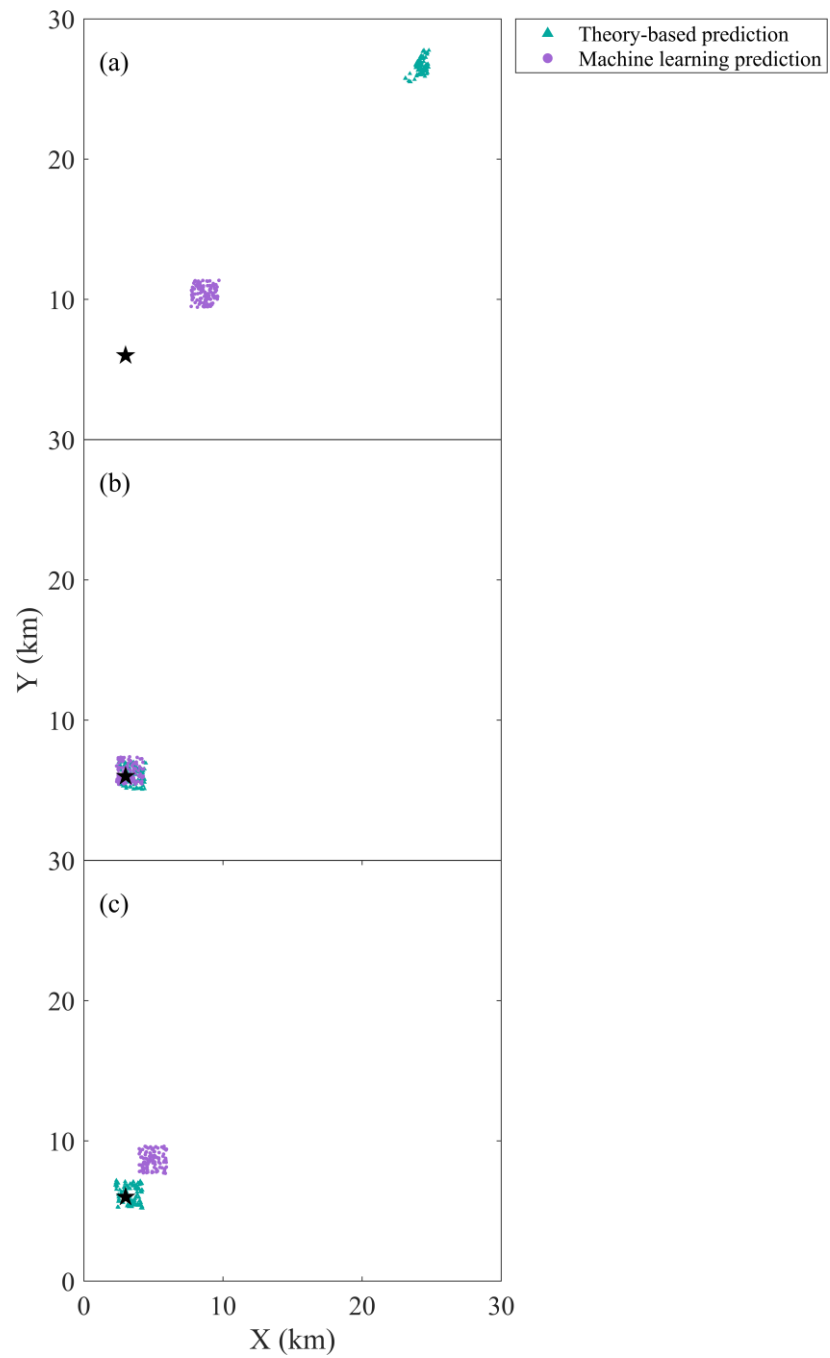


Figure 5.7 The trajectories of oil-mineral-aggregates with different sizes (a) small size, (b) medium size, and (c) large size. Particles were released at a location marked by the black star.

5.4.2 Hypothetical Case Study in Burrard Inlet

In addition to the sensitivity analysis in an ideal environment, the OMA distribution simulation in a real location was also conducted. The presence of OMA was assumed to occur in anchorage #12 in Burrard Inlet, Vancouver, where the *MV Marathassa* oil spill happened. The city of Vancouver on the southwest coast of British Columbia, Canada, centers around Burrard Inlet. At its western end, Burrard Inlet connects to the Pacific Ocean *via* the Strait of Georgia. The inlet is narrow and extends about 30 km inland from the Strait of Georgia to the Indian Arm. In this study, Burrard Inlet (Figure 5.8) was defined to include the Outer Harbour, First Narrows (around 880 m wide), the Inner Harbour (about 8.8 km long; also called Vancouver Harbour), Second Narrows (around 330 m wide), and the Central Harbour (around 7.8 km long) [227]. The southeast portion of the Outer Harbour is an open bay known as English Bay, which has a narrow inlet called False Creek.

The water depths at First Narrows and Second Narrows are 15 m and 19 m, respectively. Tidal currents can be as high as 2 m s^{-1} when tidal mixing is at its greatest at these two Narrows [62,228]. Tidal currents are a major dynamic process in Burrard Inlet. Tides enter the Outer Harbour through the Strait of Georgia and propagate into the Inner Harbour through First Narrows. The semi-diurnal M_2 component (12.42 h period) and two diurnal components, the diurnal K_1 component (23.93 h period) and the lunar diurnal O_1 component (25.82 h period), dominate the tides with a mean tidal range of 3.3 m and a maximum tidal range of about 5 m [63, 229–231].

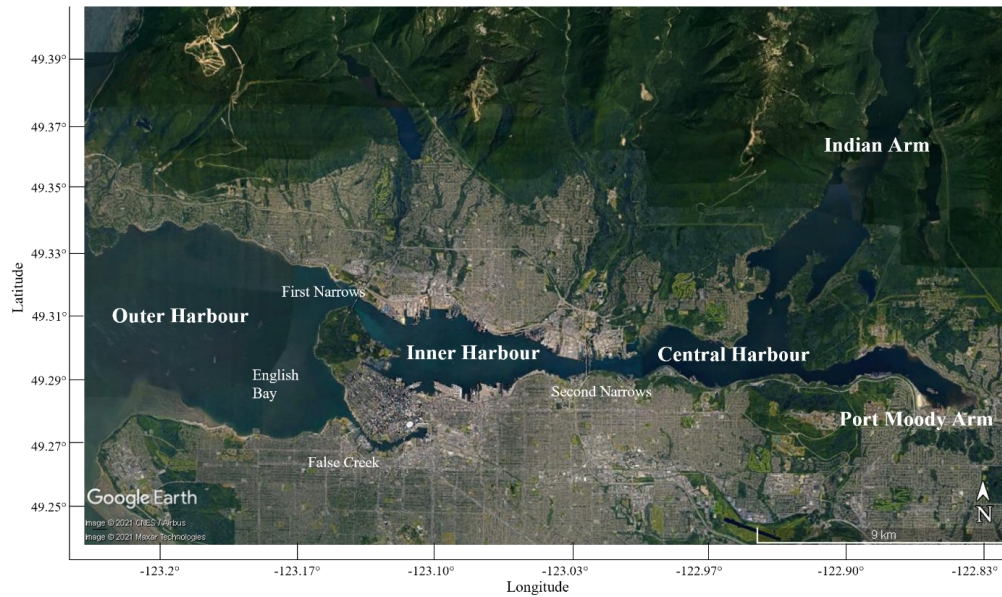


Figure 5.8 Burrard Inlet is located on the southwest coast of British Columbia and connects with the Pacific Ocean *via* the Strait of Georgia at its western end. Burrard Inlet geographically includes the Outer Harbour, First Narrows, Inner Harbour, Second Narrows, and Central Harbour.

Burrard Inlet holds a high risk of oil spills due to its heavy maritime traffic. In addition, OMA is likely to be formed once an oil spill occurs in the area due to the high concentration of suspended sediments. Therefore, anchorage #12 in Burrard Inlet was selected to evaluate how the OMA settling velocity prediction accuracy affects the extent of OMA deposition in Burrard Inlet. The hydrodynamic forcing used in this study was generated by the FVCOM [232]. The FVCOM model used in this study was validated by Wu et al. (2019). The OMA class setting and settling velocity prediction of each group can be found in Section 6.2. Particles were released in anchorage #12 and tracked for 48 hours with a time step of 20 min following Equation 3.4. The particle positions were recorded every hour.

It can be seen from Figure 5.9a (a relatively low settling velocity prediction accuracy) that a portion of OMA was transported into the Vancouver harbour through the First Narrows, with some ended up on the southern shoreline of Vancouver Harbour. Conversely, when employing the highly predictive settling velocity derived from the machine learning algorithm (Figure 5.9b), all OMA remained in the Outer Harbour, emphasizing the significance of accurate settling velocity prediction for OMA trajectory determination. In Figure 5.9a, the OMA transported into Vancouver Harbour are likely dominated by smaller OMA. This inference is supported by the sensitivity analysis concerning the predicted settling velocities of various OMA sizes and their corresponding deposition patterns, which revealed that lower prediction accuracy is associated with increased travel distances for smaller OMA. Considering the maximum water depth in the Outer Harbour is 45 m [234] and the current's initial direction was towards the western of the inlet, it is expected that OMA with higher settling velocities would settle before being transported into Vancouver Harbour.

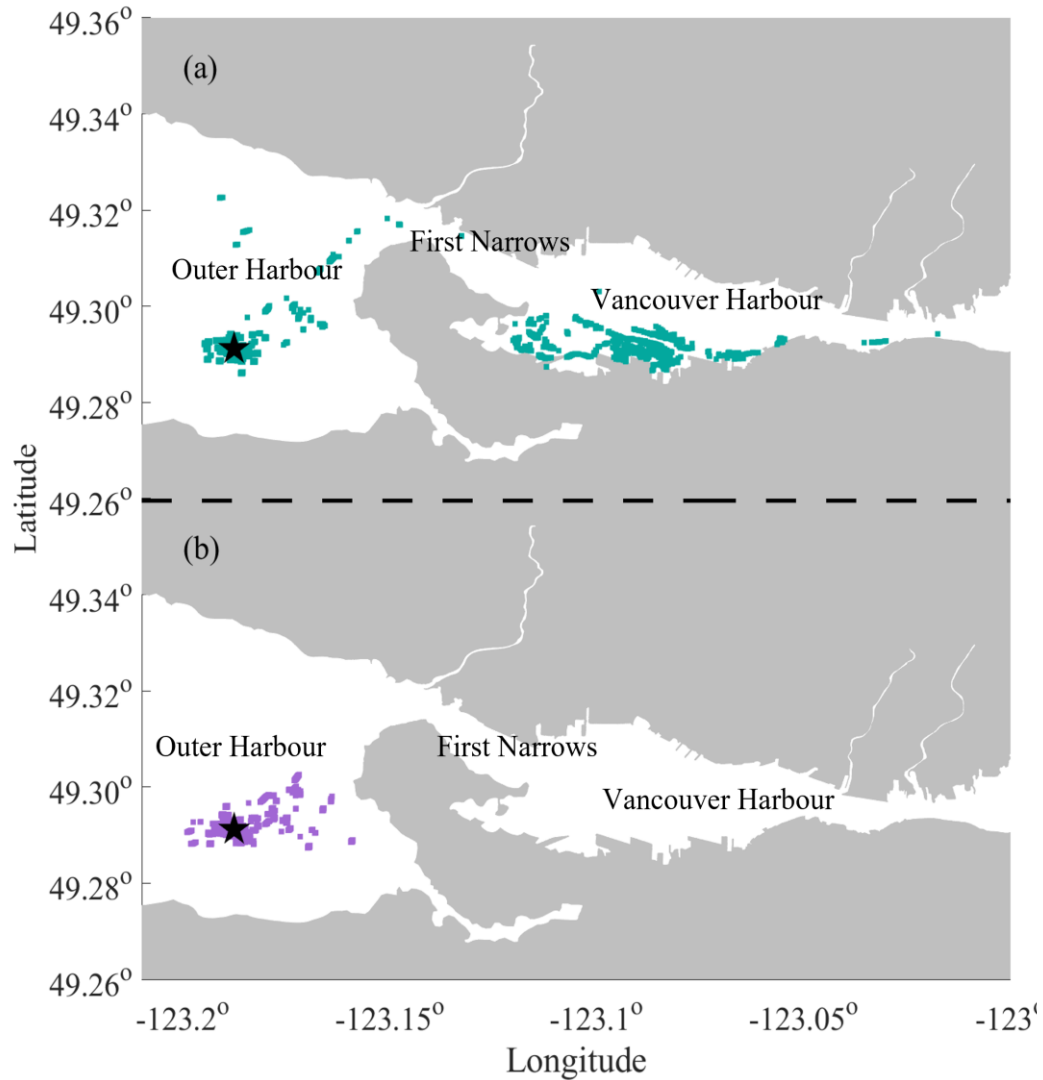


Figure 5.9 The trajectories of oil-mineral-aggregates in a real location (Burrard Inlet, Vancouver) by using (a) traditional flocculation equation and (b) machine learning algorithm for settling velocities prediction. Particles were released at black star.

5.5 Summary

Although settling and transport of OMA are extremely important for accurate oil spill modelling, limited efforts have been contributed to explore this subject. Laboratory setups were constructed in this study to measure the OMA

settling velocity by coupling a high-speed camera and magnifying lens. The settling velocity of observed OMA varied from 0.2 mm/s to 3 mm/s, with the majority of 0.2 – 1 mm/s. The principal component analysis was also applied to investigate how the process variables affected the OMA settling velocity. It was found that the clay concentration in the water environment positively and strongly correlated with OMA settling velocity. The dispersant addition and water density increment led to the reduction in OMA settling velocity. We also, for the first time, employed machine learning algorithms (RF, GBR and Adaboost) to predict the OMA settling velocity, and GBR exhibited the best prediction accuracy (testing R^2 of 0.614 and RMSE of 1.535) among the three tested algorithms. Compared to traditional empirical estimation (R^2 of 0.387), machine learning prediction had a much higher prediction accuracy, implying its promising potential in OMA settling velocity prediction.

The sensitivity analysis of OMA deposition with different prediction accuracies of OMA settling velocity revealed that a lower prediction accuracy led to a wider (less concentrated) spread of OMA, which was attributed to the small size of OMA. A hypothetical case study in Burrard Inlet, Vancouver, revealed that all OMA remained at the Outer Harbour when a highly predictive settling velocity model was employed. However, part of OMA could be transported into the Vancouver Harbour through the First Narrows, and some ended up on the southern shoreline of Vancouver Harbour when a less accurate OMA settling velocity model was implemented, which once again suggested the importance of accurate settling velocity prediction for OMA deposition. Such a comprehensive study on OMA

settling will help to build a solid foundation to track the oil spill in marine environments.

5.6 Transition Section

The OMA settling velocities were successfully tracked by the assembled high-speed camera and magnifying lens in Chapter 5. Clay concentration and density were found to be positively related to OMA settling velocity, which was, however, negatively influenced by the presence of dispersant and water density increment. Once again, machine learning algorithms exhibited better prediction performance than traditional empirical floc equations for OMA settling velocity estimation. Nevertheless, how OMA transport would respond to using different settling velocity models that have varying prediction accuracies remains unknown. Particle tracking studies demonstrated the high sensitivity of OMA trajectory to the accuracy of settling velocity prediction, in which machine learning algorithms were applied to improve the prediction accuracy of OMA settling velocity. In addition to machine learning prediction, a few other tools can be employed to aid in oil spill modelling. FTLE has received much research interest in understanding how nutrients, pollutants, suspended sediments, and waterborne planktonic biota in coastal oceans would distribute and evolve. Unfortunately, scarce efforts have been made to evaluate the feasibility of using FTLE for the spilled oil's trajectory analysis. Chapter 6 therefore employed FTLE analysis to study the oil spill in Burrard Inlet, Vancouver, one of the busiest water areas in Canada.

Chapter 6 Applying Finite-Time Lyapunov Exponent to Study the Tidal Dispersion Properties in Burrard Inlet

Copyright permission:

This chapter combined with Chapter 8 has been published in the Journal of Hazardous Materials 437(8):129404. The copyright has been obtained from Elsevier and co-authors.

Contribution statement:

I was responsible for velocity fields data analysis, oil spill model simulation, pre- and post-processed results and manuscript drafting.

6.1 Particle Tracking Algorithm

The particle tracking algorithms were described in Equation 3.3 in Chapter 3 Section 3.5. The results of particle trajectories and instantaneous velocities were recorded every five minutes. The positions of particles were used to calculate the FTLE values. The magnitude and direction of currents in each grid over 30 days were averaged to estimate the residual current by using t-tide toolbox [212]. The tidal cycle was assumed to be 26 hours, and the particles (10 in each grid) were released every hour to simulate the trajectories, which were further utilized to obtain the tidal excursion. The results of 260 runs ($26 \text{ h} \times 10 \text{ particle}$) were then averaged to create the map of tidal excursion length.

6.2 General Descriptions for FTLE

The FTLE is denoted as $\phi_t^T(\mathbf{x})$ for a given location x and time t in a flow field. The FTLE is a scalar that measures the separation between particle traces which are spatially close to x , over the time interval t to $t + T$. The FTLE was computed following Haller (2001):

$$\phi_t^T(\mathbf{x}) = \frac{\ln\sqrt{\lambda_{\max}(\Delta)}}{|T|} \quad (6.1)$$

where $\lambda_{\max}(\Delta)$ represents the maximum eigenvalue of the symmetric matrix Δ , and Δ is the Cauchy-Green deformation tensor represented by:

$$\Delta = \left(\frac{d\phi_t^T(\mathbf{x})}{dx} \right)^T \times \frac{d\phi_t^T(\mathbf{x})}{dx} \quad (6.2)$$

The definition of the FTLE allows for positive and negative T . For a positive time, the FTLE measures the separation forward in time and yields a repelling LCS. For a negative time, the FTLE measures the separation backward in time and yields an attracting LCS. To generalize the finite-time classic concept of normally hyperbolic invariant manifolds in dynamic systems, d'Ovidio et al. (2004) combined the normalized forward and backward FTLE fields to get hyperbolic FTLE fields:

$$\text{FTLE}^\pm = \frac{\text{FTLE}^+}{\text{FTLE}_{\max}^+} - \frac{\text{FTLE}^-}{\text{FTLE}_{\max}^-} \quad (6.3)$$

Because square grid cells were required to calculate the FTLE, a horizontal grid with a spacing of 40 m between grid cell centers was defined for the entire

inlet at $t = 0$. Then particle was released in each grid cell. Start times at four different phases of the tide (low tide, mid-flood, high tide, and mid-ebb) were chosen for the spring and neap tides. The integration time (T) was 26 hours for the forward and backward FTLE fields because it covered all the main tidal constituents.

The LCS lines are estimates of the transport barriers in the modelled flow. In this study, the LCS lines were extracted by analyzing the FTLE fields for thresholds of 0.5, 0.7, 0.8, and 0.9 [160]. The results showed that the threshold equal to 0.8 was suitable for highlighting the LCS in Burrard Inlet. Therefore, any FTLE values higher than 80% of the FTLE maximum were defined as the LCS. Finally, the LCS lines were compared with observed Lagrangian drifter data that were obtained from two Surface Current Tracker (SCT) drifters released at 8:42 and 9:11 on Nov. 8, 2015. The drifter locations were recorded every two to six minutes, and velocities were calculated from those recorded positions. The drifter data records were 12 hours and 10 days long for the two- and six-minute recorded data, respectively. The SCT design is described in Page et al. (2019).

6.3 Stochastic Simulation

A case study of a hypothetical oil spill was conducted, and the potential trajectories of the oil spill case were compared with the results of the FTLE analysis. The case study involved the same volume and type of spilled oil (2800 L of IFO-380) as in the *MV Marathassa* spill [228]. To explore the trajectory of the spilled oil, six possible release sites in Burrard Inlet were selected (as shown in Figure 6.1), and the trajectories using the Oil Spill Contingency and Response (OSCAR) model

with a stochastic approach were followed. Details about the OSCAR model are in Reed et al. and Aamo et al. [237–239].

The hydrodynamic forcing used for this study was generated with FVCOM. FVCOM is a three-dimensional, finite-volume ocean model with an unstructured grid. Chen et al. (2003) first developed FVCOM, and researchers from the University of Massachusetts, Dartmouth, and Woods Hole Oceanography Institute [241–243] upgraded the model. The coastline and bathymetric data were obtained from the Canadian Hydrographic Service. The model domain's horizontal grid spacing varied from ~ 1 m in the Inner Harbour to ~ 1 km in the open ocean. In the vertical direction, 21 sigma levels were used with enhanced resolutions at the surface and bottom layers. The model is a barotropic model and runs with a constant temperature and salinity. The model was driven by tides along the open boundaries, and the tides were derived from the tidal harmonic constants from Foreman et al. (2000). The model was validated with observed water elevations and water currents, and more detailed information on the model setup and model validation can be found in Wu et al. (2019). To clearly demonstrate and isolate the extraordinarily complex flow patterns that the tidal currents generate, surface wind forcing was not included in this study.

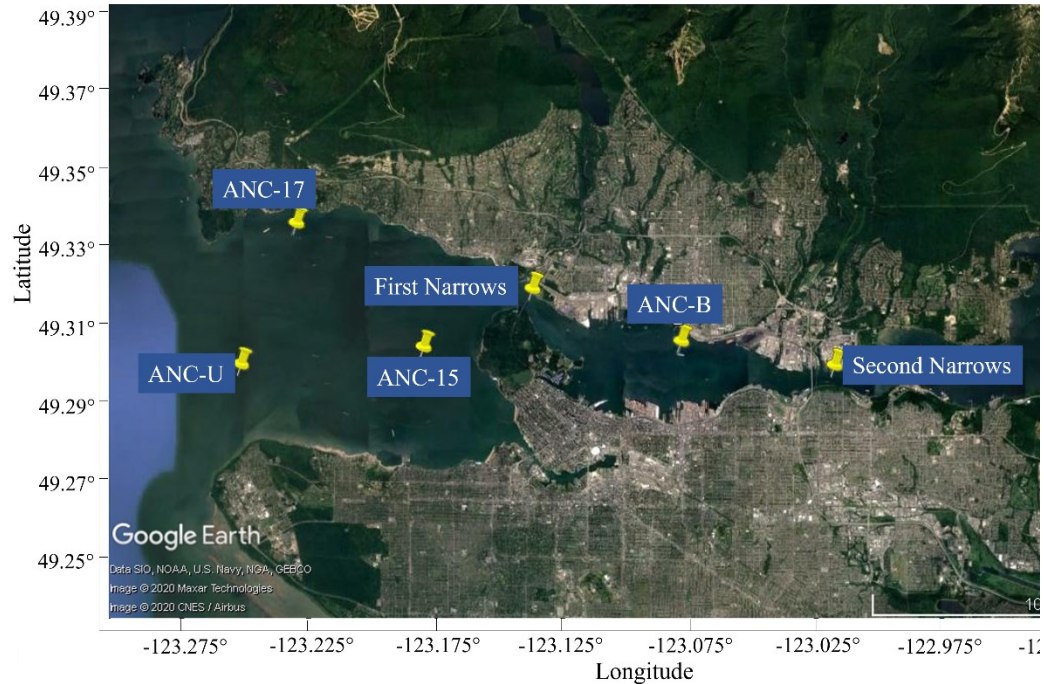


Figure 6.1 Six oil release sites in Burrard Inlet: ANC-U, ANC-17, ANC-15, First Narrows, ANC-B, and Second Narrows, from west to east of the inlet.

Stochastic analysis is commonly used to assess the potential risk of an oil spill by overlapping a large number (tens to thousands) of individual deterministic simulations. In this study, a stochastic approach was employed to simulate the fate and behaviour of an oil spill happening between Feb. 5 to Mar. 7, 2017 (30 days) using current velocity data from FVCOM. At each of the six hypothetical release locations (Figure 6.1), there were 12 simulations with different start times, evenly distributed during the 30-day period. For each simulation, the oil was released uniformly over the first two hours and was tracked for seven days. The critical parameter settings and the longitudes and latitudes of the release sites for the stochastic oil spill modelling are summarized in Table 6.1. The stochastic model results did not provide the extent of any individual spill event, but the results

summarized all the simulations. The summarized information was used to generate maps of the probability of contamination throughout the inlet.

Table 6.1 The key parameters settings and the release site locations for the stochastic oil spill modelling.

Parameter	Setting	
Period of simulation (days)	30	
Number of simulations	12	
Duration of each simulation (days)	7	
Duration of oil release (hrs)	2	
Type of released oil	IFO 380	
Amount of release oil (L)	2800	
Release sites	Latitude	Longitude
ANC15	49.300278	-123.181389
ANC17	49.332222	-123.231667
ANC-U	49.295833	-123.253611
ANC-B	49.301667	-123.079444
First Narrows	49.315260	-123.138266
Second Narrows	49.295365	-123.018871

6.4 FTLE Analysis Results

In this study, the FTLE results were normalized with the maximum FTLE ($FTLE/FTLE_{max}$) for the forward and backward fields separately [160]. Then, the forward and backward FTLEs were combined to obtain the hyperbolic FTLE field

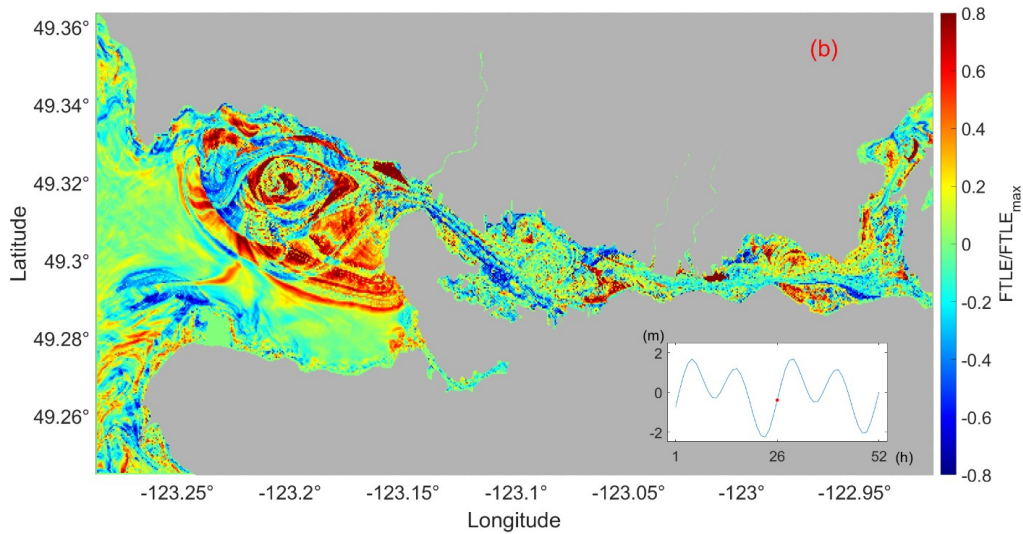
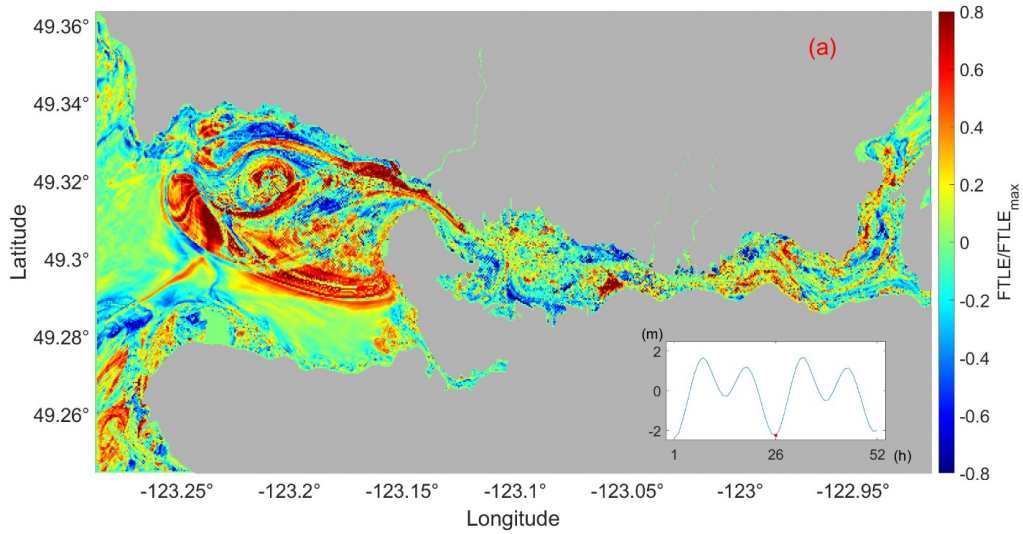
(see Equation (6.3)) [235]. This combined FTLE field provided the potential hyperbolic LCS and dominant hyperbolic saddle points, where repelling and attracting material lines meet. A hyperbolic LCS is locally the strongest repelling or attracting material surface over a finite time interval [246], and the saddle points are the main hidden features that dictate the mixing and stirring of tracers in the flow field [160]. The hyperbolic FTLE field for a typical spring tide and neap tide and the corresponding water levels are presented in Figure 6.2 and Figure 6.3, respectively. As mentioned in Section 6.2, the FTLE field highlights the repelling (red) material lines and attracting (blue) material lines, indicating the potential pathways for material transport by spreading and accumulating, respectively. Inferring flow direction from the FTLE fields is not trivial. Near the saddle points, the flow along the red lines must be into the saddle point, and the flow along the blue lines must be outward. Thus, in the figures (Figure 6.2 and Figure 6.3), flow in a particular direction changed color as it followed the red lines into a saddle point and the blue lines outwardly. Regions that did not have an obvious LCS, and were more of a random mixture of red, yellow, green, and blue, were regions where the flow tended to mix particles rather than transport them long distances. The description of the FTLE focuses on the most coherent features.

The FTLE fields for the low tide release during the spring tide (Figure 6.2a) were first interpreted. The most obvious features were the several red LCSs in the Outer Harbour and the red material line extending from the eastern end of First Narrows, through the narrows, and along the northern edge of the Outer Harbour. There was also a blue material line through First Narrows connecting the Inner and

Outer harbours. In the Inner Harbour, there were two blue material lines along the southern side, a strong red feature to the south of the entrance to Second Narrows, and a blue one to the north of the Inner Harbour. Second Narrows did not have any obvious LCS features. There were some coherent linear material lines in the Central Harbour and into the Indian Arm, but they were not as strong (consistently red or blue) as the lines in the Outer Harbour. The hyperbolic saddle points were used to infer some of the flow directions. The red material line along the northern side of First Narrows was outward towards the Outer Harbour (the ebb tide jet). The red material lines that extended from the central part of the Outer Harbour to the eastern coastline were directed towards the coast. The northeastward extension, along the coast towards First Narrows, expressed the tidal residual flowing towards the entrance of First Narrows along the coast.

The details of the flow structure and the locations of the saddle points varied as a function of the release time. However, there were some consistent features (Figure 6.2): large coherent structures in the Outer Harbour (the details of the patterns varied); red material lines from the center of the Outer Harbour to the eastern coastline; and a material line through the First Narrows (weakest for the high tide release, Figure 6.2b, when a red coherent structure blocked the western end of the narrows). In none of the simulations was there a material line connecting the First and Second Narrows. For the mid-flood tide release (Figure 6.2b), the material line in First Narrows extended to the southern coastline of the Inner Harbour. In addition, the material lines were separated more distinctly in the Outer Harbour than in other regions. The fact that material lines in the Inner Harbour and

Second Narrows were more tightly packed and less distinct (often looking like a random mess of red, yellow, green, and blue), says that there was more mixing and less net transport than in the Outer Harbour.



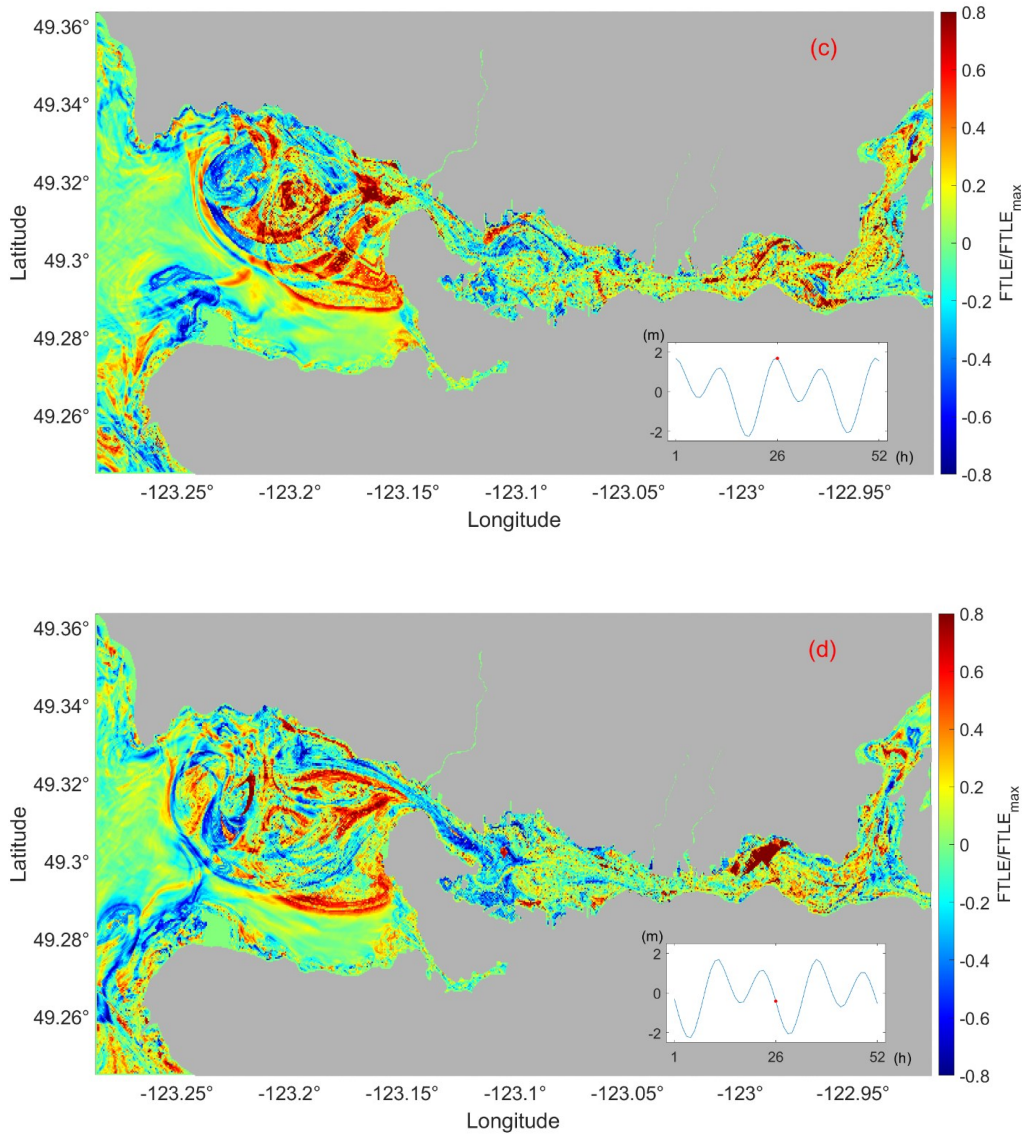
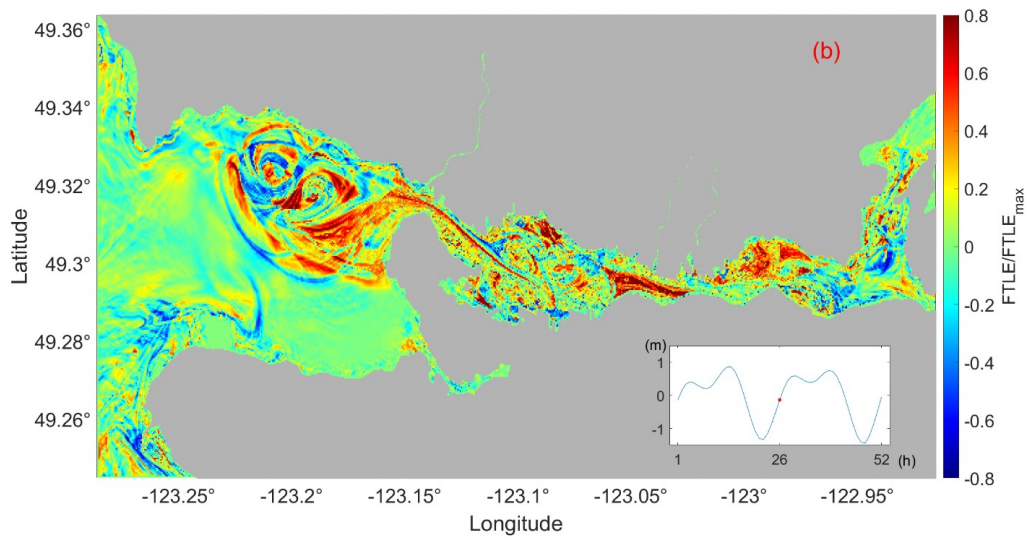
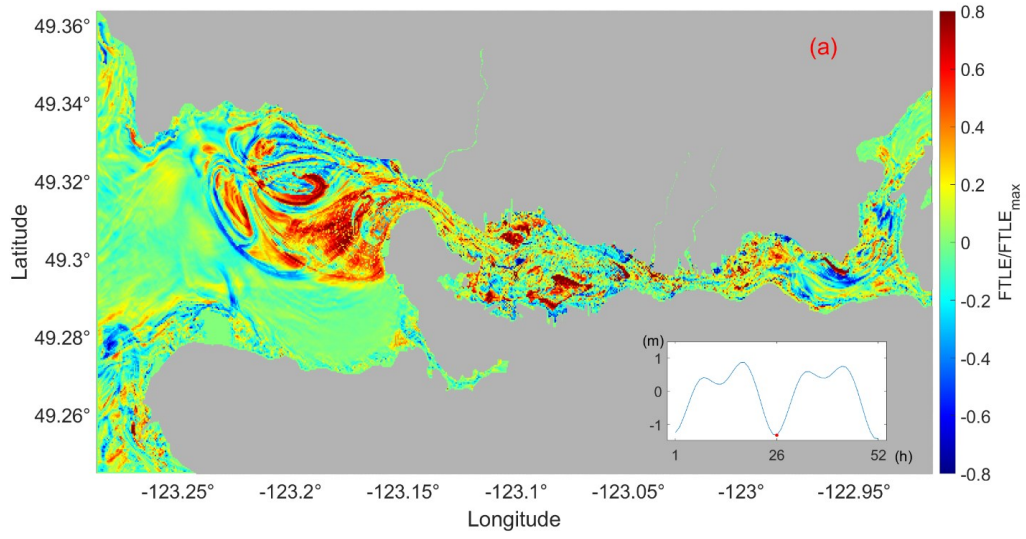


Figure 6.2 The normalized hyperbolic FTLE fields for Burrard inlet during spring tide for particles released at (a) low tide; (b) mid-flood tide; (c) high tide; (d) mid-ebb tide. One particle was released at each grid. The time history of the tide is shown in the inset. The $FTLE^+$ calculation extends 26 hrs forward of the red dot and the $FTLE^-$ calculation extends 26 hrs backward in time.

As for the neap tide (Figure 6.3), the material lines in the Outer Harbour were mostly distributed in the northeast and worked as transport barriers preventing the particles from moving into English Bay. The particles were easily transported

between the Outer Harbour and Inner Harbour through First Narrows because there were clear pathways along the First Narrows. However, the particles that moved between the eastern and western Inner Harbour were impeded as evidenced by the tightly packed material lines during low tide (Figure 6.3a) and the material lines directed north-south for the other tidal phases (Figures 6.3b, 6.3c, and 6.3d)). The impeded movement indicated that the particles in the Inner Harbour were hard to transport into the Central Harbour and vice versa. Furthermore, two eddies formed in different locations in the Outer Harbour when the particles were released during the different tidal phases (Figure 6.3).

Overall, the FTLE results suggest that the dynamics of the western (Outer Harbour and First Narrows) and eastern parts of the inlet (Second Narrows and Central Harbour) were different. The material lines were distinctly separated in the Outer Harbour, and strong mixing and stirring occurred in the eastern inlet. Furthermore, for neap and spring tides, water exchanged easily between the Outer Harbour and the Inner Harbour through First Narrows, but the water exchange between the eastern and western ends of the inlet decreased in the Inner Harbour due to the complex FTLE pattern. More detailed versions of Figure 6.2 and Figure 6.3 are presented in Figure S6.1 in APPENDIX B, and the details are summarized in Table S6.1 in APPENDIX B.



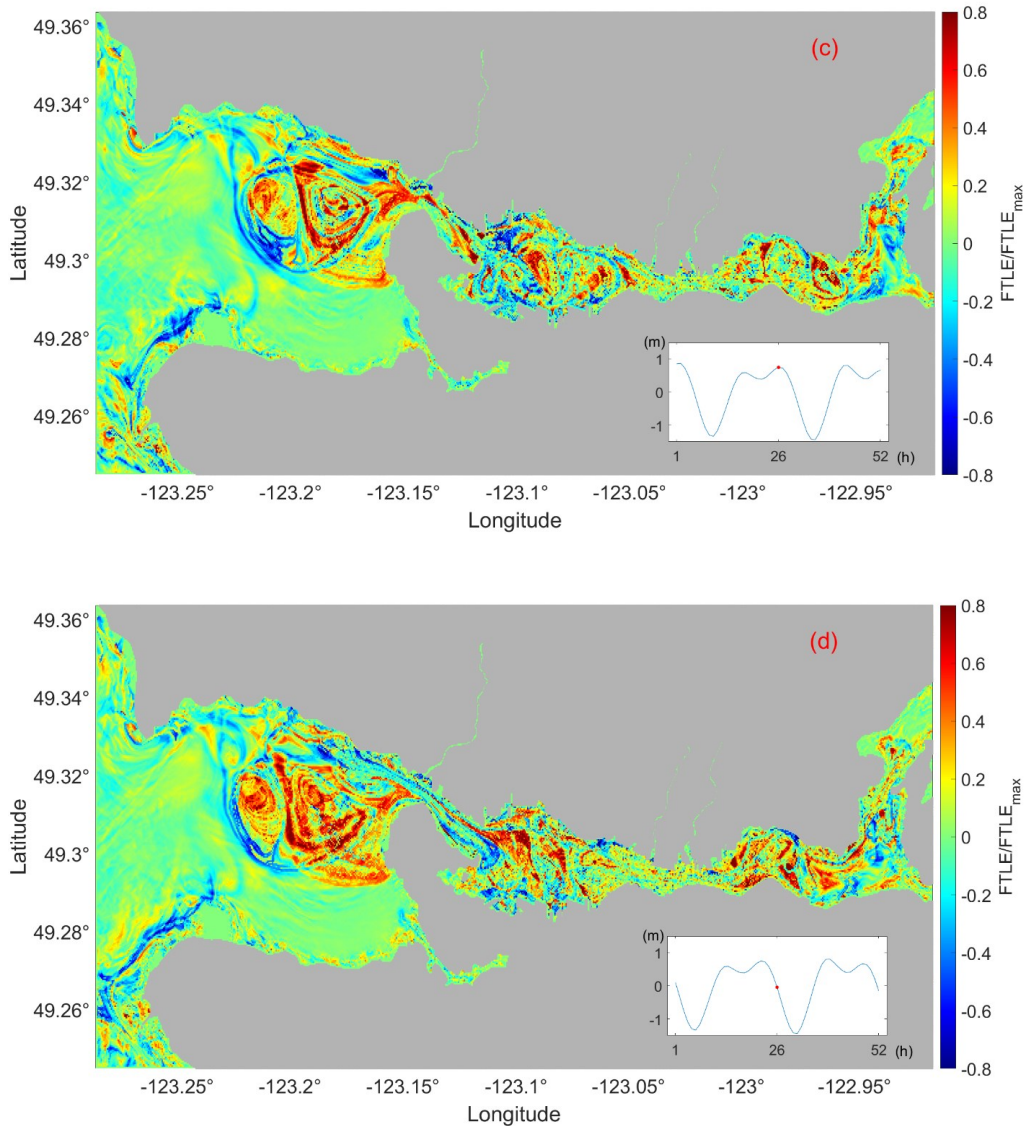
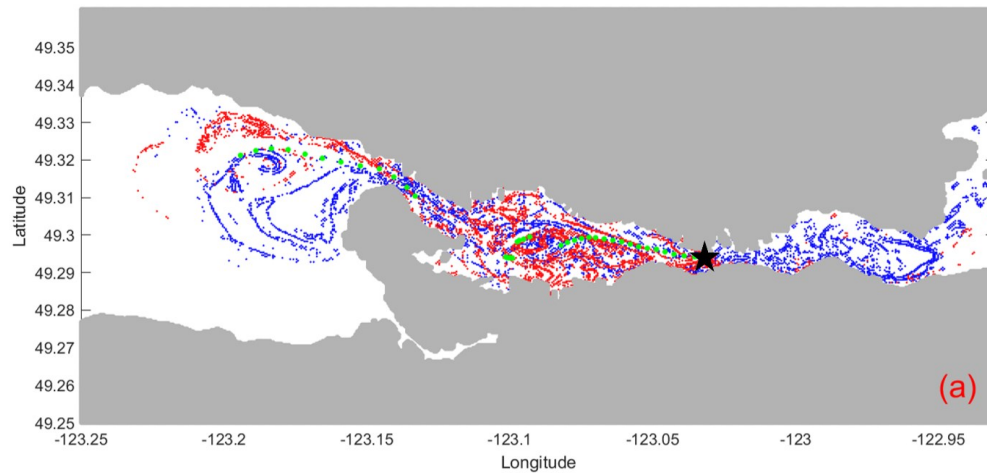


Figure 6.3 The normalized hyperbolic FTLE fields for Burrard inlet during neap tide for particle released at (a) low tide; (b) mid-flood tide; (c) high tide; (d) mid-ebb tide. Particles were released in each grid cell. The time history of the tide is shown in the inset. The $FTLE^+$ calculation extends 26 hrs forward of the red dot and the $FTLE^-$ calculation extends 26 hrs backward in time.

The FTLE fields describe the tidal dispersion properties and are useful when analyzing horizontal transport. The LCS lines extracted from the FTLE fields are relevant to the trajectories of surface drifters. The drifters will not cross LCS lines;

instead, they will follow the water bodies that the LCS lines define. In this study, by checking NOAA's tides and currents website (<https://tidesandcurrents.noaa.gov/>), the tidal phase coincided with the time the surface drifters were launched was selected. The FTLEs higher than 80% of the FTLE maximum were defined as LCSs. The LCSs were compared with the experimental Lagrangian drifter data and the results were illustrated in Figure 6.4. For the drifter deployed at Second Narrows (Figure 6.4a), the drifter first moved to the Inner Harbour following the repelling lines (red), then it moved further to the Outer Harbour along the attracting lines (blue). For another drifter deployed in the Central Harbour, Figure 6.4b shows that the drifter moved to Second Narrows followed the attracting lines (blue), and then moved to the Inner Harbour along the repelling lines (red). Therefore, these drifter trajectories were consistently aligned with the LCS lines.



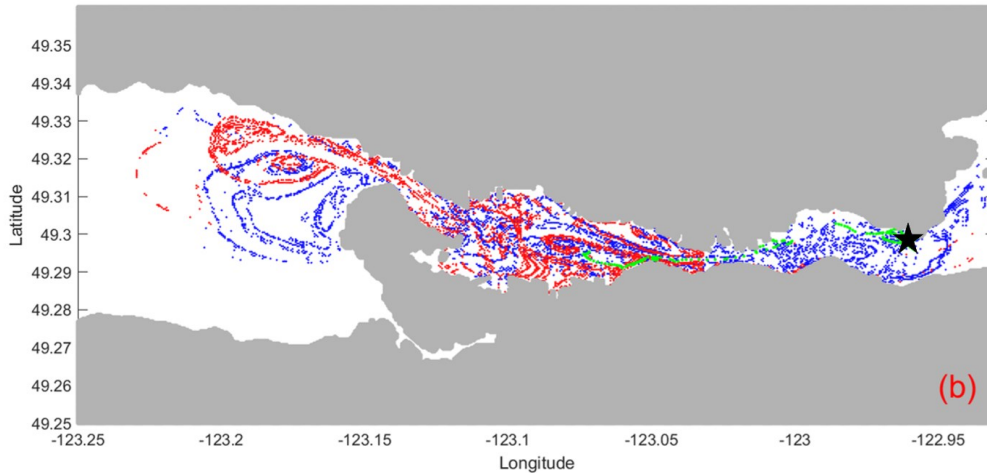


Figure 6.4 Comparison of drifter data with FTLE ridges. Particles were released in each grid cell. Drifters were deployed at (a) Second Narrows and (b) the Central Harbour. The black stars indicate the drifter release locations, and the green points depict the observed drifter trajectories. The red lines represent the repelling LCSs, and the blue lines represent attracting LCSs. The white spaces are where FTLE values were lower than or equal to 80% of the FTLE maximum.

6.5 Tidal Dispersion Properties

Several observations and simulations demonstrated that particle trajectories in coastal areas are very sensitive to their initial release locations and dates [49,50,247–250]. FTLE fields, which can be considered sensitivity maps for initial conditions over a finite time interval [148], directly address this sensitivity. The FTLE analysis showed that the spatial structures of the FTLE fields were sensitive to the differences in the strength of the tidal currents during spring and neap tides and that the FTLE fields were sensitive to the phases of the tide at the time of the particle release. However, there were five consistent features: 1) material lines through First Narrows connecting the Outer Harbour to the Inner Harbour; 2) material lines connecting First Narrows to the northern side of the Outer Harbour;

3) material lines separating the central part of the Outer Harbour from the southern shore of the Outer Harbour (including False Creek); 4) no material lines in the Inner Harbour connecting First and Second Narrows; and 5) no strong material lines in Second Narrow connecting the Inner and Central Harbours. The primary result of this study is that First Narrows tends to function as a transport corridor, whereas Second Narrows tends to function as a mixing element. These features will be used to interpret the oil spill simulations presented in Section 6.6 and Section 6.7.

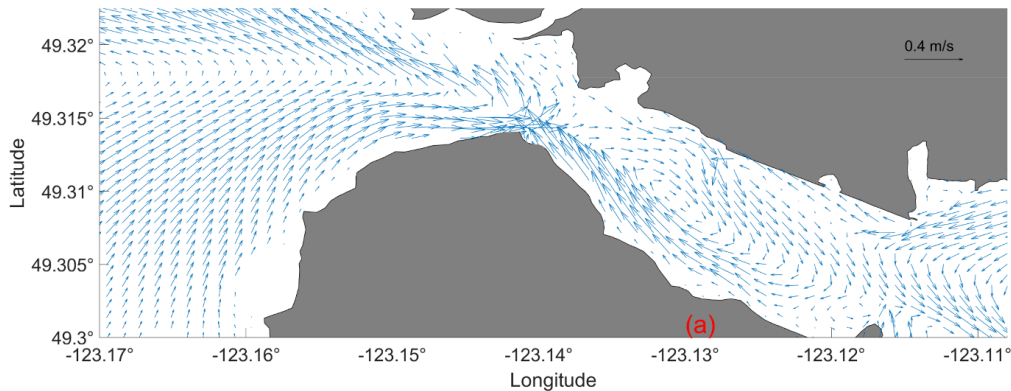
The sensitivity of the FTLE patterns to the overall strength of the currents (spring/neap cycle) and to the timing of the particle release (phase of the tide) indicates that when the asymmetric tidal currents interact with the physical structures, the dynamic structure in Burrard Inlet is affected. A metric of asymmetric tidal currents is the large residual current where the current is strong. Another metric is where the residual currents rapidly change over short distances. Also, the areas where the coastline and topography abruptly change are prime sites for asymmetric tidal currents. Figure 6.5 shows that residual eddies formed at the western end of First Narrows, in the Inner Harbour, and at each end of Second Narrows. Specifically, the incoming tides along the southern slope and the outgoing tide along the northern slope most likely caused the anti-cyclonic eddy at the western end of First Narrows [63,227]. The cyclonic eddy that covered almost the entire Inner Harbour was attributed to these features: the ebb tide jet from Second Narrows tending to stay on the north side; the tidal dipole propagating from First Narrows towards the southern side of the harbour on strong flood tides [63,251–253]; and the deep water in the center of the Inner Harbour. In addition, the residual

currents had small eddies in the southwest corner of the Inner Harbour. Therefore, we concluded that the complex topography led to the forming of asymmetric tidal currents, which influenced the transport and mixing in Burrard Inlet.

Water exchange between the Outer Harbour and the Central Harbour decreased in the Inner Harbour due to the tightly packed material lines during a spring tide (Figure 6.2) and the material lines across the harbour during neap tide (Figure 6.3b, 6.3c, 6.3d). The tidal excursion length explains how the FTLE fields formed in the Inner Harbour (Figure 6.6). The tidal excursion lengths for the neap tide had the same pattern as for the spring tide but had smaller magnitudes (not shown). The longest excursions were towards the east in the northeastern Outer Harbour (about 9 km, Figure 6.6a) and towards the west in Second Narrows and Central Harbour (around 10 km, Figure 6.6b). As mentioned in Section 5.4.2, the lengths of the Inner Harbour and the Central Harbour are about 8.8 and 7.8 km, respectively. Because the tidal excursion length (10 km) was shorter than the topographic scale (combined lengths of the two harbours are >17 km), it was difficult for the particles to move directly between the Outer Harbour and the Central Harbour. By comparison, the water exchange between the Outer Harbour and the Inner Harbour through First Narrows was relatively easy during spring tide and neap tide (Figures 6.2 and 6.3). The key to this easy exchange was that the tidal excursion in the northeastern Outer Harbour (Figure 6.6a) and the Inner Harbour (Figure 6.6b) was greater than the length of the First Narrows.

The spatial patterns of the tidal residual currents (Figure 6.5) and the tidal excursions (Figure 6.6) support the interpretation of the FTLE. The magnitudes of

the residual currents were largest in First Narrows and Second Narrows with the maximum residual currents ranging from about 0.37 to 0.43 m s⁻¹ compared to the typical value of ~0.1 m s⁻¹. In the Outer Harbour, there was a large area with mean eastward tidal excursions (flood tide; Figure 6.6a) ranging from 8 to 10 km (yellow). This large area represented water from the Outer Harbour transported into the Inner Harbour. There was also an area of a large eastward excursion (8 km) at the entrance to Second Narrows, and this large area represented water transporting through Second Narrows to the Central Harbour. For the westward excursions, the largest values (10 to 12 km, red; Figure 6.6b) were in Second Narrows and represented water that could not cross the Inner Harbour to exit First Narrows.



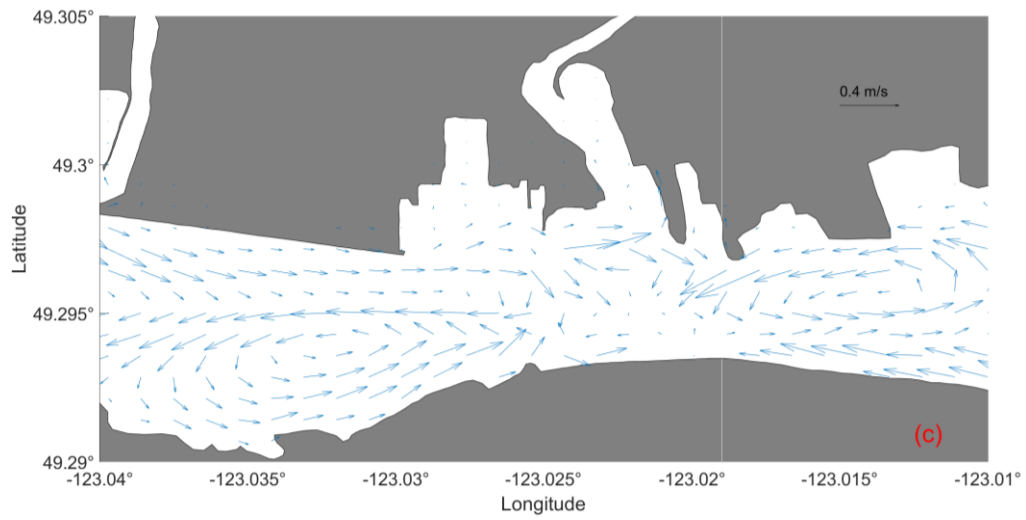
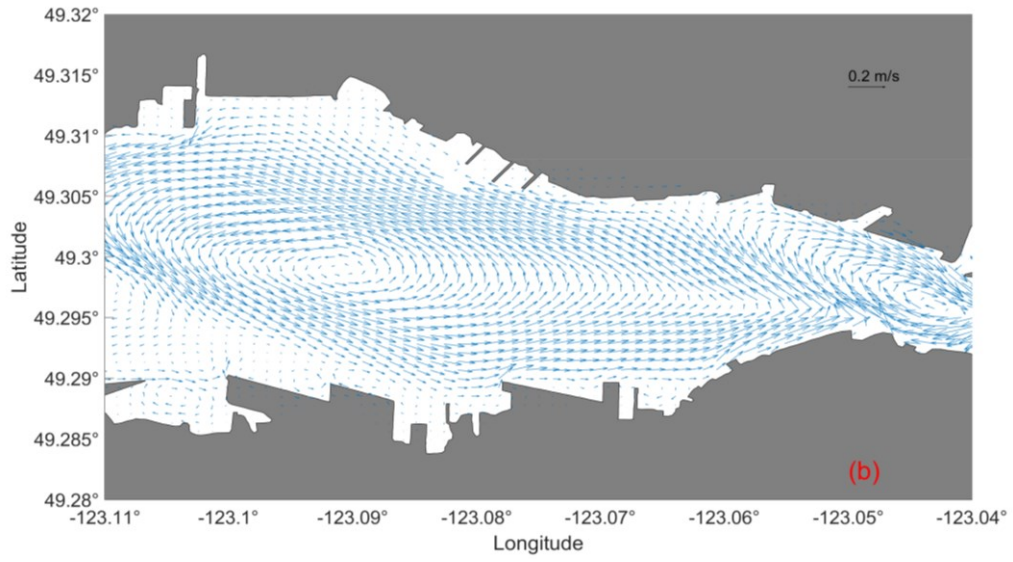


Figure 6.5 Residual current vectors for select locations within (a) First Narrows; the (b) Inner Harbour; and (c) Second Narrows

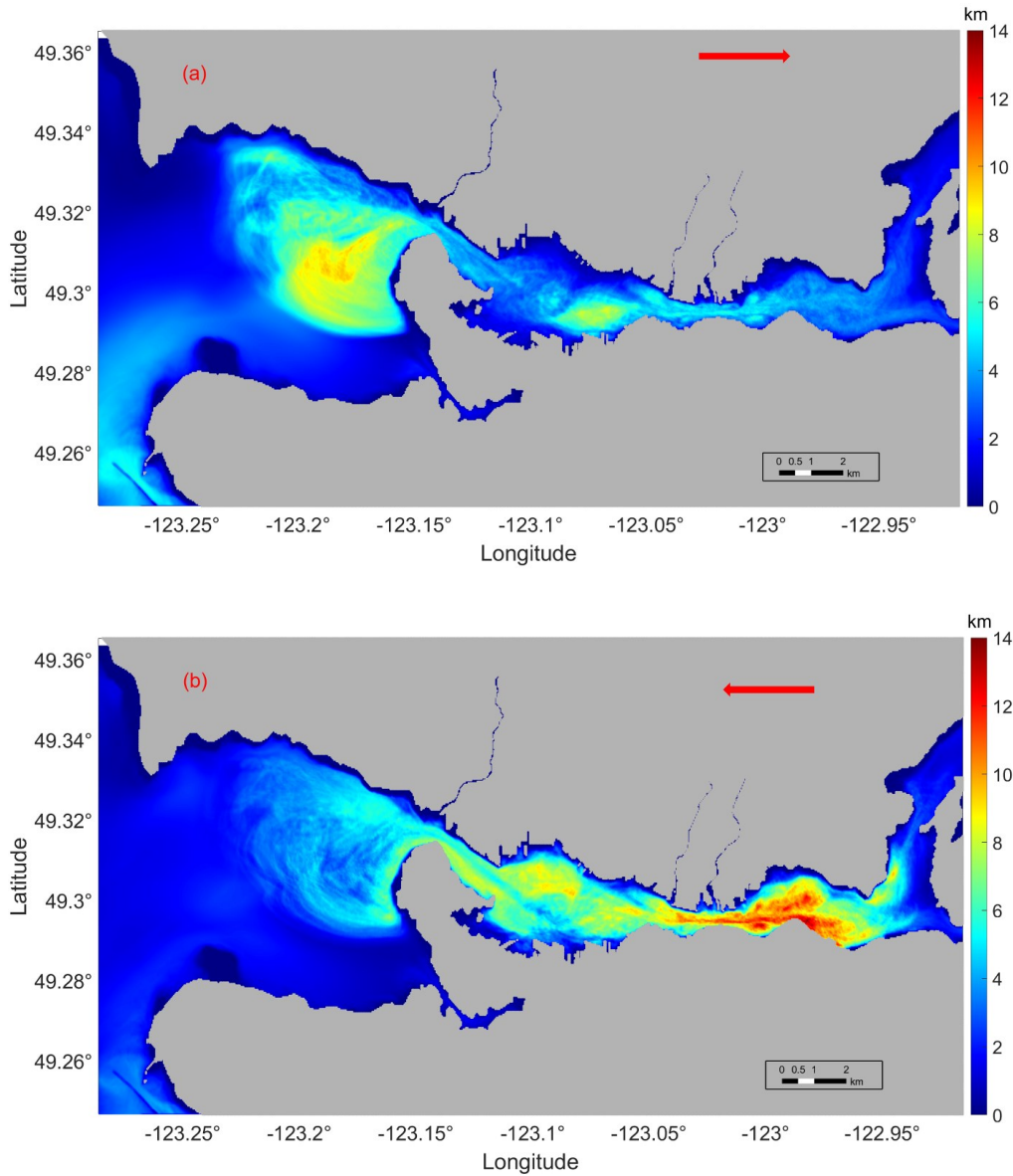


Figure 6.6 Mean tidal excursions (a) towards the east and (b) towards the west of the inlet.

6.6 The *M/V Marathassa* Oil Spill

As a busy port, PMV is at high risk for oil spills. On April 8, 2015, a small oil spill occurred in English Bay (Anchorage #12) with at least 2800 litres of oil

being released from the cargo vessel, *M/V Marathassa* [254]. The *M/V Marathassa* oil spill map in Figure 6.7 is adapted from Stormont (2015). The map in Figure 6.7 represents observations compiled from several sources, including the Shoreline Cleanup Assessment Technique (SCAT) [228,256], the National Aerial Surveillance Program (NASP) flights [254], and the City of Vancouver, BC [255]. Unfortunately, the exact time of the spill is unknown, but by studying the fate and trajectories of the spill, Zhong et al. (2018) found that the spill probably started between 14:00 and 15:00 (April 8, 2015). The tidal phase at the time was mid-ebb during the spring tide (NOAA's tides and currents website: <https://tidesandcurrents.noaa.gov/>). Therefore, the FTLE result for the mid-ebb tide during a spring tide (Figure 6.2d) is relevant.

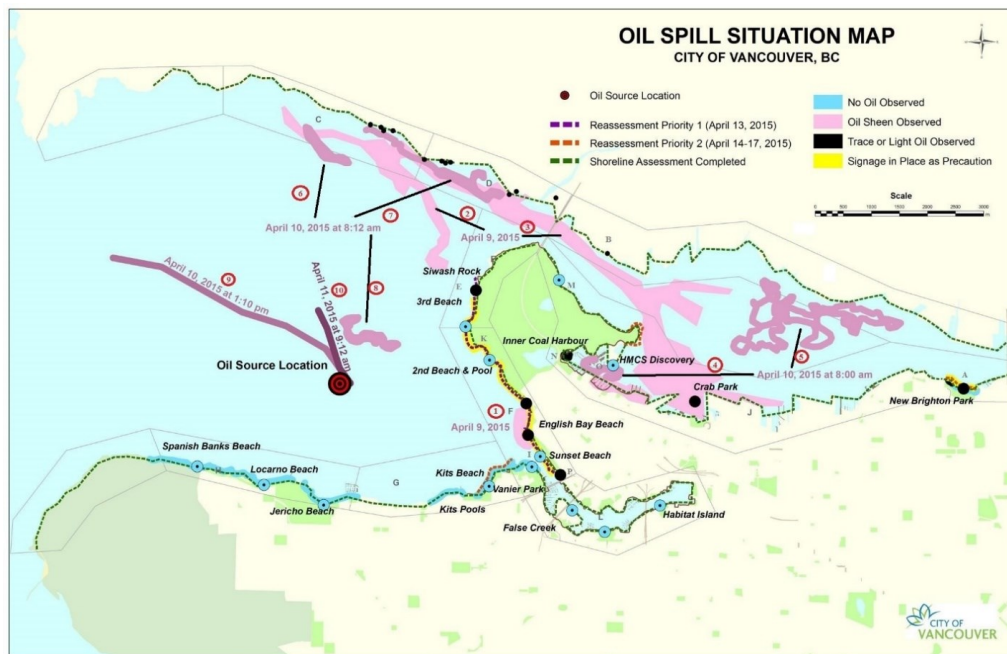


Figure 6.7 The *M/V Marathassa* oil spill situation map (Map provided by the City of Vancouver, BC and adapted from Stormont (2015)). This map shows the observed trajectory of the oil spill on the water surface and the contamination on

the shoreline in English Bay and the Inner Harbour from April 8 to April 10, 2015. Areas with oil sheen are numbered 1 to 10, and the contaminated shoreline areas are labelled A to P.

As shown in Figure 6.7, some of the oil beached at the eastern end of the Outer Harbour (English Bay Beach and near Siwash Rock), in the Inner Harbour, and along the northern shore of the Inner and Outer Harbours. The oil found on English Bay Beach and near Siwash Rock was consistent with the FTLE result that shows (red) material lines connecting the center of the Outer Harbour with the eastern end (Figure 6.2d). The oil observed in the Inner Harbour and along the north shore of First Narrows and the Outer Harbour was consistent with the clear blue material lines connecting the Outer Harbour to the Inner Harbour through First Narrows, with a branch extending northwest along the north shore of the Outer Harbour. Furthermore, some of the oil reached the north shore of the Outer Harbour and was transported into the Inner Harbour through First Narrows on April 9 and April 10, 2015, as evidenced by the FTLE results that have a clear blue material line along the First Narrows (Figure 6.2d). Furthermore, there was a red material line in the western part of First Narrows that extended towards the northwest and connected with the material line at the Outer Harbour's north shore, suggesting that this oil partially moved back to the Outer Harbour's north shore through First Narrows. Some of the oil in the Inner Harbour washed ashore on the southwest shore. A material line that connected to the southwest shoreline of the Inner Harbour was in the FTLE field (Figure 6.2d). It noted that no oil was observed on the shoreline of the southern Outer Harbour, which was consistent with the east-west orientation of the material lines that transported particles to the eastern end

and prevented transport to the south of shorelines. Overall, the FTLE results reasonably explained the trajectories of the *M/V Marathassa* spilled oil.

6.7 Stochastic Oil Spill Modelling

To verify the impact of tidal dispersion on particle transport, an oil spill case study was carried out. Six oil release sites were selected as shown in Figure 8.4: ANC-15, ANC-17, ANC-U, ANC-B, First Narrows, and Second Narrows. A stochastic approach was applied to conduct the spill modelling and hydrodynamic data from the FVCOM model were used. The total probability of oil contamination is in Figure 6.8. For the ANC-17, it was highly probable that the contaminant would move out of Burrard Inlet, with a small probability of crossing First Narrows into the Inner Harbour. When oil was released at First Narrows and in the Inner Harbour, the oil moved west to the Outer Harbour, but oil released at ANC-U and ANC-15 were likely to cross First Narrows and move towards the Inner Harbour, with a high probability of reaching the north shore of the Outer Harbour. Furthermore, the probability of the oil moving through Second Narrows was low in these five cases. These results agreed with the FTLE features mentioned in Section 6.5: 1) material lines through First Narrows connecting the Outer Harbour to the Inner Harbour; and 2) material lines connecting First Narrows to the northern side of the Outer Harbour. Moreover, the Second Narrows case showed little oil transporting through the First Narrows and into the Outer Harbour (Figure 6.8). This result is supported by the FTLE features: 4) no material lines in the Inner Harbour connecting First and Second Narrows; and 5) no strong material lines in Second Narrows connecting the Inner Harbour and Central Harbour.

The oil spill trajectory in the Outer Harbour was like a tail when oil was released at ANC-17, First Narrows, and ANC-U. It is also worth mentioning that there was no oil in False Creek. These were consistent with the FTLE feature: 3) material lines separating the central part of the Outer Harbour from the southern shore of the Outer Harbour (including False Creek). Overall, the results show that complex transport patterns can result from simple tidal forcing due to the importance of tidal dispersion and from the FTLE fields explaining the oil distribution in the model simulations.

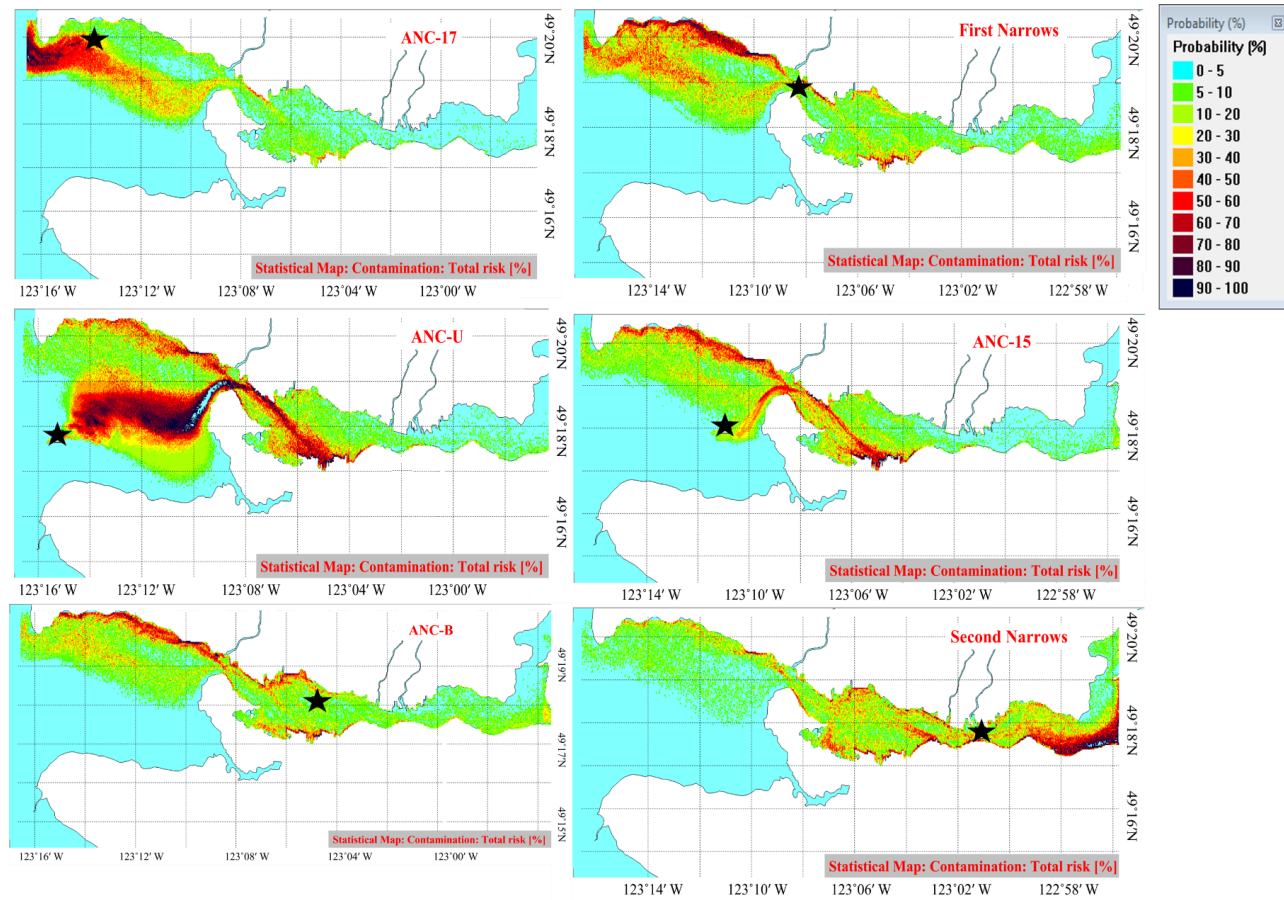


Figure 6.8 The total probability of oil contamination for an oil spill at ANC-17, First Narrows, ANC-U, ANC-15, ANC-B, and Second Narrows. Oil released at the black stars.

6.8 Summary

This study combined FTLE values, residual currents, and tidal excursion length to explore the influence of tidal dispersion on oil spill transport in Burrard Inlet. The FTLE results showed that the spatial structures of the FTLE fields were sensitive to the differences in the strength of the tidal currents during spring and neap tides, and the FTLE fields were sensitive to the phases of the tide at the time of the particle release. However, there were five consistent features: 1) material lines through First Narrows connecting the Outer Harbour to the Inner Harbour; 2) material lines connecting First Narrows to the northern side of the Outer Harbour; 3) material lines separating the central part of the Outer Harbour from the southern shore of the Outer Harbour (including False Creek); 4) no material lines in the Inner Harbour connecting First and Second Narrows; and 5) no strong material lines in Second Narrows connecting the Inner and Central Harbour. These features were consistency with the residual currents and tidal excursion analysis. Moreover, particles adhered to the eastern shore of English Bay during spring tide because most material lines in the Outer Harbour connected to the eastern shore.

To verify the tidal dispersion's impact on the transport of spilled oil, FTLE fields were used to explain the fate of a real oil spill (*M/V Marathassa* oil spill) that occurred in Burrard Inlet in 2015, and proved that the FTLE fields could explain the trajectory of this spilled oil. Finally, a stochastic case study of an oil spill in Burrard Inlet was conducted. The results of the oil spill modelling agreed well with observations from the analysis of the FTLE fields. This agreement suggests that computing the FTLE is promising for predicting oil trajectories and contingency

planning for when an oil spill occurs. Overall, such a systematic exploration of tidal dispersion's influence on particle/oil spill trajectories is valuable in oil spill modelling and ocean protection.

Chapter 7: Conclusion

7.1 Summary and Conclusions

With the aim to systematically explore OMA formation, settling and transport, we firstly utilized Screening Design to investigate seven process variables' impact on OMA D_{50} , including temperature, time, salinity, clay type, agitation speed, oil/clay weight ratio, the absence/presence of dispersant. It was found that time exhibited the most profound influence on OMA D_{50} , followed by temperature and oil/clay ratio. Also, the influence of time heavily depended on the temperature and oil/clay ratio employed. Prolonging formation time to 8 h at a low temperature of 0 °C and 1:2 oil/clay ratio led to a greater OMA D_{50} (~50 μm). The feasibility of using machine learning algorithms for OMA D_{50} prediction was also evaluated. Three tree-based machine learning algorithms (RF, GBR and Adaboost) were assessed. Adaboost had the most satisfactory performance on predicting D_{50} , as evidenced by the high R^2 (0.97 for training and 0.74 for testing) and low RMSE values. In addition to D_{50} prediction, Adaboost was implemented to quantify the importance of each process variable, and the obtained results were in well agreement with that of statistical analysis from ANOVA analysis. The machine learning based prediction was then compared with the traditional collision-theory-based prediction by using the same dataset, which the former was favourable in terms of the prediction accuracy (R^2 of 0.74 vs. 0.62). An open-sourced mini application software that incorporated with Adaboost algorithm and can be easily installed in the user's computer was assembled to quickly predict the OMA D_{50} by

simply keying the formation process variables, even though more research efforts are still required to expand the dataset to train the model better for more accurate prediction.

Identifying significant factors and their interactions that influence OMA median size improves our understanding of the significant factors and the complex relationships between various factors in OMA formation. This knowledge is crucial for guiding future experiments investigating OMA formation. Machine learning algorithms offer a convenient and effective means of estimating OMA median size, with potential for predicting OMA size distribution through further exploration. By employing these efficient methods, oil spill response strategies can be optimized, and environmental damage can be minimized by enhancing the accuracy of oil spill fate and trajectory predictions.

Laboratory setups (a high-speed camera coupled with a magnifying lens) were then constructed to measure the OMA settling velocity. The settling velocity of observed OMA varied from 0.2 mm/s to 3 mm/s. How the process variables affected the OMA settling velocity was also investigated by Principal Component Analysis (PCA). It was found that the clay concentration in the water environment positively and strongly correlated with OMA settling velocity. However, the dispersant addition and water density increment led to the reduction in OMA settling velocity. We also employed machine learning algorithms (RF, GBR and Adaboost) to predict the OMA settling velocity. GBR exhibited the best prediction accuracy (testing R^2 of 0.614 and RMSE of 1.535) among the three tested algorithms. Compared to traditional empirical estimation (R^2 of 0.387), machine

learning prediction had a much higher prediction accuracy, implying its promising potential in OMA settling velocity prediction. The sensitivity analysis of OMA transport with different prediction accuracies of OMA settling velocity revealed that a lower prediction accuracy led to a wider (less concentrated) spread of OMA, which was attributed to the small size of OMA. A hypothetical case particle tracking of OMA in Burrard Inlet, Vancouver, showed that all OMA remained at the Outer Harbour when a highly predictive settling velocity model was employed. However, a portion of OMA could be transported into the Vancouver Harbour through the First Narrows, with some ended up on the shoreline of the southern Vancouver Harbour when a less accurate OMA settling velocity model was implemented, which once again suggested the importance of accurate settling velocity prediction for OMA trajectories. Such a comprehensive study on OMA settling will help to build a solid foundation to better understand and track the oil spill transport in marine environments.

Understanding the important factors and their impact on OMA settling velocity not only guides future research on OMA settling velocity but also aids in predicting the behavior and distribution of OMA in the water column. The convenience and efficiency of using machine learning algorithms for estimating OMA settling velocity contribute to the development of more accurate oil spill models. This ultimately empowers decision-makers to optimize oil spill response strategies and reduce the environmental impact of oil spills more effectively.

An emerging technique on tidal dispersion properties analysis and pollutant tracking, the FTLE method, was then used as an aid-in tool for oil spill modelling

in Burrard Inlet, Vancouver, one of the busiest water areas in Canada. The FTLE results showed that the spatial structures of the FTLE fields were sensitive to the differences in the strength of the tidal currents during spring and neap tides, and the FTLE fields were sensitive to the phases of the tide at the time of the particle release. However, there were five consistent features: 1) material lines through First Narrows connecting the Outer Harbour to the Inner Harbour; 2) material lines connecting First Narrows to the northern side of the Outer Harbour; 3) material lines separating the central part of the Outer Harbour from the southern shore of the Outer Harbour (including False Creek); 4) no material lines in the Inner Harbour connecting First and Second Narrows; and 5) no strong material lines in Second Narrows connecting the Inner and Central Harbour. These features were consistent with the tidal excursion and the residual currents analysis, providing crucial information for predicting pollutant transport in the region. Moreover, particles adhered to the eastern shore of English Bay during spring tide because most material lines in the Outer Harbour connected to the eastern shore. To verify the tidal dispersion's impact on the transport of spilled oil, FTLE fields were used to explain the fate of a real oil spill (*M/V Marathassa* oil spill) that occurred in Burrard Inlet in 2015, and proved that the FTLE fields could explain the trajectory of this spilled oil. Finally, a stochastic case study of an oil spill in Burrard Inlet was conducted. The results of the oil spill modelling agreed well with observations from the analysis of the FTLE fields. This agreement suggests that computing the FTLE is promising for predicting oil trajectories and contingency planning for when an oil spill occurs.

Moreover, as compared to traditional modelling approaches, calculating FTLE values does not require high data accuracy or interpolating the velocity field. In addition, FTLE analysis results are not sensitive to data errors. The FTLE analysis contributes to the mitigation of environmental consequences arising from oil spills and the optimization of resource allocation during response initiatives. For example, once an oil spill occurs in Burrard Inlet, by giving the initial spill location and tidal phase in Burrard Inlet, users can rapidly pinpoint transport barriers and discern areas of high sensitivity from the corresponding FTLE map. Then, optimal strategies to address oil spills, such as targeted containment, dispersion, or recovery efforts, can be rapidly implemented.

Overall, this study highlights the benefits of combining traditional experimental methods with advanced machine learning techniques to understand complex processes like OMA formation, settling, and transport. This interdisciplinary approach can inspire future research in environmental science and other fields to leverage the power of machine learning and other advanced computational tools for deeper insights. Moreover, this research has identified areas that need further exploration, such as expanding the dataset to improve the machine learning model's accuracy and investigating OMA size distribution predictions. By identifying these gaps, the study sets the stage for future research to build upon these findings and further enhance the prediction and understanding of OMA formation and transport. Furthermore, the successful application of the FTLE method in Burrard Inlet suggests its potential for use in other geographical areas with varying hydrodynamic conditions. Additionally, the method can potentially be

extended to track and model the dispersion of other pollutants in water bodies, contributing to the broader field of environmental management.

7.2 Future Work and Recommendations

1. Influential factors for OMA D_{50} have been identified through Screening Design, a more detailed study by Factorial Design to explore their influences on the OMA size distribution more explicitly is recommended. In addition, machine learning algorithms have been proven to be superior to traditional collision-theory-based prediction for D_{50} , which serves as an inspiring reference for future work on estimating the OMA size distribution *via* machine learning algorithms.

2. Although the OMA formation and settling have been investigated from different perspectives in this study, the OMA oil trapping efficiency was not explored. The fast and adequate quantification of trapped oil in OMA is of significant value, which will ease and speed up the OMA oil trapping efficiency study. Furthermore, the obtained oil trapping efficiency results can be combined with OMA settling velocity and subsequently incorporated into the OMA transport modelling. This allows the OMA trajectory tracking and provides information on how much and where the spilled oils are sunk to the bottom by forming OMA.

3. Most oil spill modelling software lacks an OMA formation and settling section, future works on incorporating these sections (based upon acquired OMA data and highly predictive models) into oil spill models are of importance to improve the software performances on tracking the fate and trajectory of the spilled oil.

4. Tree-based machine learning algorithms showed promising potential in OMA formation and settling prediction. However, the predictability of other types of machine learning algorithms (e.g., deep learning and neural network) for OMA formation and settling need to be evaluated, and further predictability improvement might be possible. Also, the LCS line extraction from the FTLE field is still challenging. Therefore, using machine learning algorithms to extract the LCS lines more efficiently and accurately are also recommended.

5. Although FTLE is a promising aid-in tool for analyzing the trajectory of spilled oil, the current FTLE analysis was only two-dimensional (2D). However, the fate and behaviour of oil spills are usually three-dimensional (3D). Therefore, there is a strong necessity to develop the 3D FTLE technique.

References

- [1] A.K. Mishra, G.S. Kumar, Weathering of Oil Spill: Modeling and Analysis, *Aquatic Procedia*. 4 (2015) 435–442. <https://doi.org/10.1016/j.aqpro.2015.02.058>.
- [2] ITOPF, Oil Tanker Spill Statistics 2021, International Tanker Owners Pollution Federation (ITOPF), 2022. https://www.itopf.org/fileadmin/uploads/itopf/data/Documents/Company_Lit/Oil_Spill_Stats_2021.pdf.
- [3] M. Fingas, *Oil Spill Science and Technology*, Gulf Professional Publishing, 2016.
- [4] A.Y. Ivanov, V.V. Zatyagalova, A GIS approach to mapping oil spills in a marine environment, *International Journal of Remote Sensing*. 29 (2008) 6297–6313. <https://doi.org/10.1080/01431160802175587>.
- [5] P. Keramea, K. Spanoudaki, G. Zodiatis, G. Gikas, G. Sylaios, Oil Spill Modeling: A Critical Review on Current Trends, Perspectives, and Challenges, *Journal of Marine Science and Engineering*. 9 (2021) 181. <https://doi.org/10.3390/jmse9020181>.
- [6] M.L. Spaulding, State of the art review and future directions in oil spill modeling, *Marine Pollution Bulletin*. 115 (2017) 7–19. <https://doi.org/10.1016/j.marpolbul.2017.01.001>.
- [7] C.A. Page, J.S. Bonner, P.L. Sumner, T.J. McDonald, R.L. Autenrieth, C.B. Fuller, Behavior of a chemically-dispersed oil and a whole oil on a near-shore environment, *Water Research*. 34 (2000) 2507–2516. [https://doi.org/10.1016/S0043-1354\(99\)00398-X](https://doi.org/10.1016/S0043-1354(99)00398-X).
- [8] Sterling Michael C., J.S. Bonner, C.A. Page, C.B. Fuller, A.N.S. Ernest, R.L. Autenrieth, Partitioning of Crude Oil Polycyclic Aromatic Hydrocarbons in Aquatic Systems, *Environ. Sci. Technol.* 37 (2003) 4429–4434. <https://doi.org/10.1021/es0341034>.
- [9] D.K. Button, The influence of clay and bacteria on the concentration of dissolved hydrocarbon in saline solution, *Geochimica et Cosmochimica Acta*. 40 (1976) 435–440. [https://doi.org/10.1016/0016-7037\(76\)90008-9](https://doi.org/10.1016/0016-7037(76)90008-9).
- [10] X. Chao, Shankar N. Jothi, Wang Sam S. Y., Development and Application of Oil Spill Model for Singapore Coastal Waters, *Journal of Hydraulic Engineering*. 129 (2003) 495–503. [https://doi.org/10.1061/\(ASCE\)0733-9429\(2003\)129:7\(495\)](https://doi.org/10.1061/(ASCE)0733-9429(2003)129:7(495)).

- [11] P.A. Meyers, T.G. Oas, Comparison of associations of different hydrocarbons with clay particles in simulated seawater, *Environ. Sci. Technol.* 12 (1978) 934–937. <https://doi.org/10.1021/es60144a005>.
- [12] Z. Wang, W. Yang, Y. Zhang, Z. Yan, H. Liu, B. Sun, A practical adsorption model for the formation of submerged oils under the effect of suspended sediments, *RSC Advances.* 9 (2019) 15785–15790. <https://doi.org/10.1039/C9RA02775K>.
- [13] J.R. Payne, B.E. Kirstein, J.R. Clayton, C. Clary, R. Redding, Integration of suspended-particulate matter and oil-transportation study. Final report, September 1984–September 1987, Science Applications International Corp., San Diego, CA (USA), 1987. <https://www.osti.gov/biblio/5818912> (accessed January 11, 2020).
- [14] M.C. Sterling, J.S. Bonner, A.N.S. Ernest, C.A. Page, R.L. Autenrieth, Application of fractal flocculation and vertical transport model to aquatic sol–sediment systems, *Water Research.* 39 (2005) 1818–1830. <https://doi.org/10.1016/j.watres.2005.02.007>.
- [15] Sterling Michael C., J.S. Bonner, C.A. Page, C.B. Fuller, A.N.S. Ernest, R.L. Autenrieth, Modeling Crude Oil Droplet–Sediment Aggregation in Nearshore Waters, *Environ. Sci. Technol.* 38 (2004) 4627–4634. <https://doi.org/10.1021/es035467z>.
- [16] A.H. Walker, C. Stern, D. Scholz, E. Nielsen, F. Csulak, R. Gaudiosi, Consensus Ecological Risk Assessment of Potential Transportation-related Bakken and Dilbit Crude Oil Spills in the Delaware Bay Watershed, USA, *Journal of Marine Science and Engineering.* 4 (2016) 23.
- [17] O.A. Poirier, G.A. Thiel, Deposition of Free Oil by Sediments Settling in Sea Water, *AAPG Bulletin.* 25 (1941) 2170–2180.
- [18] J.R. Bragg, S.H. Yang, J.C. Roffall, Experimental studies of natural cleansing of oil residue from rocks in Prince William Sound by wave/tidal action: Unpublished Report, Exxon Production Research Co., PO Box. 2189 (1990).
- [19] H.O. Jahns, J.R. Bragg, L.C. Dash, E.H. Owens, Natural Cleaning of Shorelines Following the Exxon Valdez Spill, *International Oil Spill Conference Proceedings.* 1991 (1991) 167–176. <https://doi.org/10.7901/2169-3358-1991-1-167>.
- [20] J.R. Bragg, E.H. Owens, Shoreline Cleansing By Interactions Between Oil and Fine Mineral Particles, in: *International Oil Spill Conference Proceedings,* 1995: pp. 219–227. <https://www.ioscproceedings.org/doi/abs/10.7901/2169-3358-1995-1-219> (accessed January 21, 2020).

- [21] J.R. Bragg, S.H. Yang, Clay Oil Flocculation and its Role in Natural Cleansing in Prince William Sound Following the Exxon Valdez Oil Spill, in: United States, 1995. https://www-astm-org.ezproxy.library.dal.ca/DIGITAL_LIBRARY/STP/PAGES/STP19864S.htm (accessed January 21, 2020).
- [22] K. Lee, Oil-Particle Interactions in Aquatic Environments: Influence on the Transport, Fate, Effect and Remediation of Oil Spills, *Spill Science & Technology Bulletin*. 8 (2002) 3–8. [https://doi.org/10.1016/S1353-2561\(03\)00006-9](https://doi.org/10.1016/S1353-2561(03)00006-9).
- [23] K. Lee, P. Stoffyn-Egli, P.A. Wood, T. Lunel, Formation and structure of oil-mineral fines aggregates in coastal environments, (1998). <https://www.osti.gov/etdeweb/biblio/633775> (accessed October 29, 2021).
- [24] R.H. Dollhopf, F.A. Fitzpatrick, J.W. Kimble¹, D.M. Capone, T.P. Graan, R.B. Zelt, R. Johnson, Response to Heavy, Non-Floating Oil Spilled in a Great Lakes River Environment: A Multiple-Lines-Of-Evidence Approach for Submerged Oil Assessment and Recovery, *International Oil Spill Conference Proceedings*. 2014 (2014) 434–448. <https://doi.org/10.7901/2169-3358-2014.1.434>.
- [25] Y. Gong, X. Zhao, Z. Cai, S.E. O'Reilly, X. Hao, D. Zhao, A review of oil, dispersed oil and sediment interactions in the aquatic environment: Influence on the fate, transport and remediation of oil spills, *Marine Pollution Bulletin*. 79 (2014) 16–33. <https://doi.org/10.1016/j.marpolbul.2013.12.024>.
- [26] X. Zhong, H. Niu, P. Li, Y. Wu, L. Liu, An Overview of Oil-Mineral-Aggregate Formation, Settling, and Transport Processes in Marine Oil Spill Models, *Journal of Marine Science and Engineering*. 10 (2022) 610. <https://doi.org/10.3390/jmse10050610>.
- [27] A. Khelifa, P. Stoffyn-Egli, P.S. Hill, K. Lee, Characteristics of Oil Droplets Stabilized by Mineral Particles: The Effect of Salinity, *International Oil Spill Conference Proceedings*. 2003 (2003) 963–970. <https://doi.org/10.7901/2169-3358-2003-1-963>.
- [28] S. Le-Floch, J. Guyomarch, F.-X. Merlin, P. Stoffyn-Egli, J. Dixon, K. Lee, The Influence of Salinity on Oil-Mineral Aggregate Formation, *Spill Science & Technology Bulletin*. 8 (2002) 65–71. [https://doi.org/10.1016/S1353-2561\(02\)00124-X](https://doi.org/10.1016/S1353-2561(02)00124-X).
- [29] A. Khelifa, P. Stoffyn-Egli, P.S. Hill, K. Lee, Effects of salinity and clay type on oil-mineral aggregation, *Marine Environmental Research*. 59 (2005) 235–254. <https://doi.org/10.1016/j.marenvres.2004.05.003>.
- [30] D. Kerebel, Study of the influence of salinity on the flocculation oil-clay, Centre de Documentation de Recherche et d'expérimentations Sur Les

Pollutions Accidentelles Des Eaux (Cèdre). Final Report (in French), 20p & Annexes. (1997).

- [31] J. Guyomarch, F.-X. Merlin, P. Bernanose, Oil interaction with mineral fines and chemical dispersion: behaviour of the dispersed oil in coastal or estuarine conditions, in: ARCTIC AND MARINE OILSPILL PROGRAM TECHNICAL SEMINAR, MINISTRY OF SUPPLY AND SERVICES, CANADA, 1999: pp. 137–150.
- [32] J. Sun, A. Khelifa, X. Zheng, Z. Wang, L.L. So, S. Wong, C. Yang, B. Fieldhouse, A laboratory study on the kinetics of the formation of oil-suspended particulate matter aggregates using the NIST-1941b sediment, *Marine Pollution Bulletin*. 60 (2010) 1701–1707. <https://doi.org/10.1016/j.marpolbul.2010.06.044>.
- [33] J. Guyomarch, S. Le Floch, F.-X. Merlin, Effect of Suspended Mineral Load, Water Salinity and Oil Type on the Size of Oil–Mineral Aggregates in the Presence of Chemical Dispersant, *Spill Science & Technology Bulletin*. 8 (2002) 95–100. [https://doi.org/10.1016/S1353-2561\(02\)00118-4](https://doi.org/10.1016/S1353-2561(02)00118-4).
- [34] A. Khelifa, P. Stoffyn-Egli, P.S. Hill, K. Lee, Characteristics of Oil Droplets Stabilized by Mineral Particles: Effects of Oil Type and Temperature, *Spill Science & Technology Bulletin*. 8 (2002) 19–30. [https://doi.org/10.1016/S1353-2561\(02\)00117-2](https://doi.org/10.1016/S1353-2561(02)00117-2).
- [35] N. Nazemzadeh, A.A. Malanca, R.F. Nielsen, K.V. Gernaey, M.P. Andersson, S.S. Mansouri, Integration of first-principle models and machine learning in a modeling framework: An application to flocculation, *Chemical Engineering Science*. 245 (2021) 116864. <https://doi.org/10.1016/j.ces.2021.116864>.
- [36] Y. Qin, H. Jia, W. Liu, N. Lu, H.H. Ngo, J. Wang, Application of in-situ micro laser transmission on real-time monitoring of flocculation process, *Journal of Water Process Engineering*. 51 (2023) 103364. <https://doi.org/10.1016/j.jwpe.2022.103364>.
- [37] Y.-K. Kim, K.-S. Na, Application of machine learning classification for structural brain MRI in mood disorders: Critical review from a clinical perspective, *Progress in Neuro-Psychopharmacology and Biological Psychiatry*. 80 (2018) 71–80. <https://doi.org/10.1016/j.pnpbp.2017.06.024>.
- [38] A.E. Maxwell, T.A. Warner, F. Fang, Implementation of machine-learning classification in remote sensing: an applied review, *International Journal of Remote Sensing*. 39 (2018) 2784–2817. <https://doi.org/10.1080/01431161.2018.1433343>.
- [39] Y. Cao, Q. Kang, B. Zhang, Z. Zhu, G. Dong, Q. Cai, K. Lee, B. Chen, Machine learning-aided causal inference for unraveling chemical dispersant

- and salinity effects on crude oil biodegradation, *Bioresource Technology*. 345 (2022) 126468. <https://doi.org/10.1016/j.biortech.2021.126468>.
- [40] L. Ye, A.J. Manning, T.-J. Hsu, Oil-mineral flocculation and settling velocity in saline water, *Water Research*. 173 (2020) 115569.
- [41] C.M. O’Laughlin, B.A. Law, V.S. Zions, T.L. King, B. Robinson, Y. Wu, Settling of dilbit-derived oil-mineral aggregates (OMAs) & transport parameters for oil spill modelling, *Marine Pollution Bulletin*. 124 (2017) 292–302. <https://doi.org/10.1016/j.marpolbul.2017.07.042>.
- [42] W.R. Geyer, R.P. Signell, A reassessment of the role of tidal dispersion in estuaries and bays, *Estuaries*. 15 (1992) 97–108. <https://doi.org/10.2307/1352684>.
- [43] U.S. Army Corps of Engineers, Coastal Engineering Manual - Part II, 2012.
- [44] A.J.F. Hoitink, Physics of coral reef systems in a shallow tidal embayment, Utrecht University Repository, 2003. <http://dspace.library.uu.nl/handle/1874/567> (accessed February 4, 2020).
- [45] S.K. Maity, R. Maiti, Tidal impact leading to sedimentation at lower reach of Rupnarayan River, West Bengal, India, *IJMS Vol.45(10)* [October 2016]. (2016). <http://nopr.niscair.res.in/handle/123456789/35730> (accessed February 4, 2020).
- [46] J.C. Ohlmann, M.J. Molemaker, B. Baschek, B. Holt, G. Marmorino, G. Smith, Drifter observations of submesoscale flow kinematics in the coastal ocean, *Geophysical Research Letters*. 44 (2017) 330–337. <https://doi.org/10.1002/2016GL071537>.
- [47] R. Pawlowicz, C. Hannah, A. Rosenberger, Lagrangian observations of estuarine residence times, dispersion, and trapping in the Salish Sea, *Estuarine, Coastal and Shelf Science*. 225 (2019) 106246. <https://doi.org/10.1016/j.ecss.2019.106246>.
- [48] R.F. Rhodes, Effect of Salinity on Current Velocities, US Corps of Engineers, Committees Tidal Hydraulics. 94 (1950).
- [49] R.P. Signell, B. Butman, Modeling tidal exchange and dispersion in Boston Harbor, *Journal of Geophysical Research: Oceans*. 97 (1992) 15591–15606. <https://doi.org/10.1029/92JC01429>.
- [50] D. Xu, H. Xue, A numerical study of horizontal dispersion in a macro tidal basin, *Ocean Dynamics*. 61 (2011) 623–637. <https://doi.org/10.1007/s10236-010-0371-6>.

- [51] Z.-G. Ji, *Hydrodynamics and water quality: modeling rivers, lakes, and estuaries*, John Wiley & Sons, 2017.
- [52] H.H. Savenije, *Salinity and Tides in Alluvial Estuaries*, Elsevier, 2006. https://books.google.ca/books?hl=en&lr=&id=7vC3LYKD7RIC&oi=fnd&pg=PR3&ots=6e9uoMsUU5&sig=g-hIKn68gJRI4EiYKN9993In2Jo&redir_esc=y#v=onepage&q&f=false (accessed February 5, 2020).
- [53] G.P. Schramkowski, H.M. Schuttelaars, H.E. de Swart, Non-linear channel-shoal dynamics in long tidal embayments, *Ocean Dynamics*. 54 (2004) 399–407. <https://doi.org/10.1007/s10236-003-0063-6>.
- [54] G.P. Schramkowski, H.M. Schuttelaars, H.E. de Swart, The effect of geometry and bottom friction on local bed forms in a tidal embayment, *Continental Shelf Research*. 22 (2002) 1821–1833. [https://doi.org/10.1016/S0278-4343\(02\)00040-7](https://doi.org/10.1016/S0278-4343(02)00040-7).
- [55] L.V. Lucas, J.R. Koseff, S.G. Monismith, J.E. Cloern, J.K. Thompson, Processes governing phytoplankton blooms in estuaries. II: The role of horizontal transport, *Marine Ecology Progress Series*. 187 (1999) 17–30. <https://doi.org/10.3354/meps187017>.
- [56] F.W.L. Kho, P.L. Law, S.H. Lai, Y.W. Oon, L.H. Ngu, H.S. Ting, Quantitative dam break analysis on a reservoir earth dam, *Int. J. Environ. Sci. Technol.* 6 (2009) 203–210. <https://doi.org/10.1007/BF03327623>.
- [57] A. Hibma, H.J. de Vriend, M.J.F. Stive, Numerical modelling of shoal pattern formation in well-mixed elongated estuaries, *Estuarine, Coastal and Shelf Science*. 57 (2003) 981–991. [https://doi.org/10.1016/S0272-7714\(03\)00004-0](https://doi.org/10.1016/S0272-7714(03)00004-0).
- [58] M.J. Barrett, Predicting the effect of pollution in estuaries, *Proc. R. Soc. Lond. B*. 180 (1972) 511–520. <https://doi.org/10.1098/rspb.1972.0035>.
- [59] A. Valle-Levinson, Some basic hydrodynamic concepts to be considered for coastal aquaculture, in: *Site Selection and Carrying Capacities for Inland and Coastal Aquaculture*, 2013: p. 147.
- [60] B. De Young, S. Pond, The internal tide and resonance in Indian Arm, British Columbia, *Journal of Geophysical Research: Oceans*. 92 (1987) 5191–5207. <https://doi.org/10.1029/JC092iC05p05191>.
- [61] M.W. Stacey, R. Pieters, S. Pond, The Simulation of Deep Water Exchange in a Fjord: Indian Arm, British Columbia, Canada, *J. Phys. Oceanogr.* 32 (2002) 2753–2765. [https://doi.org/10.1175/1520-0485\(2002\)032<2753:TSODWE>2.0.CO;2](https://doi.org/10.1175/1520-0485(2002)032<2753:TSODWE>2.0.CO;2).

- [62] M.W. Stacey, S. Pond, Dependence of Currents and Density on the Spring–Neap Cycle and the Diurnal Inequality in Burrard Inlet, British Columbia: Simulations and Observations, *J. Phys. Oceanogr.* 33 (2003) 2366–2374. [https://doi.org/10.1175/1520-0485\(2003\)033<2366:DOCADO>2.0.CO;2](https://doi.org/10.1175/1520-0485(2003)033<2366:DOCADO>2.0.CO;2).
- [63] Y. Wu, C. Hannah, M. O’Flaherty-Sproul, P. MacAulay, S. Shan, A modeling study on tides in the Port of Vancouver, *Coastal Environmental Changes under Increasing Anthropogenic Impacts.* 2 (2019) 101–125. <https://doi.org/10.1139/anc-2018-0008@anc-cec.issue01>.
- [64] I. Mezić, S. Loire, V.A. Fonoberov, P. Hogan, A new mixing diagnostic and Gulf oil spill movement, *Science.* 330 (2010) 486–489.
- [65] M. Fingas, Chapter 8 - Introduction to Spill Modeling, in: M. Fingas (Ed.), *Oil Spill Science and Technology*, Gulf Professional Publishing, Boston, 2011: pp. 187–200. <https://doi.org/10.1016/B978-1-85617-943-0.10008-5>.
- [66] K. Lee, M. Boufadel, B. Chen, J. Foght, P. Hodson, S. Swanson, A. Venosa, *Expert Panel Report on the Behaviour and Environmental Impacts of Crude Oil Released into Aqueous Environments*, Royal Society of Canada, Ottawa, 2015.
- [67] T.K. Dutta, S. Harayama, Fate of Crude Oil by the Combination of Photooxidation and Biodegradation, *Environ. Sci. Technol.* 34 (2000) 1500–1505. <https://doi.org/10.1021/es991063o>.
- [68] M. Fingas, The evaporation of oil spills, in: *ARCTIC AND MARINE OILSPILL PROGRAM TECHNICAL SEMINAR, MINISTRY OF SUPPLY AND SERVICES, CANADA*, 1995: pp. 43–60.
- [69] M. Fingas, Chapter 10 - Models for Water-in-Oil Emulsion Formation, in: M. Fingas (Ed.), *Oil Spill Science and Technology*, Gulf Professional Publishing, Boston, 2011: pp. 243–273. <https://doi.org/10.1016/B978-1-85617-943-0.10010-3>.
- [70] J.A. Fay, The Spread of Oil Slicks on a Calm Sea, in: D.P. Hoult (Ed.), *Oil on the Sea: Proceedings of a Symposium on the Scientific and Engineering Aspects of Oil Pollution of the Sea, Sponsored by Massachusetts Institute of Technology and Woods Hole Oceanographic Institution and Held at Cambridge, Massachusetts, May 16, 1969*, Springer US, Boston, MA, 1969: pp. 53–63. https://doi.org/10.1007/978-1-4684-9019-0_5.
- [71] W.A. Dew, A. Hontela, S.B. Rood, G.G. Pyle, Biological effects and toxicity of diluted bitumen and its constituents in freshwater systems, *Journal of Applied Toxicology.* 35 (2015) 1219–1227.
- [72] W.J. Lehr, Review of modeling procedures for oil spill weathering behavior, *Advances in Ecological Sciences.* 9 (2001) 51–90.

- [73] S.-D. Wang, Y.-M. Shen, Y.-K. Guo, J. Tang, Three-dimensional numerical simulation for transport of oil spills in seas, *Ocean Engineering*. 35 (2008) 503–510.
- [74] J. Michel, N. Rutherford, Impacts, recovery rates, and treatment options for spilled oil in marshes, *Marine Pollution Bulletin*. 82 (2014) 19–25. <https://doi.org/10.1016/j.marpolbul.2014.03.030>.
- [75] W. Lehr, R. Jones, M. Evans, D. Simecek-Beatty, R. Overstreet, Revisions of the ADIOS oil spill model, *Environmental Modelling & Software*. 17 (2002) 189–197. [https://doi.org/10.1016/S1364-8152\(01\)00064-0](https://doi.org/10.1016/S1364-8152(01)00064-0).
- [76] W.J. Lehr, R. Overstreet, R. Jones, G. Watabayashi, ADIOS-automated data inquiry for oil spills, (1992). http://inis.iaea.org/Search/search.aspx?orig_q=RN:25009588 (accessed November 23, 2018).
- [77] P.S. Daling, O.M. Aamo, A. Lewis, T. Strøm-Kristiansen, Sintef/iku oil-weathering model: predicting oils' properties at sea, *International Oil Spill Conference Proceedings*. 1997 (1997) 297–307. <https://doi.org/10.7901/2169-3358-1997-1-297>.
- [78] M. Reed, P. Daling, A. Lewis, M.K. Ditlevsen, B. Brørs, J. Clark, D. Aurand, Modelling of dispersant application to oil spills in shallow coastal waters, *Environmental Modelling & Software*. 19 (2004) 681–690. <https://doi.org/10.1016/j.envsoft.2003.08.014>.
- [79] D. Mackay, I. Buist, R. Mascarenhas, S. Paterson, Oil spill processes and models, Environment Canada Manuscript Report No. EE-8, Ottawa, Ontario. (1980).
- [80] D. Mackay, S. Paterson, K. Trudel, A mathematical model of oil spill behaviour, Environment Canada, Environmental Protection Service, Environmental Impact Control Directorate, Environmental Emergency Branch, Research and Development Division, 1980.
- [81] O.M. Aamo, M. Reed, P.S. Daling, A laboratory-based weathering model: PC version for coupling to transport models, (1993). http://inis.iaea.org/Search/search.aspx?orig_q=RN:25063976 (accessed November 23, 2018).
- [82] P. Li, H. Niu, S. Li, T.L. King, S. Zou, X. Chen, Z. Lu, DBWM: A Diluted Bitumen Weathering Model, *Marine Pollution Bulletin*. (2022) Accepted.
- [83] M. Reed, Ø. Johansen, P.J. Brandvik, P. Daling, A. Lewis, R. Fiocco, D. Mackay, R. Prentki, Oil Spill Modeling towards the Close of the 20th Century: Overview of the State of the Art, *Spill Science & Technology Bulletin*. 5 (1999) 3–16. [https://doi.org/10.1016/S1353-2561\(98\)00029-2](https://doi.org/10.1016/S1353-2561(98)00029-2).

- [84] American Society of Civil Engineers (ASCE), State-of-the-Art Review of Modeling Transport and Fate of Oil Spills, *Journal of Hydraulic Engineering*. 122 (1996) 594–609. [https://doi.org/10.1061/\(ASCE\)0733-9429\(1996\)122:11\(594\)](https://doi.org/10.1061/(ASCE)0733-9429(1996)122:11(594)).
- [85] G. Marcotte, P. Bourgoïn, G. Mercier, J.P. Gauthier, P. Pellerin, G. Smith, C.W. Brown, Canadian oil spill modelling suite: An overview., in: Halifax, NS, Canada, 2016: pp. 1026–1034.
- [86] Tetra Tech., SPILLCALC Oil and Contaminant Spill Model, (n.d.). <http://www.tetratech.com/en/projects/spillcalc-oil-and-contaminant-spill-model> (accessed September 10, 2018).
- [87] M. Reed, E. Gundlach, T. Kana, A coastal zone oil spill model: Development and sensitivity studies, *Oil and Chemical Pollution*. 5 (1989) 411–449. [https://doi.org/10.1016/S0269-8579\(89\)80019-X](https://doi.org/10.1016/S0269-8579(89)80019-X).
- [88] NOAA, GNOME Suite for Oil Spill Modeling, Office of Response and Restoration. (2019). <https://response.restoration.noaa.gov/oil-and-chemical-spills/oil-spills/response-tools/gnome-suite-oil-spill-modeling.html> (accessed January 29, 2022).
- [89] A.H. Al-Rabeh, R.W. Lardner, N. Gunay, Gulfspill Version 2.0: a software package for oil spills in the Arabian Gulf, *Environmental Modelling & Software*. 15 (2000) 425–442. [https://doi.org/10.1016/S1364-8152\(00\)00013-X](https://doi.org/10.1016/S1364-8152(00)00013-X).
- [90] R. Lardner, G. Zodiatis, D. Hayes, N. Pinardi, Application of the MEDSLIK oil spill model to the Lebanese spill of July 2006, *European Group of Experts on Satellite Monitoring of Sea Based Oil Pollution, European Communities ISSN*. (2006) 1018–5593.
- [91] R.W. Lardner, G. Zodiatis, L. Loizides, A. Demetropoulos, An operational oil spill model for the Levantine Basin (Eastern Mediterranean Sea), (1999). http://inis.iaea.org/Search/search.aspx?orig_q=RN:30046843 (accessed November 23, 2018).
- [92] M. De Dominicis, N. Pinardi, G. Zodiatis, R. Archetti, MEDSLIK-II, a Lagrangian marine surface oil spill model for short-term forecasting – Part 2: Numerical simulations and validations, *Geoscientific Model Development*. 6 (2013) 1871–1888. <https://doi.org/10.5194/gmd-6-1871-2013>.
- [93] Danish Hydraulic Institute (DHI)., DHI Oil Spill Model - Scientific Description, (2017). http://manuals.mikepoweredbydhi.help/2017/General/DHI_OilSpill_Model.pdf.

- [94] P. Carracedo, S. Torres-López, M. Barreiro, P. Montero, C.F. Balseiro, E. Penabad, P.C. Leitaó, V. Pérez-Muñuzuri, Improvement of pollutant drift forecast system applied to the Prestige oil spills in Galicia Coast (NW of Spain): Development of an operational system, *Marine Pollution Bulletin*. 53 (2006) 350–360. <https://doi.org/10.1016/j.marpolbul.2005.11.014>.
- [95] P. Daniel, F. Marty, P. Josse, C. Skandrani, R. Benshila, Improvement of Drift Calculation in Mothy Operational Oil Spill Prediction System, *International Oil Spill Conference Proceedings*. 2003 (2003) 1067–1072. <https://doi.org/10.7901/2169-3358-2003-1-1067>.
- [96] M.L. Spaulding, V.S. Kolluru, E. Anderson, E. Howlett, Application of three-dimensional oil spill model (WOSM/OILMAP) to Hindcast the Braer spill, *Spill Science & Technology Bulletin*. 1 (1994) 23–35. [https://doi.org/10.1016/1353-2561\(94\)90005-1](https://doi.org/10.1016/1353-2561(94)90005-1).
- [97] M.C. Garcia, M.A. Sanz-Bobi, J. del Pico, SIMAP: Intelligent System for Predictive Maintenance: Application to the health condition monitoring of a windturbine gearbox, *Computers in Industry*. 57 (2006) 552–568. <https://doi.org/10.1016/j.compind.2006.02.011>.
- [98] A. Berry, T. Dabrowski, K. Lyons, The oil spill model OILTRANS and its application to the Celtic Sea, *Marine Pollution Bulletin*. 64 (2012) 2489–2501. <https://doi.org/10.1016/j.marpolbul.2012.07.036>.
- [99] K.-F. Dagestad, J. Röhrs, Ø. Breivik, B. Ådlandsvik, OpenDrift v1.0: a generic framework for trajectory modelling, *Geoscientific Model Development*. 11 (2018) 1405–1420. <https://doi.org/10.5194/gmd-11-1405-2018>.
- [100] J. Röhrs, K.-F. Dagestad, H. Asbjørnsen, T. Nordam, J. Skancke, C.E. Jones, C. Brekke, The effect of vertical mixing on the horizontal drift of oil spills, *Ocean Science*. 14 (2018) 1581–1601. <https://doi.org/10.5194/os-14-1581-2018>.
- [101] M. Reed, O.M. Aamo, P.S. Daling, Quantitative analysis of alternate oil spill response strategies using OSCAR, *Spill Science & Technology Bulletin*. 2 (1995) 67–74. [https://doi.org/10.1016/1353-2561\(95\)00020-5](https://doi.org/10.1016/1353-2561(95)00020-5).
- [102] P. Annika, T. George, P. George, N. Konstantinos, D. Costas, C. Koutitas, The Poseidon Operational Tool for the Prediction of Floating Pollutant Transport, *Marine Pollution Bulletin*. 43 (2001) 270–278. [https://doi.org/10.1016/S0025-326X\(01\)00080-7](https://doi.org/10.1016/S0025-326X(01)00080-7).
- [103] K. Nittis, L. Perivoliotis, G. Korres, C. Tziavos, I. Thanos, Operational monitoring and forecasting for marine environmental applications in the Aegean Sea, *Environmental Modelling & Software*. 21 (2006) 243–257. <https://doi.org/10.1016/j.envsoft.2004.04.023>.

- [104] C.H. Ainsworth, E.P. Chassignet, D. French-McCay, C.J. Beegle-Krause, I. Berenshtein, J. Englehardt, T. Fiddaman, H. Huang, M. Huettel, D. Justic, V.H. Kourafalou, Y. Liu, C. Mauritzen, S. Murawski, S. Morey, T. Özgökmen, C.B. Paris, J. Ruzicka, S. Saul, J. Shepherd, S. Socolofsky, H. Solo Gabriele, T. Sutton, R.H. Weisberg, C. Wilson, L. Zheng, Y. Zheng, Ten years of modeling the Deepwater Horizon oil spill, *Environmental Modelling & Software*. 142 (2021) 105070. <https://doi.org/10.1016/j.envsoft.2021.105070>.
- [105] L. Zhao, T. Nedwed, D. Mitchell, Review of the Science behind Oil Spill Fate Models: Are Updates Needed?, *International Oil Spill Conference Proceedings*. 2021 (2021) 687874. <https://doi.org/10.7901/2169-3358-2021.1.687874>.
- [106] S.A. Gustitus, T.P. Clement, Formation, Fate, and Impacts of Microscopic and Macroscopic Oil-Sediment Residues in Nearshore Marine Environments: A Critical Review, *Reviews of Geophysics*. 55 (2017) 1130–1157. <https://doi.org/10.1002/2017RG000572>.
- [107] P.A. Wood, T. Lunel, F. Daniel, R. Swannell, K. Lee, P. Stoffyn-Egli, Influence of oil and mineral characteristics on oil-mineral interaction, (1998). http://inis.iaea.org/Search/search.aspx?orig_q=RN:29050809 (accessed January 14, 2020).
- [108] H. Zhang, M. Khatibi, Y. Zheng, K. Lee, Z. Li, J.V. Mullin, Investigation of OMA formation and the effect of minerals, *Marine Pollution Bulletin*. 60 (2010) 1433–1441. <https://doi.org/10.1016/j.marpolbul.2010.05.014>.
- [109] W. Wang, Y. Zheng, Z. Li, K. Lee, PIV investigation of oil–mineral interaction for an oil spill application, *Chemical Engineering Journal*. 170 (2011) 241–249. <https://doi.org/10.1016/j.cej.2011.03.062>.
- [110] J.R. Payne, *Oil-ice Sediment Interactions During Freeze-up and Break-up*, US Department of Commerce, National Oceanic and Atmospheric Administration ..., 1989.
- [111] W. Ji, M. Boufadel, L. Zhao, B. Robinson, T. King, C. An, B. (Helen) Zhang, K. Lee, Formation of oil-particle aggregates: Impacts of mixing energy and duration, *Science of The Total Environment*. 795 (2021) 148781. <https://doi.org/10.1016/j.scitotenv.2021.148781>.
- [112] X. Ma, A. Cogswell, Z. Li, K. Lee, Particle size analysis of dispersed oil and oil-mineral aggregates with an automated ultraviolet epi-fluorescence microscopy system, *Environmental Technology*. 29 (2008) 739–748. <https://doi.org/10.1080/09593330801987111>.
- [113] J. Sun, A. Khelifa, C. Zhao, D. Zhao, Z. Wang, Laboratory investigation of oil–suspended particulate matter aggregation under different mixing

- conditions, *Science of The Total Environment*. 473–474 (2014) 742–749. <https://doi.org/10.1016/j.scitotenv.2013.12.078>.
- [114] K. Lee, Z. Li, T. King, P. Kepkay, M.C. Boufadel, A.D. Venosa, Wave Tank Studies on Formation and Transport of OMA from the Chemically Dispersed Oil, in: W.F. Davidson, K. Lee, A. Cogswell (Eds.), *Oil Spill Response: A Global Perspective*, Springer Netherlands, Dordrecht, 2008: pp. 159–177. https://doi.org/10.1007/978-1-4020-8565-9_20.
- [115] A. Khelifa, M. Fingas, C. Brown, Effects of dispersants on oil-SPM aggregation and fate in US coastal waters, Final Report Grant Number: NA04NOS4190063. (2008).
- [116] J. Fu, Y. Gong, X. Zhao, S.E. O'Reilly, D. Zhao, Effects of Oil and Dispersant on Formation of Marine Oil Snow and Transport of Oil Hydrocarbons, *Environ. Sci. Technol.* 48 (2014) 14392–14399. <https://doi.org/10.1021/es5042157>.
- [117] D.K. Muschenheim, K. Lee, Removal of Oil from the Sea Surface through Particulate Interactions: Review and Prospectus, *Spill Science & Technology Bulletin*. 8 (2002) 9–18. [https://doi.org/10.1016/S1353-2561\(02\)00129-9](https://doi.org/10.1016/S1353-2561(02)00129-9).
- [118] D.M. Waterman, M.H. Garcia, Laboratory tests of oil-particle interactions in a freshwater riverine environment with cold lake blend weathered bitumen, Ven Te Chow Hydrosystems Laboratory, University of Illinois. (2015).
- [119] U.C. Bandara, P.D. Yapa, H. Xie, Fate and transport of oil in sediment laden marine waters, *Journal of Hydro-Environment Research*. 5 (2011) 145–156. <https://doi.org/10.1016/j.jher.2011.03.002>.
- [120] A. Khelifa, K. Lee, P.S. Hill, Prediction of oil droplet size distribution in agitated aquatic environments, in: Canada, 2004. <https://www.osti.gov/etdeweb/biblio/20485447> (accessed January 14, 2020).
- [121] A. Khelifa, K. Lee, P.S. Hill, L.O. Ajijolaiya, Modelling the effect of sediment size on OMA formation, in: Canada, 2004. http://inis.iaea.org/Search/search.aspx?orig_q=RN:35072650 (accessed January 14, 2020).
- [122] L. Zhao, M.C. Boufadel, X. Geng, K. Lee, T. King, B. Robinson, F. Fitzpatrick, A-DROP: A predictive model for the formation of oil particle aggregates (OPAs), *Marine Pollution Bulletin*. 106 (2016) 245–259. <https://doi.org/10.1016/j.marpolbul.2016.02.057>.
- [123] M. v. Smoluchowski, Versuch einer mathematischen Theorie der Koagulationskinetik kolloider Lösungen, *Zeitschrift Für Physikalische Chemie*. 92U (1918) 129–168. <https://doi.org/10.1515/zpch-1918-9209>.

- [124] H.R. Pruppacher, J.D. Klett, *Microphysics of Clouds and Precipitation*, Springer Netherlands, 1980.
- [125] L. Cui, C.K. Harris, D.R.N. Tarpley, Formation of Oil-Particle-Aggregates: Numerical Model Formulation and Calibration, *Frontiers in Marine Science*. 8 (2021). <https://www.frontiersin.org/article/10.3389/fmars.2021.629476> (accessed January 19, 2022).
- [126] L. Jones, M.H. Garcia, Development of a Rapid Response Riverine Oil–Particle Aggregate Formation, Transport, and Fate Model, *Journal of Environmental Engineering*. 144 (2018) 04018125. [https://doi.org/10.1061/\(ASCE\)EE.1943-7870.0001470](https://doi.org/10.1061/(ASCE)EE.1943-7870.0001470).
- [127] A. Khelifa, P.S. Hill, K. Lee, Assessment of minimum sediment concentration for OMA formation using a Monte Carlo model, in: M. Al-Azab, W. El-Shorbagy (Eds.), *Developments in Earth and Environmental Sciences*, Elsevier, 2005: pp. 93–104. [https://doi.org/10.1016/S1571-9197\(05\)80031-X](https://doi.org/10.1016/S1571-9197(05)80031-X).
- [128] P.S. Hill, A. Khelifa, K. Lee, Time Scale for Oil Droplet Stabilization by Mineral Particles in Turbulent Suspensions, *Spill Science & Technology Bulletin*. 8 (2002) 73–81. [https://doi.org/10.1016/S1353-2561\(03\)00008-2](https://doi.org/10.1016/S1353-2561(03)00008-2).
- [129] Z. Wang, W. Yang, Y. Zhang, Z. Yan, H. Liu, B. Sun, A practical adsorption model for the formation of submerged oils under the effect of suspended sediments, *RSC Advances*. 9 (2019) 15785–15790. <https://doi.org/10.1039/C9RA02775K>.
- [130] L.O. Ajijolaiya, P.S. Hill, A. Khelifa, R.M. Islam, K. Lee, Laboratory investigation of the effects of mineral size and concentration on the formation of oil–mineral aggregates, *Marine Pollution Bulletin*. 52 (2006) 920–927. <https://doi.org/10.1016/j.marpolbul.2005.12.006>.
- [131] Z. Wang, Z. Yanqiu, Y. Zhiyu, S. Bing, L. Hui, Adsorption model of oil droplets interacting with suspended particulate materials in marine coastal environments, *Continental Shelf Research*. 173 (2019) 87–92. <https://doi.org/10.1016/j.csr.2018.12.010>.
- [132] Y. Wu, C. Hannah, B. Law, T. King, B. Robinson, An estimate of the sinking rate of spilled diluted bitumen in sediment-laden coastal waters, in: *Proceedings of the 39th AMOP Technical Seminar, Environment and Climate Change Canada, Ottawa, ON, Canada, 2016*: pp. 331–347.
- [133] A.N. Ernest, J.S. Bonner, R.L. Autenrieth, Determination of Particle Collision Efficiencies for Flocculent Transport Models, *Journal of Environmental Engineering*. 121 (1995) 320–329. [https://doi.org/10.1061/\(ASCE\)0733-9372\(1995\)121:4\(320\)](https://doi.org/10.1061/(ASCE)0733-9372(1995)121:4(320)).

- [134] H. Niu, Z. Li, K. Lee, P. Kepkay, J.V. Mullin, Modelling the Transport of Oil–Mineral-Aggregates (OMAs) in the Marine Environment and Assessment of Their Potential Risks, *Environ Model Assess.* 16 (2011) 61–75. <https://doi.org/10.1007/s10666-010-9228-0>.
- [135] H. Niu, K. Lee, Study of the dispersion/settling of oil-mineral-aggregates using particle tracking model and assessment of their potential risks, *International Journal of Environment and Pollution.* 52 (2013) 32–51. <https://doi.org/10.1504/IJEP.2013.056356>.
- [136] B. Ouartassi, B. Doyon, M. Heniche, Numerical Prediction of Oil Mineral Aggregates Dispersion in the Estuary Of ST-Lawrence River, *J. Phys.: Conf. Ser.* 1743 (2021) 012033. <https://doi.org/10.1088/1742-6596/1743/1/012033>.
- [137] Z. Zhu, D.M. Waterman, M.H. Garcia, Modeling the transport of oil–particle aggregates resulting from an oil spill in a freshwater environment, *Environ Fluid Mech.* 18 (2018) 967–984. <https://doi.org/10.1007/s10652-018-9581-0>.
- [138] J.C. Winterwerp, A simple model for turbulence induced flocculation of cohesive sediment, *Journal of Hydraulic Research.* 36 (1998) 309–326. <https://doi.org/10.1080/00221689809498621>.
- [139] Y. Li, Q. Yu, S. Gao, B.W. Flemming, Settling velocity and drag coefficient of platy shell fragments, *Sedimentology.* 67 (2020) 2095–2110. <https://doi.org/10.1111/sed.12696>.
- [140] L. Zhao, M.C. Boufadel, E. Adams, S.A. Socolofsky, T. King, K. Lee, T. Nedwed, Simulation of scenarios of oil droplet formation from the Deepwater Horizon blowout, *Marine Pollution Bulletin.* 101 (2015) 304–319. <https://doi.org/10.1016/j.marpolbul.2015.10.068>.
- [141] H. Niu, Z. Li, K. Lee, P. Kepkay, J. Mullin, A Method for Assessing Environmental Risks of Oil-Mineral-Aggregate to Benthic Organisms, *Human and Ecological Risk Assessment: An International Journal.* 16 (2010) 762–782. <https://doi.org/10.1080/10807039.2010.501240>.
- [142] E.N. Lorenz, Deterministic Nonperiodic Flow, *J. Atmos. Sci.* 20 (1963) 130–141. [https://doi.org/10.1175/1520-0469\(1963\)020<0130:DNF>2.0.CO;2](https://doi.org/10.1175/1520-0469(1963)020<0130:DNF>2.0.CO;2).
- [143] G. Haller, Distinguished material surfaces and coherent structures in three-dimensional fluid flows, *Physica D: Nonlinear Phenomena.* 149 (2001) 248–277. [https://doi.org/10.1016/S0167-2789\(00\)00199-8](https://doi.org/10.1016/S0167-2789(00)00199-8).
- [144] G. Haller, Lagrangian coherent structures from approximate velocity data, *Physics of Fluids.* 14 (2002) 1851–1861. <https://doi.org/10.1063/1.1477449>.

- [145] M.R. Allshouse, T. Peacock, Refining and classifying finite-time Lyapunov exponent ridges, *ArXiv:1506.07027 [Physics]*. (2015). <http://arxiv.org/abs/1506.07027> (accessed March 12, 2020).
- [146] S.C. Shadden, F. Lekien, J.E. Marsden, Definition and properties of Lagrangian coherent structures from finite-time Lyapunov exponents in two-dimensional aperiodic flows, *Physica D: Nonlinear Phenomena*. 212 (2005) 271–304. <https://doi.org/10.1016/j.physd.2005.10.007>.
- [147] S.L. Brunton, C.W. Rowley, Fast computation of finite-time Lyapunov exponent fields for unsteady flows, *Chaos*. 20 (2010) 017503. <https://doi.org/10.1063/1.3270044>.
- [148] X. Morel, M.A. Lucas, F.D. Santos, A Lagrangian study of the Brazil-Malvinas confluence: Lagrangian coherent structures and several lyapunov exponents, *Journal of Operational Oceanography*. 7 (2014) 13–23. <https://doi.org/10.1080/1755876X.2014.11020155>.
- [149] K. Burger, P. Kondratieva, J. Kruger, R. Westermann, Importance-Driven Particle Techniques for Flow Visualization, in: 2008 IEEE Pacific Visualization Symposium, 2008: pp. 71–78. <https://doi.org/10.1109/PACIFICVIS.2008.4475461>.
- [150] F. Ferstl, K. Burger, H. Theisel, R. Westermann, Interactive Separating Streak Surfaces, *IEEE Transactions on Visualization and Computer Graphics*. 16 (2010) 1569–1577. <https://doi.org/10.1109/TVCG.2010.169>.
- [151] D. Lipinski, K. Mohseni, A ridge tracking algorithm and error estimate for efficient computation of Lagrangian coherent structures, *Chaos*. 20 (2010) 017504. <https://doi.org/10.1063/1.3270049>.
- [152] F. Sadlo, A. Rigazzi, R. Peikert, Time-Dependent Visualization of Lagrangian Coherent Structures by Grid Advection, in: V. Pascucci, X. Tricoche, H. Hagen, J. Tierny (Eds.), *Topological Methods in Data Analysis and Visualization: Theory, Algorithms, and Applications*, Springer Berlin Heidelberg, Berlin, Heidelberg, 2011: pp. 151–165. https://doi.org/10.1007/978-3-642-15014-2_13.
- [153] F. Huhn, A. von Kameke, S. Allen-Perkins, P. Montero, A. Venancio, V. Pérez-Muñuzuri, Horizontal Lagrangian transport in a tidal-driven estuary—Transport barriers attached to prominent coastal boundaries, *Continental Shelf Research*. 39–40 (2012) 1–13. <https://doi.org/10.1016/j.csr.2012.03.005>.
- [154] S. Orre, B. Gjevik, J.H. LaCasce, Characterizing chaotic dispersion in a coastal tidal model, *Continental Shelf Research*. 26 (2006) 1360–1374. <https://doi.org/10.1016/j.csr.2005.11.015>.

- [155] L.A. Fiorentino, M.J. Olascoaga, A. Reniers, Z. Feng, F.J. Beron-Vera, J.H. MacMahan, Using Lagrangian Coherent Structures to understand coastal water quality, *Continental Shelf Research*. 47 (2012) 145–149. <https://doi.org/10.1016/j.csr.2012.07.009>.
- [156] H. Ku, J.H. Hwang, The Lagrangian Coherent Structure and the Sediment Particle Behavior in the Lock Exchange Stratified Flows, *Journal of Coastal Research*. (2018) 976–980. <https://doi.org/10.2112/SI85-196.1>.
- [157] Y. Wu, C.G. Hannah, M. O’Flaherty-Sproul, P. Thupaki, Representing kelp forests in a tidal circulation model, *Journal of Marine Systems*. 169 (2017) 73–86. <https://doi.org/10.1016/j.jmarsys.2016.12.007>.
- [158] M.J. Olascoaga, G. Haller, Forecasting sudden changes in environmental pollution patterns, *PNAS*. 109 (2012) 4738–4743. <https://doi.org/10.1073/pnas.1118574109>.
- [159] P.J. Nolan, H. Foroutan, S.D. Ross, Pollution Transport Patterns Obtained Through Generalized Lagrangian Coherent Structures, *Atmosphere*. 11 (2020) 168. <https://doi.org/10.3390/atmos11020168>.
- [160] K. Suara, M. Khanarmuei, A. Ghosh, Y. Yu, H. Zhang, T. Soomere, R.J. Brown, Material and debris transport patterns in Moreton Bay, Australia: The influence of Lagrangian coherent structures, *Science of The Total Environment*. 721 (2020) 137715. <https://doi.org/10.1016/j.scitotenv.2020.137715>.
- [161] A. Ghosh, K. Suara, S.W. McCue, Y. Yu, T. Soomere, R.J. Brown, Persistency of debris accumulation in tidal estuaries using Lagrangian coherent structures, *Science of The Total Environment*. 781 (2021) 146808.
- [162] R. Al-Ruzouq, M.B.A. Gibril, A. Shanableh, A. Kais, O. Hamed, S. Al-Mansoori, M.A. Khalil, Sensors, Features, and Machine Learning for Oil Spill Detection and Monitoring: A Review, *Remote Sensing*. 12 (2020) 3338. <https://doi.org/10.3390/rs12203338>.
- [163] H. Ahmad, MACHINE LEARNING APPLICATIONS IN OCEANOGRAPHY, *Aquat Res*. (2019) 161–169. <https://doi.org/10.3153/AR19014>.
- [164] A. Dogan, D. Birant, Machine learning and data mining in manufacturing, *Expert Systems with Applications*. 166 (2021) 114060. <https://doi.org/10.1016/j.eswa.2020.114060>.
- [165] B. Mahesh, Machine Learning Algorithms -A Review, 2019. <https://doi.org/10.21275/ART20203995>.

- [166] S. Temitope Yekeen, A.-L. Balogun, Advances in Remote Sensing Technology, Machine Learning and Deep Learning for Marine Oil Spill Detection, Prediction and Vulnerability Assessment, *Remote Sensing*. 12 (2020) 3416. <https://doi.org/10.3390/rs12203416>.
- [167] T. Bolton, L. Zanna, Applications of Deep Learning to Ocean Data Inference and Subgrid Parameterization, *Journal of Advances in Modeling Earth Systems*. 11 (2019) 376–399. <https://doi.org/10.1029/2018MS001472>.
- [168] S.C. James, Y. Zhang, F. O’Donncha, A machine learning framework to forecast wave conditions, *Coastal Engineering*. 137 (2018) 1–10. <https://doi.org/10.1016/j.coastaleng.2018.03.004>.
- [169] P.M.R. Bento, J.A.N. Pombo, R.P.G. Mendes, M.R.A. Calado, S.J.P.S. Mariano, Ocean wave energy forecasting using optimised deep learning neural networks, *Ocean Engineering*. 219 (2021) 108372. <https://doi.org/10.1016/j.oceaneng.2020.108372>.
- [170] R. Lou, Z. Lv, S. Dang, T. Su, X. Li, Application of machine learning in ocean data, *Multimedia Systems*. (2021). <https://doi.org/10.1007/s00530-020-00733-x>.
- [171] B. Azari, K. Hasan, J. Pierce, S. Ebrahimi, Evaluation of Machine Learning Methods Application in Temperature Prediction, *COMPUTATIONAL RESEARCH PROGRESS IN APPLIED SCIENCE & ENGINEERING*. 8 (2022) 1–12. <https://doi.org/10.52547/crpase.8.1.2747>.
- [172] H. Shen, Y. Jiang, T. Li, Q. Cheng, C. Zeng, L. Zhang, Deep learning-based air temperature mapping by fusing remote sensing, station, simulation and socioeconomic data, *Remote Sensing of Environment*. 240 (2020) 111692. <https://doi.org/10.1016/j.rse.2020.111692>.
- [173] G. Yang, H. Lee, G. Lee, A Hybrid Deep Learning Model to Forecast Particulate Matter Concentration Levels in Seoul, South Korea, *Atmosphere*. 11 (2020) 348. <https://doi.org/10.3390/atmos11040348>.
- [174] T. De Kerf, J. Gladines, S. Sels, S. Vanlanduit, Oil Spill Detection Using Machine Learning and Infrared Images, *Remote Sensing*. 12 (2020) 4090. <https://doi.org/10.3390/rs12244090>.
- [175] A.A. Huby, R. Sagban, R. Alubady, Oil Spill Detection based on Machine Learning and Deep Learning: A Review, in: 2022 5th International Conference on Engineering Technology and Its Applications (IICETA), 2022: pp. 85–90. <https://doi.org/10.1109/IICETA54559.2022.9888651>.
- [176] Y. Li, Q. Yu, M. Xie, Z. Zhang, Z. Ma, K. Cao, Identifying Oil Spill Types Based on Remotely Sensed Reflectance Spectra and Multiple Machine Learning Algorithms, *IEEE Journal of Selected Topics in Applied Earth*

- Observations and Remote Sensing. 14 (2021) 9071–9078. <https://doi.org/10.1109/JSTARS.2021.3109951>.
- [177] F. Löw, K. Stieglitz, O. Diemar, Terrestrial oil spill mapping using satellite earth observation and machine learning: A case study in South Sudan, *Journal of Environmental Management*. 298 (2021) 113424. <https://doi.org/10.1016/j.jenvman.2021.113424>.
- [178] M.S. Ozigis, J.D. Kaduk, C.H. Jarvis, Mapping terrestrial oil spill impact using machine learning random forest and Landsat 8 OLI imagery: a case site within the Niger Delta region of Nigeria, *Environ Sci Pollut Res*. 26 (2019) 3621–3635. <https://doi.org/10.1007/s11356-018-3824-y>.
- [179] X. Wu, Q. Zhou, L. Mu, X. Hu, Machine learning in the identification, prediction and exploration of environmental toxicology: Challenges and perspectives, *Journal of Hazardous Materials*. 438 (2022) 129487. <https://doi.org/10.1016/j.jhazmat.2022.129487>.
- [180] M.R.A. Conceição, L.F.F. de Mendonça, C.A.D. Lentini, A.T. da Cunha Lima, J.M. Lopes, R.N. de Vasconcelos, M.B. Gouveia, M.J. Porsani, SAR Oil Spill Detection System through Random Forest Classifiers, *Remote Sensing*. 13 (2021) 2044. <https://doi.org/10.3390/rs13112044>.
- [181] M. Shaban, R. Salim, H. Abu Khalifeh, A. Khelifi, A. Shalaby, S. El-Mashad, A. Mahmoud, M. Ghazal, A. El-Baz, A Deep-Learning Framework for the Detection of Oil Spills from SAR Data, *Sensors*. 21 (2021) 2351. <https://doi.org/10.3390/s21072351>.
- [182] Y. Fan, X. Rui, G. Zhang, T. Yu, X. Xu, S. Poslad, Feature Merged Network for Oil Spill Detection Using SAR Images, *Remote Sensing*. 13 (2021) 3174. <https://doi.org/10.3390/rs13163174>.
- [183] P. Liu, Y. Li, B. Liu, P. Chen, J. Xu, Semi-Automatic Oil Spill Detection on X-Band Marine Radar Images Using Texture Analysis, Machine Learning, and Adaptive Thresholding, *Remote Sensing*. 11 (2019) 756. <https://doi.org/10.3390/rs11070756>.
- [184] S. Tong, X. Liu, Q. Chen, Z. Zhang, G. Xie, Multi-Feature Based Ocean Oil Spill Detection for Polarimetric SAR Data Using Random Forest and the Self-Similarity Parameter, *Remote Sensing*. 11 (2019) 451. <https://doi.org/10.3390/rs11040451>.
- [185] S. Magrì, T. Vairo, A. Reverberi, B. Fabiano, Oil Spill Identification and Monitoring from Sentinel-1 Sar Satellite Earth Observations: a Machine Learning Approach, *Chemical Engineering Transactions*. 86 (2021) 379–384. <https://doi.org/10.3303/CET2186064>.

- [186] R. Trujillo-Acatitla, J. Tuxpan-Vargas, C. Ovando-Vázquez, Oil spills: Detection and concentration estimation in satellite imagery, a machine learning approach, *Marine Pollution Bulletin*. 184 (2022) 114132. <https://doi.org/10.1016/j.marpolbul.2022.114132>.
- [187] C.B. Maroun, G. Daou, B. Hammoud, B. Hammoud, Machine Learning Using Support Vector Regression in Radar Remote Sensing for Oil-Spill Thickness Estimation, in: 2021 18th European Radar Conference (EuRAD), 2022: pp. 221–224. <https://doi.org/10.23919/EuRAD50154.2022.9784478>.
- [188] L. Corucci, F. Nardelli, M. Cococcioni, Oil spill classification from multi-spectral satellite images: exploring different machine learning techniques, in: *Remote Sensing of the Ocean, Sea Ice, and Large Water Regions 2010*, SPIE, 2010: pp. 73–87. <https://doi.org/10.1117/12.864556>.
- [189] Y. Xiong, H. Zhou, Oil spills identification in SAR image based on Convolutional Neural Network, in: 2019 14th International Conference on Computer Science & Education (ICCSE), 2019: pp. 667–670. <https://doi.org/10.1109/ICCSE.2019.8845383>.
- [190] K. Zeng, Y. Wang, A Deep Convolutional Neural Network for Oil Spill Detection from Spaceborne SAR Images, *Remote Sensing*. 12 (2020) 1015. <https://doi.org/10.3390/rs12061015>.
- [191] S.T. Seydi, M. Hasanlou, M. Amani, W. Huang, Oil Spill Detection Based on Multiscale Multidimensional Residual CNN for Optical Remote Sensing Imagery, *IEEE Journal of Selected Topics in Applied Earth Observations and Remote Sensing*. 14 (2021) 10941–10952. <https://doi.org/10.1109/JSTARS.2021.3123163>.
- [192] S. Mohammadiun, G. Hu, A.A. Gharahbagh, J. Li, K. Hewage, R. Sadiq, Evaluation of machine learning techniques to select marine oil spill response methods under small-sized dataset conditions, *Journal of Hazardous Materials*. 436 (2022) 129282. <https://doi.org/10.1016/j.jhazmat.2022.129282>.
- [193] H.H. Murray, Traditional and new applications for kaolin, smectite, and palygorskite: a general overview, *Applied Clay Science*. 17 (2000) 207–221. [https://doi.org/10.1016/S0169-1317\(00\)00016-8](https://doi.org/10.1016/S0169-1317(00)00016-8).
- [194] SeaTemperature.org, World Water Temperature & | Sea Temperatures, (n.d.). <https://www.seatemperature.org/> (accessed April 20, 2023).
- [195] Y. Yu, Z. Qi, D. Xiong, W. Li, X. Yu, R. Sun, Experimental investigations on the vertical distribution and properties of oil-mineral aggregates (OMAs) formed by different clay minerals, *Journal of Environmental Management*. 311 (2022) 114844. <https://doi.org/10.1016/j.jenvman.2022.114844>.

- [196] W. Zhang, X. Yu, J. Zhang, Y. Wang, Study of oil-particle-aggregation by digital inline holograph, *Geosci J.* 23 (2019) 461–469. <https://doi.org/10.1007/s12303-018-0041-0>.
- [197] M.C. Sterling, J.S. Bonner, A.N.S. Ernest, C.A. Page, R.L. Autenrieth, Characterizing aquatic sediment–oil aggregates using in situ instruments, *Marine Pollution Bulletin.* 48 (2004) 533–542. <https://doi.org/10.1016/j.marpolbul.2003.10.005>.
- [198] N. Tambo, Y. Watanabe, Physical characteristics of flocs—I. The floc density function and aluminium floc, *Water Research.* 13 (1979) 409–419. [https://doi.org/10.1016/0043-1354\(79\)90033-2](https://doi.org/10.1016/0043-1354(79)90033-2).
- [199] N. Hawley, Settling velocity distribution of natural aggregates, *Journal of Geophysical Research: Oceans.* 87 (1982) 9489–9498. <https://doi.org/10.1029/JC087iC12p09489>.
- [200] I.N. McCave, Size spectra and aggregation of suspended particles in the deep ocean, *Deep Sea Research Part A. Oceanographic Research Papers.* 31 (1984) 329–352. [https://doi.org/10.1016/0198-0149\(84\)90088-8](https://doi.org/10.1016/0198-0149(84)90088-8).
- [201] C. Kranenburg, The Fractal Structure of Cohesive Sediment Aggregates, *Estuarine, Coastal and Shelf Science.* 39 (1994) 451–460. <https://doi.org/10.1006/ecss.1994.1075>.
- [202] K.J. Curran, P.S. Hill, T.G. Milligan, O.A. Mikkelsen, B.A. Law, X. Durrieu de Madron, F. Bourrin, Settling velocity, effective density, and mass composition of suspended sediment in a coastal bottom boundary layer, Gulf of Lions, France, *Continental Shelf Research.* 27 (2007) 1408–1421. <https://doi.org/10.1016/j.csr.2007.01.014>.
- [203] A. Vahedi, B. Gorczyca, Predicting the settling velocity of flocs formed in water treatment using multiple fractal dimensions, *Water Research.* 46 (2012) 4188–4194. <https://doi.org/10.1016/j.watres.2012.04.031>.
- [204] R.B. Moruzzi, J. Bridgeman, P.A.G. Silva, A combined experimental and numerical approach to the assessment of floc settling velocity using fractal geometry, *Water Science and Technology.* 81 (2020) 915–924. <https://doi.org/10.2166/wst.2020.171>.
- [205] L.C. Van Rijn, *Handbook: Sediment transport by currents and waves*, Rep, H461, Delft Hydraul., Delft, Netherlands. (1989).
- [206] R.L. Soulsby, *Dynamics of marine sands: a manual for practical applications*, *Oceanographic Literature Review.* 9 (1997) 947.
- [207] N.-S. Cheng, Simplified settling velocity formula for sediment particle, *Journal of Hydraulic Engineering.* 123 (1997) 149–152.

- [208] B. Camenen, Simple and general formula for the settling velocity of particles, *Journal of Hydraulic Engineering*. 133 (2007) 229–233.
- [209] S.M. Sadat-Helbar, E. Amiri-Tokaldany, Irrigation, Fall Velocity of Sediment Particles, in: 2009. <https://www.semanticscholar.org/paper/Fall-Velocity-of-Sediment-Particles-Sadat-Helbar-Amiri-Tokaldany/91ff8837fb11402e755f88d5bb294382ed7925e7> (accessed January 10, 2023).
- [210] E.B. Goldstein, G. Coco, A machine learning approach for the prediction of settling velocity, *Water Resources Research*. 50 (2014) 3595–3601. <https://doi.org/10.1002/2013WR015116>.
- [211] F. Pedregosa, G. Varoquaux, A. Gramfort, V. Michel, B. Thirion, O. Grisel, M. Blondel, P. Prettenhofer, R. Weiss, V. Dubourg, J. Vanderplas, A. Passos, D. Cournapeau, Scikit-learn: Machine Learning in Python, *Journal of Machine Learning Research*. 12 (2011) 2825–2830.
- [212] J. Yu, X. Zhong, Z. Huang, X. Lin, H. Weng, D. Ye, Q. (Sophia) He, J. Yang, Mining the synergistic effect in hydrothermal co-liquefaction of real feedstocks through machine learning approaches, *Fuel*. 334 (2023) 126715. <https://doi.org/10.1016/j.fuel.2022.126715>.
- [213] M. Reed, B. Hetland, DREAM: A dose-related exposure assessment model technical description of physical-chemical fates components, in: SPE International Conference on Health, Safety and Environment in Oil and Gas Exploration and Production, Society of Petroleum Engineers, 2002.
- [214] G.A.L. Delvigne, C.E. Sweeney, Natural dispersion of oil, *Oil and Chemical Pollution*. 4 (1988) 281–310. [https://doi.org/10.1016/S0269-8579\(88\)80003-0](https://doi.org/10.1016/S0269-8579(88)80003-0).
- [215] W. Ji, M. Boufadel, L. Zhao, B. Robinson, T. King, K. Lee, Formation of oil-particle aggregates: Particle penetration and impact of particle properties and particle-to-oil concentration ratios, *Science of The Total Environment*. 760 (2021) 144047. <https://doi.org/10.1016/j.scitotenv.2020.144047>.
- [216] L. Zhao, M.C. Boufadel, J. Katz, G. Haspel, K. Lee, T. King, B. Robinson, A New Mechanism of Sediment Attachment to Oil in Turbulent Flows: Projectile Particles, *Environ. Sci. Technol*. 51 (2017) 11020–11028. <https://doi.org/10.1021/acs.est.7b02032>.
- [217] P. Stoffyn-Egli, K. Lee, Formation and Characterization of Oil–Mineral Aggregates, *Spill Science & Technology Bulletin*. 8 (2002) 31–44. [https://doi.org/10.1016/S1353-2561\(02\)00128-7](https://doi.org/10.1016/S1353-2561(02)00128-7).
- [218] R. Jézéquel, J. Receveur, T. Nedwed, S. Le Floch, Evaluation of the ability of calcite, bentonite and barite to enhance oil dispersion under arctic

- conditions, *Marine Pollution Bulletin*. 127 (2018) 626–636. <https://doi.org/10.1016/j.marpolbul.2017.12.034>.
- [219] W. Wang, Y. Zheng, K. Lee, Chemical dispersion of oil with mineral fines in a low temperature environment, *Marine Pollution Bulletin*. 72 (2013) 205–212. <https://doi.org/10.1016/j.marpolbul.2013.03.042>.
- [220] Y. Ou, R. Li, R. Liang, Experimental Study on the Impact of NaCl Concentration on the Flocculating Settling of Fine Sediment in Static Water, *Procedia Engineering*. 154 (2016) 529–535. <https://doi.org/10.1016/j.proeng.2016.07.548>.
- [221] L.I. Portela, S. Ramos, A.T. Teixeira, Effect of salinity on the settling velocity of fine sediments of a harbour basin, *Coas*. 65 (2013) 1188–1193. <https://doi.org/10.2112/SI65-201.1>.
- [222] S. Al Ani, K.R. Dyer, D.A. Huntley, Measurement of the influence of salinity on floc density and strength, *Geo-Marine Letters*. 11 (1991) 154–158. <https://doi.org/10.1007/BF02431002>.
- [223] A.J. Manning, W.J. Langston, P.J.C. Jonas, A review of sediment dynamics in the Severn Estuary: Influence of flocculation, *Marine Pollution Bulletin*. 61 (2010) 37–51. <https://doi.org/10.1016/j.marpolbul.2009.12.012>.
- [224] A.J. Mehta, E.J. Hayter, W.R. Parker, R.B. Krone, A.M. Teeter, Cohesive Sediment Transport. I: Process Description, *Journal of Hydraulic Engineering*. 115 (1989) 1076–1093. [https://doi.org/10.1061/\(ASCE\)0733-9429\(1989\)115:8\(1076\)](https://doi.org/10.1061/(ASCE)0733-9429(1989)115:8(1076)).
- [225] J. Yang, L. Tang, Y. She, J. Sun, Laboratory measurements of the fall velocity of fine sediment in an estuarine environment, *International Journal of Sediment Research*. 35 (2020) 217–226. <https://doi.org/10.1016/j.ijsrc.2019.08.003>.
- [226] U.-J. Lee, K.-S. Hyeong, H.-Y. Cho, Estimation of Settling Velocity and Floc Distribution through Simple Particles Sedimentation Experiments, *Journal of Marine Science and Engineering*. 8 (2020) 500. <https://doi.org/10.3390/jmse8070500>.
- [227] S.A. Ryan, G.D. Wohlgeschaffen, N. Jahan, H. Niu, A.C. Ortmann, T.N. Brown, T.L. King, J. Clyburne, Canada, Department of Fisheries and Oceans, G. and E.R. (Canada) Centre for Offshore Oil, Dalhousie University, Department of Engineering, N.S.) Saint Mary's University (Halifax, Department of Chemistry, State of knowledge on fate and behaviour of ship-source petroleum product spills, 2019. http://epe.lac-bac.gc.ca/100/201/301/weekly_acquisitions_list-ef/2019/19-28/publications.gc.ca/collections/collection_2019/mpo-dfo/Fs97-4-3176-eng.pdf (accessed August 31, 2021).

- [228] Hemmera Envirochem Inc., M/V Marathassa Fuel Spill Environmental Impact Assessment, 2015. <http://www.ccg-gcc.gc.ca/folios/00025/docs/Marathassa-Hemmera.pdf> (accessed July 9, 2018).
- [229] D.R. Haggarty, An evaluation of fish habitat in Burrard Inlet, British Columbia, University of British Columbia, 2001. <https://doi.org/10.14288/1.0074846>.
- [230] D. Sutherland, Water Quality Objectives Attainment Monitoring in Burrard Inlet in 2002, Ministry of Water, Land and Air Protection, Environmental Quality Section., 2004.
- [231] J. Stone, K. Piscitelli, K. Demes, S. Chang, M. Quayle, D. Withers, Economic and biophysical impacts of oil tanker spills relevant to Vancouver, Canada: a literature review. Prepared for Vancouver Economic Commission, 2013. <https://www.vancouvereconomic.com/wp-content/uploads/2015/04/VEC-Report-Impacts-of-Oil-Tanker-Spills-Relevant-to-Vancouver.pdf>.
- [232] C. Chen, H. Liu, R.C. Beardsley, An Unstructured Grid, Finite-Volume, Three-Dimensional, Primitive Equations Ocean Model: Application to Coastal Ocean and Estuaries, *J. Atmos. Oceanic Technol.* 20 (2003) 159–186. [https://doi.org/10.1175/1520-0426\(2003\)020<0159:AUGFVT>2.0.CO;2](https://doi.org/10.1175/1520-0426(2003)020<0159:AUGFVT>2.0.CO;2).
- [233] Y. Wu, C. Hannah, M. O’Flaherty-Sproul, P. MacAulay, S. Shan, A modeling study on tides in the Port of Vancouver, *Anthropocene Coasts.* 2 (2019) 101–125.
- [234] C.D. Levings, S. Samis, Section II site description and oceanography., North Pacific Marine Science Organization, Sidney, BC, 2001. http://aquaticcommons.org/1313/1/Sci_Rep_16.pdf#page=23.
- [235] F. d’Ovidio, V. Fernández, E. Hernández-García, C. López, Mixing structures in the Mediterranean Sea from finite-size Lyapunov exponents, *Geophysical Research Letters.* 31 (2004). <https://doi.org/10.1029/2004GL020328>.
- [236] S. Page, Canada, Department of Fisheries and Oceans, Surface circulation tracking drifter data for the Kitimat Fjord system in northern British Columbia and adjacent continental shelf for April, 2014 to July, 2016, 2019. http://epe.lac-bac.gc.ca/100/201/301/weekly_acquisitions_list-ef/2019/19-24/publications.gc.ca/collections/collection_2019/mpo-dfo/Fs97-16-206-eng.pdf (accessed September 11, 2021).
- [237] O.M. Aamo, M. Reed, A. Lewis, Regional contingency planning using the OSCAR oil spill contingency and response model, in: ARCTIC AND

MARINE OILSPILL PROGRAM TECHNICAL SEMINAR, MINISTRY OF SUPPLY AND SERVICES, CANADA, 1997: pp. 289–308.

- [238] M. Reed, O.M. Aamo, K. Downing, Calibration and testing of IKU's oil spill contingency and response (OSCAR) model system, in: International Nuclear Information System, 1996: pp. 689–726.
- [239] M. Reed, P.S. Daling, O.G. Brakstad, I. Singsaas, L.-G. Faksness, B. Hetland, N. Ekrol, OSCAR2000: a multi-component 3-dimensional oil spill contingency and response model, (2000). http://inis.iaea.org/Search/search.aspx?orig_q=RN:31063064 (accessed September 14, 2018).
- [240] C. Chen, H. Liu, R.C. Beardsley, An unstructured grid, finite-volume, three-dimensional, primitive equations ocean model: application to coastal ocean and estuaries, *Journal of Atmospheric and Oceanic Technology*. 20 (2003) 159–186.
- [241] C. Chen, R.C. Beardsley, G. Cowles, An unstructured grid, finite-volume coastal ocean model: FVCOM user manual, Sea Grant College Program, Massachusetts Institute of Technology., 2012.
- [242] C. Chen, H. Huang, R.C. Beardsley, H. Liu, Q. Xu, G. Cowles, A finite volume numerical approach for coastal ocean circulation studies: Comparisons with finite difference models, *Journal of Geophysical Research: Oceans*. 112 (2007). <https://doi.org/10.1029/2006JC003485>.
- [243] H. Huang, C. Chen, G.W. Cowles, C.D. Winant, R.C. Beardsley, K.S. Hedstrom, D.B. Haidvogel, FVCOM validation experiments: Comparisons with ROMS for three idealized barotropic test problems, *Journal of Geophysical Research: Oceans*. 113 (2008). <https://doi.org/10.1029/2007JC004557>.
- [244] M.G.G. Foreman, W.R. Crawford, J.Y. Cherniawsky, R.F. Henry, M.R. Tarbotton, A high-resolution assimilating tidal model for the northeast Pacific Ocean, *Journal of Geophysical Research: Oceans*. 105 (2000) 28629–28651. <https://doi.org/10.1029/1999JC000122>.
- [245] X. Zhong, H. Niu, Y. Wu, C. Hannah, S. Li, T. King, A Modeling Study on the Oil Spill of M/V Marathassa in Vancouver Harbour, *Journal of Marine Science and Engineering*. 6 (2018) 106. <https://doi.org/10.3390/jmse6030106>.
- [246] G. Haller, A variational theory of hyperbolic Lagrangian Coherent Structures, *Physica D: Nonlinear Phenomena*. 240 (2011) 574–598. <https://doi.org/10.1016/j.physd.2010.11.010>.

- [247] F.J. Beron-Vera, M.J. Olascoaga, An Assessment of the Importance of Chaotic Stirring and Turbulent Mixing on the West Florida Shelf, *J Phys Oceanogr.* 39 (2009) 1743–1755.
- [248] D.A. Brooks, M.W. Baca, Y.-T. Lo, Tidal Circulation and Residence Time in a Macrotidal Estuary: Cobscook Bay, Maine, *Estuarine, Coastal and Shelf Science.* 49 (1999) 647–665. <https://doi.org/10.1006/ecss.1999.0544>.
- [249] R.T. Cheng, V. Casulli, On Lagrangian residual currents with applications in south San Francisco Bay, California, *Water Resources Research.* 18 (1982) 1652–1662. <https://doi.org/10.1029/WR018i006p01652>.
- [250] Xu Danya, Xue Huijie, Greenberg David A., A Numerical Study of the Circulation and Drifter Trajectories in Cobscook Bay, *Estuarine and Coastal Modeling* (2005). (2006). [https://doi.org/10.1061/40876\(209\)11](https://doi.org/10.1061/40876(209)11).
- [251] T. Fujiwara, H. Nakata, K. Nakatsuji, Tidal-jet and vortex-pair driving of the residual circulation in a tidal estuary, *Continental Shelf Research.* 14 (1994) 1025–1038. [https://doi.org/10.1016/0278-4343\(94\)90062-0](https://doi.org/10.1016/0278-4343(94)90062-0).
- [252] N. Imasato, What is Tide-Induced Residual Current?, *J. Phys. Oceanogr.* 13 (1983) 1307–1317. [https://doi.org/10.1175/1520-0485\(1983\)013<1307:WITIRC>2.0.CO;2](https://doi.org/10.1175/1520-0485(1983)013<1307:WITIRC>2.0.CO;2).
- [253] K.T. Tee, Tide-Induced Residual Current—Verification of a Numerical Model, *J. Phys. Oceanogr.* 7 (1977) 396–402. [https://doi.org/10.1175/1520-0485\(1977\)007<0396:TIRCOA>2.0.CO;2](https://doi.org/10.1175/1520-0485(1977)007<0396:TIRCOA>2.0.CO;2).
- [254] J. Butler, Independent Review of the M/V Marathassa Fuel Oil Spill Environmental Response Operation, Prepared for the Canadian Coast Guard, 2015. <http://www.ccg-gcc.gc.ca/independent-review-Marathassa-oil-spill-ER-operation> (accessed July 18, 2018).
- [255] K. Stormont, Stanley Park Ecological Society, After the oil spill: Stanley Park in the Wake of the English Bay Oil Spill, (2015). <http://www.webcitation.org/70oOgbAj7> (accessed July 18, 2018).
- [256] DFO, Technical review of the M/V Marathassa fuel spill environmental impact assessment report, DFO, Canada, 2017. https://www.dfo-mpo.gc.ca/csas-sccs/Publications/ScR-RS/2017/2017_006-eng.html (accessed January 22, 2022).

APPENDIX A

Copyright Permission for paper “An Overview of Oil-Mineral-Aggregate Formation, Settling, and Transport Processes in Marine Oil Spill Models”:

Co-authors' permission for the paper "An Overview of Oil-Mineral-Aggregate Formation, Settling, and Transport Processes in Marine Oil Spill Models"



Xiaomei Zhong
To: Haibo Niu, lipu@mail.sysu.edu.cn; Wu, Yongsheng; Lei Liu

Reply Reply All Forward Tue 2/14/2023 10:29 AM

Dear all,

I am preparing my Ph.D. thesis for submission to the Faculty of Graduate Studies at Dalhousie University, Halifax, Nova Scotia, Canada. I am seeking your permission to include a manuscript version of the following paper as a chapter in the thesis:

Paper title: An Overview of Oil-Mineral-Aggregate Formation, Settling, and Transport Processes in Marine Oil Spill Models

Authors: Xiaomei Zhong, Haibo Niu, Pu Li, Yongsheng Wu, Lei Liu

Paper status: Published in Journal of Marine Science and Engineering 10(5):610

Canadian graduate theses are reproduced by the Library and Archives of Canada (formerly National Library of Canada) through a non-exclusive, world-wide license to reproduce, loan, distribute, or sell theses. I am also seeking your permission for the material described above to be reproduced and distributed by the LAC(NLC). Further details about the LAC(NLC) thesis program are available on the LAC(NLC) website (www.nlc-bnc.ca).

Full publication details and a copy of this permission letter will be included in the thesis.

Please respond this email with your agreement/exception, also select/write down the grant choice (a or b) shown as below (please select b):

Permission is granted for:

- a) the inclusion of the material described above in your thesis.
- b) for the material described above to be included in the copy of your thesis that is sent to the Library and Archives of Canada (formerly National Library of Canada) for reproduction and distribution.

Name: Title:
Signature: Date:

Sincerely,

Xiaomei Zhong

答复: Co-authors' permission for the paper "An Overview of Oil-Mineral-Aggregate Formation, Settling, and Transport Processes in Marine Oil Spill ...



lipu@mail.sysu.edu.cn
To: Xiaomei Zhong

Reply Reply All Forward Fri 2/17/2023 9:05 PM

Click here to download pictures. To help protect your privacy, Outlook prevented automatic download of some pictures in this message.

CAUTION: The Sender of this email is not from within Dalhousie.

Dear Xiaomei,

The permission is granted for the material described above to be included in the copy of your thesis that is sent to the Library and Archives of Canada (formerly National Library of Canada) for reproduction and distribution.

Best regards,

Pu

Pu Li, Ph.D.
Associate Professor
School of Marine Sciences
Sun Yat-Sen University (Zhuhai Campus)
Zhuhai, Guangdong, China
Email: lipu@mail.sysu.edu.cn
Cell: +86 13825082373

Paper title: An Overview of Oil-Mineral-Aggregate Formation, Settling, and Transport Processes in Marine Oil Spill Models

Authors: Xiaomei Zhong, Haibo Niu, Pu Li, Yongsheng Wu, Lei Liu

Paper status: Published in Journal of Marine Science and Engineering 10(5):610

Canadian graduate theses are reproduced by the Library and Archives of Canada (formerly National Library of Canada) through a non-exclusive, world-wide license to reproduce, loan, distribute, or sell theses. I am also seeking your permission for the material described above to be reproduced and distributed by the LAC(NLC). Further details about the LAC(NLC) thesis program are available on the LAC(NLC) website (www.nlc-bnc.ca).

Full publication details and a copy of this permission letter will be included in the thesis.

Please respond this email with your agreement/exception, also select/write down the grant choice (a or b) shown as below (please select b):

Permission is granted for:

- a) the inclusion of the material described above in your thesis.
- b) for the material described above to be included in the copy of your thesis that is sent to the Library and Archives of Canada (formerly National Library of Canada) for reproduction and distribution.

Name: Yongsheng Wu

Title: Research Scientist

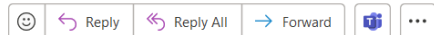
Signature:

Date:

RE: Co-authors' permission for the paper "An Overview of Oil-Mineral-Aggregate Formation, Settling, and T...



Lei Liu
To: Xiaomei Zhong



Wed 2/22/2023 11:39 PM

You replied to this message on 2/22/2023 11:44 PM.

Hi Xiaomei,
Sorry for being late to get back to you. Please use this email as my permission and signature for you to include the materials/paper mentioned below in your thesis.
Best,

LEI LIU | Ph.D., P.Eng.
Professor
Co-op Advisor in Civil/Environmental Engineering Program
Department of Civil and Resource Engineering
Dalhousie University
Room D215, D Building, P.O. Box 15000
5268 DaCosta Row, Halifax, NS Canada B3H 4R2

Phone: 902.494.3958
Fax: 902.494.3108
Email: Lei.Liu@Dal.Ca



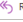



Journal of Marine Science and Engineering is an Open Access publication distributed under the terms and conditions of the Creative Commons by Attribution (CC-BY) license (<http://creativecommons.org/licenses/by/4.0/>) which permits unrestricted use, distribution, and reproduction in any medium.

Copyright Permission for paper “Applying Finite-time Lyapunov Exponent to Study the Tidal Dispersion on Oil Spill Trajectory in Burrard Inlet”:

Co-authors' permission for the paper "Applying Finite-Time Lyapunov Exponent to Study the Tidal Dispersion on Oil Spill Trajectory in Burrard Inlet"

 Xiaomei Zhong
To: Wu, Yongsheng; Hannah, Charles; Shihan Li; Haibo Niu

 Reply  Reply All  Forward  

Tue 2/14/2023 10:24 AM

Dear all,

I am preparing my Ph.D thesis for submission to the Faculty of Graduate Studies at Dalhousie University, Halifax, Nova Scotia, Canada. I am seeking your permission to include a manuscript version of the following paper as a chapter in the thesis:

Paper title: Applying Finite-Time Lyapunov Exponent to Study the Tidal Dispersion on Oil Spill Trajectory in Burrard Inlet

Authors: Xiaomei Zhong, Yongsheng Wu, Charles Hannah, Shihan Li, Haibo Niu

Paper status: Published in Journal of Hazardous Materials 437(8):129404

Canadian graduate theses are reproduced by the Library and Archives of Canada (formerly National Library of Canada) through a non-exclusive, world-wide license to reproduce, loan, distribute, or sell theses. I am also seeking your permission for the material described above to be reproduced and distributed by the LAC(NLC). Further details about the LAC(NLC) thesis program are available on the LAC(NLC) website (www.nlc-bnc.ca).

Full publication details and a copy of this permission letter will be included in the thesis.

Please respond this email with your agreement/exception, also select/write down the grant choice (a or b) shown as below (please select b):

Permission is granted for:

- the inclusion of the material described above in your thesis.
- for the material described above to be included in the copy of your thesis that is sent to the Library and Archives of Canada (formerly National Library of Canada) for reproduction and distribution.

Name: Title:
Signature: Date:

Sincerely,


Xiaomei Zhong

RE: Co-authors' permission for the paper "Applying Finite-Time Lyapunov Exponent to Study the Tidal Dispersion on Oil Spill Trajectory in Burrard Inl..."

 Hannah, Charles <Charles.Hannah@dfp-mpo.gc.ca>
To: Xiaomei Zhong

 Reply  Reply All  Forward  

Thu 2/16/2023 12:25 PM

 You replied to this message on 2/16/2023 12:27 PM.

CAUTION: The sender of this email is not from within Dalhousie.

Dear Xiaomei

I grant permission for the journal article described below to be included in the copy of your thesis that is sent to the Library and Archives of Canada (formerly National Library of Canada) for reproduction and distribution.

Paper title: Applying Finite-Time Lyapunov Exponent to Study the Tidal Dispersion on Oil Spill Trajectory in Burrard Inlet

Authors: Xiaomei Zhong, Yongsheng Wu, Charles Hannah, Shihan Li, Haibo Niu


Paper status: Published in Journal of Hazardous Materials 437(8):129404

Name: Charles Hannah Title: Research Scientist
Signature: Date: Feb 15, 2023



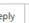
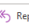
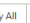
Charles Hannah
Research Scientist
Ocean Sciences Division | Division des sciences océaniques
Institute of Ocean Sciences | Institut des sciences de la mer
Fisheries and Oceans Canada | Pêches et Océans Canada
P.O. Box 6000, Sidney, B.C. V8L 4B2 | C. P. 5000, Sidney, (C.-B.) V8L 4B2

Tel: 1-250-363-6369

Re: Co-authors' permission for the paper " Applying Finite-Time Lyapunov Exponent to Study the Tidal Dispersion on Oil Spill Trajectory in Burrard Inl...

 Shihan Li
To: Xiaomei Zhong

 You replied to this message on 2/14/2023 11:06 PM.

 Reply  Reply All  Forward  

Tue 2/14/2023 10:06 PM

Hi Xiaomei,

You have my permission.

Good luck with your Ph.D thesis.

Best wishes,
Shihan

Paper title: Applying Finite-Time Lyapunov Exponent to Study the Tidal Dispersion on Oil Spill Trajectory in Burrard Inlet

Authors: Xiaomei Zhong, Yongsheng Wu, Charles Hannah, Shihan Li, Haibo Niu

Paper status: Published in Journal of Hazardous Materials 437(8):129404

Canadian graduate theses are reproduced by the Library and Archives of Canada (formerly National Library of Canada) through a non-exclusive, world-wide license to reproduce, loan, distribute, or sell theses. I am also seeking your permission for the material described above to be reproduced and distributed by the LAC(NLC). Further details about the LAC(NLC) thesis program are available on the LAC(NLC) website (www.nlc-bnc.ca).

Full publication details and a copy of this permission letter will be included in the thesis.

Please respond this email with your agreement/exception, also select/write down the grant choice (a or b) shown as below (please select b):

Permission is granted for:

- a) the inclusion of the material described above in your thesis.
- b) for the material described above to be included in the copy of your thesis that is sent to the Library and Archives of Canada (formerly National Library of Canada) for reproduction and distribution.

Name: Yongsheng Wu Title: Research Scientist

Signature: Date:

Authors may include their articles, either in full or in part, in a thesis or dissertation for non-commercial purposes, as per Elsevier's copyright and permissions policy.

APPENDIX B

Table S3.1. The OMA formation experiments setting based on Screening Design.

Standard order	Temperature (°C)	Salinity (ppt)	Agitation time (h)	Clay type	Agitation speed (rpm)	Oil/clay ratio	Dispersant
1	15	34	8	Montmorillonite	160	2: 1	Yes
2	15	0	4	Kaolinite	100	1: 2	No
3	30	17	8	Kaolinite	160	1: 2	No
4	0	17	4	Montmorillonite	100	2: 1	Yes
5	30	0	6	Kaolinite	160	2: 1	Yes
6	0	34	6	Montmorillonite	100	1: 2	No
7	30	34	8	Kaolinite	100	2: 1	No
8	0	0	4	Montmorillonite	160	1: 2	Yes
9	30	0	4	Montmorillonite	130	2: 1	No
10	0	34	8	Kaolinite	130	1: 2	Yes
11	30	34	4	Kaolinite	100	1: 1	Yes
12	0	0	8	Montmorillonite	160	1: 1	No
13	30	34	4	Montmorillonite	160	1: 2	No
14	0	0	8	Kaolinite	100	2: 1	Yes
15	30	0	8	Montmorillonite	100	1: 2	Yes
16	0	34	4	Kaolinite	160	2: 1	No
17	15	17	6	Kaolinite	130	1: 1	No
18	15	17	6	Montmorillonite	130	1: 1	Yes
1	15	34	8	Montmorillonite	160	2: 1	Yes
2	15	0	4	Kaolinite	100	1: 2	No
3	30	17	8	Kaolinite	160	1: 2	No
4	0	17	4	Montmorillonite	100	2: 1	Yes

Standard order	Temperature (°C)	Salinity (ppt)	Agitation time (h)	Clay type	Agitation speed (rpm)	Oil/clay ratio	Dispersant
5	30	0	6	Kaolinite	160	2: 1	Yes
6	0	34	6	Montmorillonite	100	1: 2	No
7	30	34	8	Kaolinite	100	2: 1	No
8	0	0	4	Montmorillonite	160	1: 2	Yes
9	30	0	4	Montmorillonite	130	2: 1	No
10	0	34	8	Kaolinite	130	1: 2	Yes
11	30	34	4	Kaolinite	100	1: 1	Yes
12	0	0	8	Montmorillonite	160	1: 1	No
13	30	34	4	Montmorillonite	160	1: 2	No
14	0	0	8	Kaolinite	100	2: 1	Yes
15	30	0	8	Montmorillonite	100	1: 2	Yes
16	0	34	4	Kaolinite	160	2: 1	No
17	15	17	6	Kaolinite	130	1: 1	No
18	15	17	6	Montmorillonite	130	1: 1	Yes



Figure S3.1 The temperature-controllable shaker.

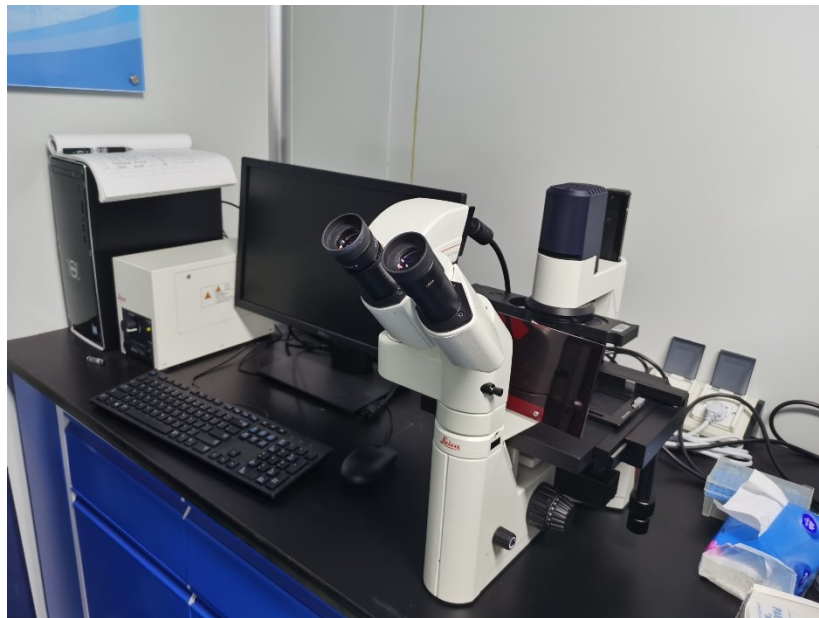


Figure S3.2 The inverted microscopy.

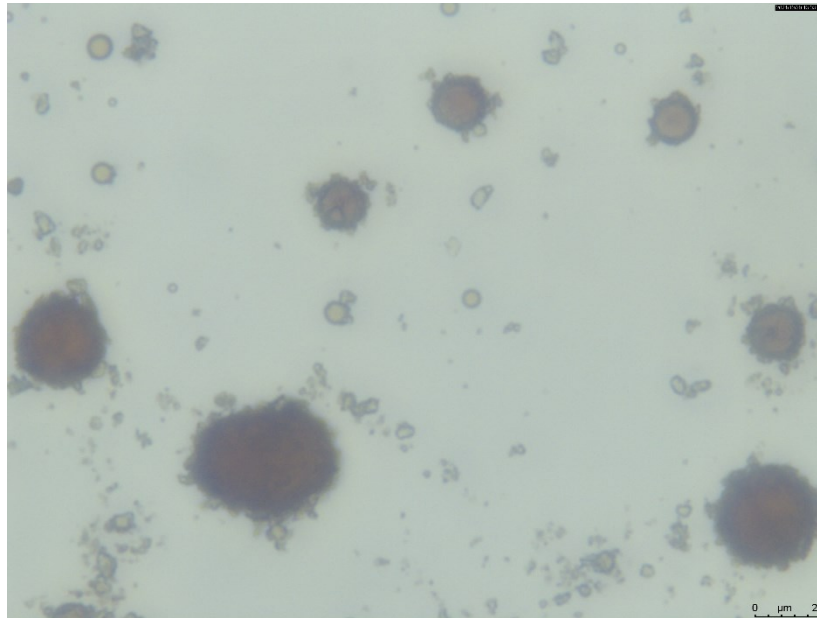


Figure S3.3 Example image of oil-mineral-aggregates acquired using inverted microscopy.

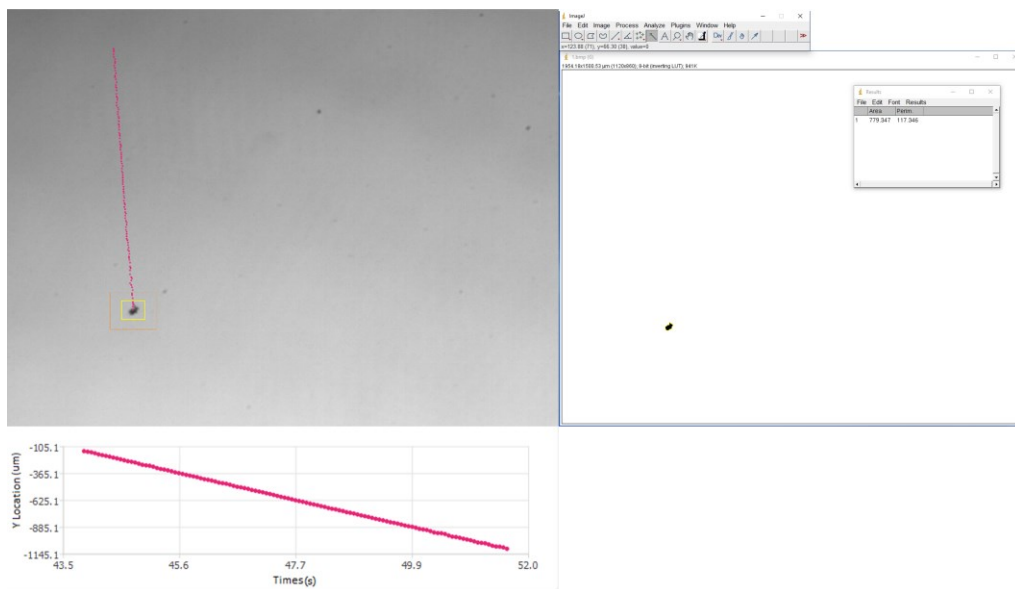


Figure S3.4 The example of OMA settling velocity and size measurements using RHSVTTMS-VL and ImageJ.exe.

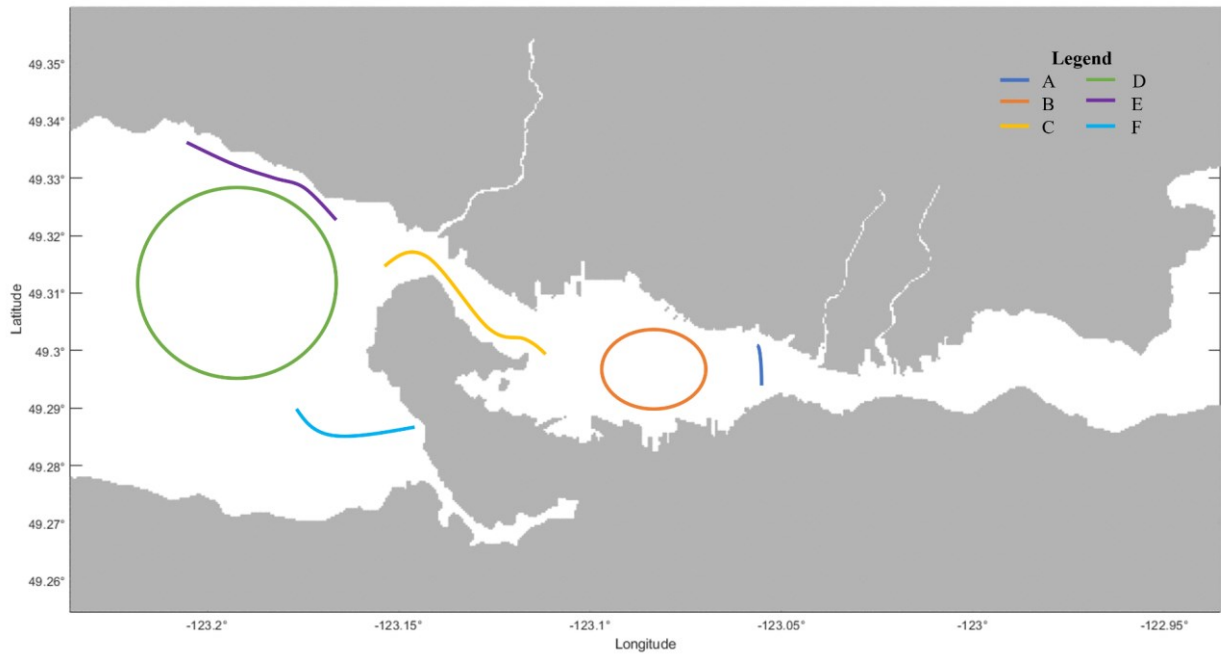


Figure S6.1. Selected locations for comparing the FTLE fields.

Table S6.1 A summary of Figure 6.2 and Figure 6.3.

Location	A	B	C	D	E	F
Spring tide						
Low tide	No observed material line	Tightly packed material lines	A clear material line	A large cyclonic eddy; material lines were distinctly separated	Observed material lines	Observed material lines
Mid-flood	No observed material lines	Tightly packed material lines in the middle with some material lines around the edges	Several clear material lines	A large cyclonic eddy; material lines were distinctly separated	Observed material lines and saddle points	Observed material lines
High tide	Observed material lines	Several material lines around the outer edges	A material line along the north shore of First Narrows	Two cyclonic eddies; material lines were distinctly separated	No observed material line	Observed material lines
Mid-ebb	No observed material line	Several material lines	Two clear material lines	Several eddies; material lines were distinctly separated	Observed material lines and saddle points	Observed material lines
Neap tide						
Low tide	Observed material line	Tightly packed material lines	Two clear material lines	Several eddies; material lines were distinctly separated	Observed material lines	No observed material line
Mid-flood	Several material lines	Tightly packed material lines in the middle with	A clear material line	Several eddies; material lines	Observed material lines	No observed

Location	A	B	C	D	E	F
		some material lines around the edges		were distinctly separated	and saddle points	material line
High tide	Observed material line	Several material lines in the north-south direction	A clear material line	Two eddies; material lines were distinctly separated	Observed material lines and saddle points	No observed material line
Mid-ebb	No observed material line	A few clear material lines	Two clear material lines	Several eddies; material lines were distinctly separated	Observed material lines and saddle points	No observed material line

Notes on the meaning of the phrases used in Table S6.1: 1) No observed material lines mean the FTLE field is almost a random collection of red, yellow, green, and blue. 2) Tightly packed material lines mean there are linear structures that are thin and broken apart. 3) Distinctly separated material lines mean that the water body is readily divided based on physical property. 4) Clear material lines are thick and continuous for substantial distances; for example, the red line in First Narrows in Figure 6.2a and the blue line in First Narrows in Figure 6.2d.